Development of sub-100 fs Yb:CALGO lasers with high peak power

By

Mohammad Anisur Rahman Reza

A thesis submitted to the faculty of graduate studies of

The University of Manitoba

In partial fulfillment of the requirements of the degree of

DOCTOR OF PHILOSOPHY

Department of Electrical and Computer Engineering

University of Manitoba

Winnipeg

Abstract

High power laser sources of ultrashort pulses (~fs, 10^{-15} s, femtosecond) have numerous applications in science, medicine, and technology such as spectroscopy, optical coherence tomography, microscopy, laser micromachining and processing of materials (e.g., all smartphone glass screens are cut with ultrashort laser pulses). The generation of ultrashort laser pulses requires a laser gain medium to have a broad emission spectrum. Generation of ultrashort pulses with high average power, on the other hand, also requires the gain medium to have good thermal conductivity. These two requirements (i.e., emission spectrum vs thermal conductivity), unfortunately, are contradictory to each other. Broad emission spectra (>30 nm) are generally observed from materials with disordered structure, i.e., glasses, which have poor thermal conductivity (~1W/m/K). Crystals, on the other hand, have good thermal conductivity (~5-10 W/m/K), but narrow emission spectra (<10 nm). At the same time propagation of intense laser pulses induces strong nonlinear optical effects in laser components (laser crystals, lenses, and even in air, etc.) which all should be minimized to avoid pulse spreading in time. Therefore, generation of ultrashort laser pulses with high average power is not a trivial task not only from the material properties point of view, but also from the way that these pulses are generated and stabilized. A method of generation of ultrashort pulses is called mode locking. Fortunately, a new laser crystal, Yb:CALGO, recently became available which has very good spectroscopic and thermal properties, i.e. 50 nm of bandwidth and 6.9 W/m/K of thermal conductivity.

The first stage of the work focused on the continuous-wave (CW) operation of the laser. To enhance the lasing efficiency, the intracavity losses were estimated and made sure that this loss was low. The next step was high power CW operation by using a birefringent filter (BRF). The use of traditional BRF can generate a wavelength pair with fixed wavelength separation for a fixed filter thickness. But using the off-surface axis BRF we can change this separation without the need to use different thickness of the filter. Also, the minimum obtainable wavelength separation is inversely proportional to the filter thickness, so the first step was to design an optimized off-surface axis BRF and then used two off-surface axis BRFs with 12 mm and 24 mm thickness in the experiments. The shortest wavelength separation was approximately 4 nm in this experiment. I believe this short wavelength separation with high output power will increase the usefulness of

DW lasers in THz generation and it will be suitable for different astronomical applications where DW with short wavelength separation is needed. Conical refraction (CR) output from the laser was obtained by using a separate conerefringent element (CRE). The resultant CR beam had very good quality and with power scalable high output power.

The rest of the work was focused on the development of the ultrashort pulse generation by mode locking method. Applications like nonlinear microscopy and fluorescence imaging require low repetition (1-20 MHz) rate oscillators. But typically, the pulse repetition rate of the conventional laser sources is around 70-100 MHz. The repetition rate can be reduced by a pulse picker or cavity dumper which are complex in design and costly. As the repetition rate is inversely proportional to the cavity length, the alternative simple way is to increase the cavity length which is known as the extended-cavity method. Two experiments were performed for ultrashort pulse generation. In the first experiment, the cavity was extended by using a 1:1 imaging telescope and 81 fs pulses were obtained at 26.9 MHz repetition rate. Reducing the repetition rate further would need more optics and complex alignment, so in the second experiment the cavity was extended by using the White cell configuration which is compact and easy to operate. Pulses as short as 114 fs were obtained at 8.2 MHz repetition rate. Apart from 8.2 MHz, laser also worked 10.15 MHz and 13.85 MHz repetition rate using the White cell. Hopefully, the development of such a compact and low repetition rate femtosecond laser will be suitable for applications like nonlinear microscopy, fluorescence imaging etc.

Acknowledgements

First, I would like to thank the almighty god for his countless blessings on me.

The completion of these experiments could not have been possible without the expertise and guidance of my supervisor Dr. Arkady Major. I would like to thank him from the bottom of my heart for giving me this opportunity. Not only he taught me laser engineering and research methods but also, he taught me professionalism, kindness, and sincerity. Many thanks to my Ph.D. committee members Dr. Cyrus Shafai and Dr. Jacob Burgess for their valuable suggestions and comments. A very special thanks to the PostDoc Dr. Reza Akbari for his generous guidance.

I would like to express my gratitude to the University of Manitoba for awarding me graduate fellowship, international graduate student scholarship and financial assistance over the years. I would also like to thank the Natural Sciences and Engineering Research Council of Canada (NSERC) and Western Economic Diversification Canada for funding.

I would like to thank my colleagues: Dr. Sujith Manjooran, Dr. Valadimir Montero Collado, Dr. Mohammad Nadimi, Zohreh, Chinedu, Rubel Chandra for their fruitful suggestions and discussion.

I would like to express my gratitude to my family. Without their support and sacrifice, I could not make it. Thanks to my father Ahmed Ali, mother Nurun Nahar, brother Abdur Rahman. I would like to express my gratitude to my wife Kaniz Maria Yousra for her constant support throughout the journey.

Contents

Page No.

List of figures

List of tables

List of Symbols and abbreviations

Symbols

E_p	Pulse energy
f	Repetition rate
f_l	Fractional population of lower laser level
f_u	Fractional population of upper laser level
L	Length of cavity
L_{in}	Roundtrip intracavity loss
l_c	Crystal length
M^2	Beam quality factor (M-squared)
N_0	Doping concentration
P_{abs}	Absorbed pump power
P_{inc}	Incident pump power
P_{out}	Average output power
P_{peak}	Peak power
P_{th}	Threshold pump power
R_{oc}	Reflectivity of the output coupler
T_{oc}	Transmission of output coupler
w_l	Laser mode radius
w_p	Pump mode radius

β	Fractional population inversion
δ_{reabs}	Reabsorption loss
λ_L	Lasing wavelength
$\Delta\lambda$	Optical spectrum
σ_{abs}	Absorption cross-section
σ_{em}	Emission cross-section

Abbreviations

AR	Antireflection coated
BRF	Birefringent filter
CR	Conical refraction
CRE	Conerefringent element
CW	Continuous-wave
DM	Dichroic mirror
DW	Dual-wavelength
FSR	Free spectral range
FWHM	Full width at half maximum
GTI	Gires-Tournois interferometer
GVD	Group velocity dispersion
HR	Highly reflecting
$Sech^2$	Hyperbolic secant function squared

KLAS	Kerr-lens and saturable absorber
KLM	Kerr-lens mode locking
ML	Mode locking
MD	Modulation depth
OC	Output coupler
RF	Radio frequency
SPM	Self-phase modulation
SESAM	Semiconductor saturable absorber mirror
TBP	Time-bandwidth product

Chapter 1
Introduction

1.1 Introduction

"LASER" originated as an acronym for Light Amplification by Stimulated Emission of Radiation. In laser, the electromagnetic radiation is optically amplified by the stimulated emission process. Based on the proposed theory of Charles Hard Townes and Arthur Leonard Schawlow, Theodore H. Maiman built the first laser in 1960. Unlike other light sources, a laser emits coherent and monochromatic light [1.1]. A large range of spectrum from ultraviolet to far-infrared is covered by various types of lasers such as solid-state lasers, gas lasers, semiconductor lasers, dye lasers, fiber lasers, etc. in the form of continuous-wave or ultrashort pulse operation regimes. Compared to other types of lasers, solid-state lasers are popular because of their high efficiency and better beam quality. In most of the cases, solid-state lasers are pumped by laser diodes (instead of flash lamps) because of their narrow spectral output which increases its absorption in the solid-state material. The use of laser diodes instead of flash lamps for pumping was demonstrated by R. J. Keyes and T.M. Quist for the first time in 1964 [1.2].

Ultrafast laser technology with the femtosecond pulse duration has numerous applications such as multiphoton imaging, X-rays generation, micromachining, time-resolved spectroscopy, etc. It is possible to obtain a very precise time resolution because of the short pulse duration. In addition to that, the highly confined energy within the very short pulse duration can induce various nonlinear effects. Thus, a high spatial resolution can be obtained because of the localization of these non-linear effects only to the focal spot area [1.3]. The pulse width and its optical bandwidth are related by the Fourier transform. So, if we obtain a shorter pulse duration it means that its spectral bandwidth should be broader. The high bandwidth is attractive for optical communication. For a certain amount of pulse energy, its peak power and peak intensity are inversely proportional to the pulse duration [1.4]. Therefore, it is possible to obtain very high peak power with ultrashort pulses. In the following paragraphs, we would like to briefly discuss a few applications of the lasers that produce femtosecond pulses (10^{-15} s).

Femtosecond lasers are very popular in biomedical applications. They can perform optical imaging in scattering media such as tissues with better resolution and depth information. Using two-photon excitation, a good spatial resolution has been obtained by nonlinear laser microscopy [1.4-1.6]. As we can generate high peak power pulses (>1 kW) without having high pulse energy, this makes femtosecond lasers useful for sensitive biological tissues.

High-power lasers with ultrashort pulses are also very attractive for material processing. In the case of continuous-wave lasers, accurate and high-quality cutting or drilling is hard because of the heating effect arising around the focus area. On the other hand, short duration pulses with moderate energy and high peak power make it possible to cut or drill with high precision because of the reduction of the deposited heat into the sample during laser operation [1.4].

Ultrafast pulse technology could play a vital role in optical communication. The low loss window of the optical fiber has a bandwidth comparable to the bandwidth of sub-100 fs pulses. So, it is possible to accommodate multiple channels within this high bandwidth for wavelength division multiplexing (WDM) [7]. Along with shorter pulse generation, it is also important for signal processing and advanced metrology [1.4].

Using the nonlinear harmonic generation process, it is possible to generate shorter wavelengths from the lasers with high intensity pulses in the visible range. This short coherent wavelength is important to study microscopic structures such as DNA [1.4, 1.8].

Laser pulses directed to solid targets with intensities of 10^{13} W/cm^2 or higher can remove the electrons from atoms. However, within a very short time range such as 100 fs, it is not possible to separate them from the ionized nuclei. Using this property, one can study solid density plasma at a temperature of around 1 million degrees [1.4].

Using femtosecond time scale of the pulses, ultrafast spectroscopy becomes a popular tool for microscopic object study such as photoexcited electron-hole dynamics and interaction with lattice vibrations, laser-induced photodissociation, melting, and solution dynamics of chemical species. In addition, to observe the dynamic chemical reaction, it is also possible to control their direction using ultrafast technology [1.4].

1.2 Motivation

Ti:sapphire has been a popular ultrafast laser source for many years because of its 180 nm emission bandwidth and 34 W/m/K thermal conductivity [1.9,1.10]. Because of its large emission bandwidth pulses as short as 5 fs have been generated and wide wavelength tuning operations have been reported as well [1.11-1.13]. However, Ti:sapphire has limitations as well. The efficiency of Ti:sapphire is low, and another laser system was needed to pump it. Argon-ion laser or a frequency-doubled Nd:YVO4 were used to pump Ti:sapphire laser systems [1.13,1.14]. This problem has been overcome recently by using InGaN or GaN laser diodes [1.15-1.17], however, to get the high peak power or pulse energy, complicated and costly amplification methods are needed [1.18].

Because of the above-mentioned limitations, the development of an alternative laser material was of interest. Among different available laser materials, Yb-ion doped laser crystals are popular because of their low quantum defect i.e. difference in energy between the pump photon and laser photon and no concentration quenching. The concentration quenching increases with doping levels and caused non-radiative decay of excited ions from the upper laser level to the ground level. As a result, the efficiency of the laser decreases [1.19, 1.20]. Also, the absorption band of the Yb-doped materials is around 980 nm which can be easily pumped by available InGaAs laser diodes.

Compared to other laser crystals, Yb-doped laser materials have comparatively broad emission bandwidth and high thermal conductivity which are suitable for the generation of ultrashort pulses with high output power. Over time, several Yb crystals have become popular for ultrashort pulse operation. A comparative study of the popular Yb-ion laser materials with Ti:sapphire is given in table 1.1. The optical-to-optical efficiency were calculated with respect to incident pump power and only mode-locked lasers were considered.

Based on table 1.1, we can see that a combination of broad emission bandwidth with high thermal conductivity for an Yb–doped crystal is rare except for Yb:CALGO. It has a broad emission bandwidth with high thermal conductivity compared to the other Yb-doped crystals. Based on the above table, Yb:CALGO is clearly the best choice for high power ultrashort pulse operation. In the next section of the thesis, the physical and optical properties of Yb:CALGO crystal will be discussed.

Table 1.1. Comparison of Yb laser crystals with Ti:sapphire

Laser crystal	Emission bandwidth (nm)	Central emission peak (nm)	Thermal conductivity (W/m/K)	Optical-to-optical Efficiency (%)
Ti:sapphire	180	790	34	10 [1.13]
Yb:YAG	9	1031	11	12.66 [1.21]
Yb:KGW	25	1030	3.3	10.66 [1.22]
Yb:KYW	24	1025	3.3	3.75 [1.23]
Yb:Glass	35	1020	0.8	12.79 [1.24]
Yb:CaF_2	30	1047	9.7	18.33 [1.25]
Yb:CALGO	50	1050	6.9	20 [1.26]

1.3 Properties of Yb:CALGO

In this section, the discussion will be focused on the fundamental properties of Yb:CALGO including its structure and preparation, optical properties and thermal properties.

1.3.1 Physical properties

Yb:CALGO was first introduced by Petit in 2005 [1.27]. This crystal is grown by Czochralski method. Raw Yb_2O_3, $CaCO_3$, Gd_2O_3 and Al_2O_3 powders are mixed based on the formula $CaGd_{0.92}Yb_{0.08}AlO_4$ and under very high pressure of about 300 MPa, they become tiny crystal pieces. Then those pieces are charged into an aluminium cubicle and sintered at 1200°C temperature to finish a solid-state reaction based on the following chemical formula:

$CaCO_3 + 0.04Yb_2O_3 + 0.46Gd_2O_3 + 0.5Al_2O_3$ $CaGd_{0.92}Yb_{0.08}AlO_4 + CO_2\uparrow$.

With a single CALGO crystal seed, the crystal can then be pulled out from the melt with an appropriate size [1.28].

The rare earth calcium aluminate $CaLnAlO_4$ (where Ln= Y, La,..Gd…Lu) is a tetragonal system and is a member of $ABCD_4$ compounds [1.28]. Here A= Ca, Sr, or Ba, B= Gd or other rare earth metals, C= Al, Ga or other transition metals. The Chemical formula for CALGO is $CaGdAlO_4$ and Ca^{2+} & Gd^{3+} occupy the same crystallographic sites and are expected to be replaced by Yb^{3+}. Although Ca^{2+} and Gd^{3+} share the same crystallographic site, it is more likely that the substitution will happen with Gd^{3+} because of the same valence of Gd^{3+} and Yb^{3+} ions. As a result, an inhomogeneous broadening happens which leads to a large emission bandwidth. This kind of disorder might reduce the thermal conductivity as well which is obstacle for high power laser operation. However, to minimize the negative impact on the thermal conductivity due to adding the doping ions, the atomic mass of the dopant should be close to the mass of the substituted ions. The atomic mass of Yb^{3+} ion is 70 and the mass of Gd^{3+} ion is 64. Because of this small difference, Yb:CALGO shows excellent stability [1.29]. In Yb:CALGO, the optic axis is parallel to the crystallographic *c*-axis. Therefore, there are two principal refractive indices (n_e and n_o) and two polarizations with electric field *E* parallel to the *c*-axis which is π-polarization and *E* perpendicular to the *c*-axis which is known as σ- polarization. Some physical properties of Yb:CALGO crystal are listed in table 1.2.

Table 1.2. Physical properties of Yb:CALGO [1.30]

Physical properties	**Values**
Crystal structure	Tetragonal
Density	5.97 g/cm^3
Melting point	1840°C
Refractive index	n_e = 1.9331 n_o =1.9564
Group velocity dispersion (1050 nm)	95 fs^2/mm
Thermo-optic coefficients	dn_o/dT= -7.6*10^{-6} K^{-1} dn_e/dT= -8.6*10^{-6} K^{-1}
Emission bandwidth	~50 nm

1.3.2 Energy level diagram

Yb-ion lasers are highly efficient because of their simple energy level scheme. The absorption and emission occur between two manifolds. Since this scheme does not have any additional loss channel, the concentration quenching, upconversion and excited state absorption will be lower which makes it very useful for high power laser operation with shorter pulses. The upconversion can be defined as a process where the emitted photons have higher energy than the excited photons. This can happen with intense pump source which might cause sequential absorption. The excited state absorption is the process where the ions in the excited states cause absorption of light which directly reduces the laser efficiency.

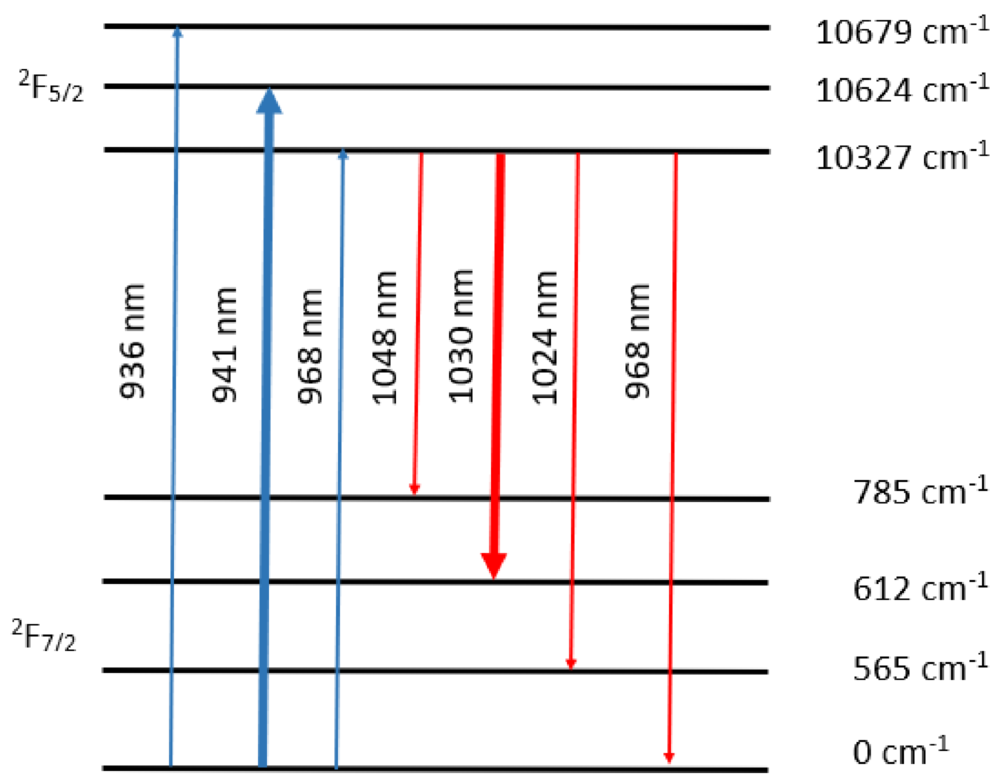

Figure 1.1: Schematic of Yb:YAG crystal energy level splitting with upper & lower manifolds and their energies. The main laser transition shown by the heavy line.

Ytterbium has only two manifolds, the ground state ($^2F_{7/2}$) and an excited state ($^2F_{5/2}$) which are located 10000 cm^{-1} away from each other. The upper state ($^2F_{5/2}$) degenerates into three Stark levels and the lower state ($^2F_{7/2}$) degenerates into four Stark levels [1.31, 1.32]. The host determines the separation between the Stark levels which may vary from 400 cm^{-1} to 1300 cm^{-1}. To get a better idea of the pump and laser transitions, consider the energy level diagram of Yb:YAG in figure 1.1 (The crystal splitting of Yb:CALGO is not available) [1.33]. At room temperature the fractional population in the lower laser level is f_1 = 0.046 and the fractional population in the upper laser level is f_2 = 0.70.

1.3.3 Spectroscopic properties

The inhomogeneous broadening in Yb:CALGO that occurs from the disordered structure results in the broad emission bandwidth. As Yb:CALGO is a uniaxial crystal and its optical axis is parallel to the c-axis, so there are two polarizations as stated in section 1.3.1. The absorption and emission spectrum for both polarizations are shown in figure 1.2. The highest absorption is around 979 nm and the absorption for the π-polarization is higher than for the σ-polarization. Although the absorption peak is at 979 nm, the absorption in the 930-990 nm range is reasonably high [1.34]. The emission is high for the σ-polarization and the peak emission is around 1050 nm with approximately 50 nm emission bandwidth.

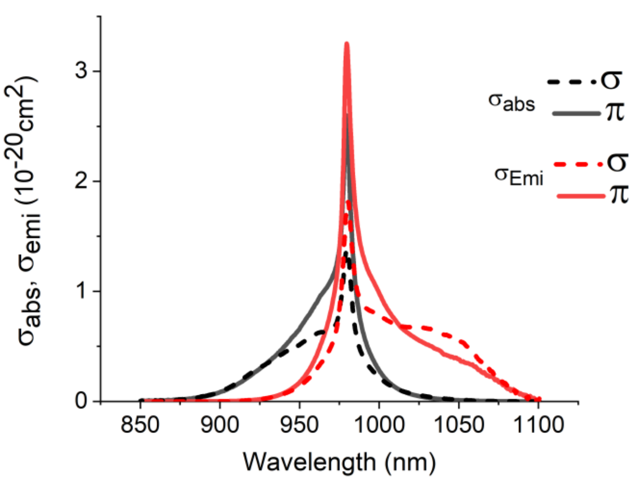

Figure 1.2: Absorption and emission cross-section spectra of Yb:CALGO [1.34].

For high-efficiency laser, the emission cross-section (σ_{em}) and the lifetime (τ) of the upper laser state play a vital role. The higher the $\sigma_{em}\tau$ product is, the lower the laser threshold will be. The value of the emission cross-section of Yb:CALGO crystal is σ_{em}= 0.8 ×$10^{-20}$$cm^2$ and the value of the lifetime is τ= 420 μs [1.3]. Therefore, the value of $\sigma_{em}\tau$ product is 3.36 ×10^{-18} μs cm^2 which is also satisfactory compared to the popular Yb:KGW laser which has $\sigma_{em}\tau$ product of 16.8 ×10^{-18} μs cm^2 but twice lower thermal conductivity. To minimize the laser threshold further, low output coupler transmission should be used while keeping other cavity losses at minimum.

1.3.4 Thermo-optical and thermo-mechanical properties

Heat management is an important part of laser design, as heavy heat loads might cause the thermal lensing effect which has a negative impact on the laser operation and thermal stresses which might cause a fracture of the laser crystal. To evaluate thermal performance of a laser crystal, thermal expansion coefficient (α) and thermal conductivity (k) play a vital role. Based on the thermal expansion coefficient, one can understand the expansion or shrinkage of the laser crystal with the variation in temperature while thermal conductivity tells us how fast it can release the produced heat.

The thermal expansion coefficient depends on the characteristics of the bonds of the materials. Materials with more ionic bond characteristics show higher thermal expansion. But materials with covalent bonding which has equal bonding strength show weaker thermal expansion. Due to thermal expansion, the end faces of the laser medium deform. In addition to that, thermal expansion causes thermal lensing effect by stress-induced variation of refractive index. The situation becomes even worse when the thermal expansion and the induced stress is so strong that it may result in the fracture of the laser medium. For anisotropic crystals, the variation of the thermal expansion is orientation sensitive and may result in fracture at high temperatures [1.34-1.36]. For a laser crystal, the maximum permitted heat load (before a fracture occurs) is inversely proportional to the thermal expansion coefficient. The value of thermal expansion coefficient in Yb:CALGO for the *a* and *c* crystallographic axes (*a*-axis is perpendicular to the *c*-axis) are $\alpha_a = 10\times10^{-6}$ K^{-1} and $\alpha_c = 16\times10^{-6}$ K^{-1} [1.34] which is satisfactory compared to its competitor laser crystal Yb:KGW with $\alpha_a = 4\times10^{-6}$ K^{-1}, $\alpha_b = 3.6\times10^{-6}$ K^{-1} $\alpha_c = 8.5\times10^{-6}$ K^{-1} [1.37].

Thermal conductivity plays a vital role in reducing the thermal effects. Thermal conductivity is the result of phonon diffusion in the materials. The population of phonon states increases with temperature which in turn reduces the thermal conductivity of a crystal at normal operating conditions. In addition to that, doping has an impact on thermal conductivity. Defects, impurities, dopant ions add irregularities in the lattice structure. These irregularities in the lattice structure are the source of scattering. This is the reason behind the low thermal conductivity of disordered materials. Sometimes, a drastic reduction in thermal conductivity is also noticed as a result of high doping. If the dopant ions and the replaced ions are nearly the same in radii, mass and effective charge, then the total disorder is also very low in the crystal. In this situation, the degradation in the thermal conductivity is also very low.

The influence of doping on the thermal conductivity for Yb: CALGO has been shown in Ref. 1.34. The variation of thermal conductivity was calculated for various substitution ratios from 100%-Gd / 0%-Ca to 50%-Gd / 50%-Ca. In the case of the substitution of Gd^{3+} by Yb^{3+}, there should be no effects on thermal conductivity i.e., the thermal conductivity should remain almost the same. However, experimental results were different from the calculated ones. So, it was proposed that this could be the reason for the substitution of Ca ions by Yb ones. The base of this proposal is that “Gd and Ca share the same crystallographic symmetric site”. When the calculated results were compared with the experimental results, it was apparent that the best fit was the 80%-Gd/ 20%-Ca line. However, it was shown that below 5% doping concentration, it matched more closely with the 70%-Gd/30%-Ca line. The thermal conductivity along the *a*-axis is actually better than for the *c*-axis. The same statement was also mentioned in Ref. 1.36, where thermal conductivity along the *a*-axis and c-axis was k_a = 6.9 W/m/K and k_c = 6.3 W/m/K.

The change of refractive index with temperature is very important as this change in refractive index will cause the thermal lensing effect. This effect can be due to the temperature itself, i.e. Δn is proportional to the *dn/dT* or in the other case, the variation of the refractive index could be because of the stress, i.e. Δn is proportional to the thermal expansion coefficient of the material. If the laser crystal is heated inhomogeneously then *dn/dT* will depend on the orientation of the heat flow, orientation, and shape of the heated zone. The *dn/dT* could be positive or negative. For uniaxial Yb:CALGO, two thermo-optic coefficients (dn_o/dT for π-polarization and dn_e/dT for σ-polarization) are observed as its optical axis is parallel to the crystallographic *c*-axis. The values of TOCs (thermo-optic coefficients) at 1.03 μm are: dn_0/dT = -7.6 ×10-5 K^{-1} and dn_e/dT= -8.8 ×10-6 K^{-1} [1.34].

1.4 Thesis organization and contribution

This thesis has 7 chapters. In chapter 1, the applications of ultrashort pulses in various fields have been discussed. Then the motivation and goal of this work have been discussed as well. The reason for choosing Yb:CALGO crystal has been discussed in this chapter as well. The physical, optical and thermal properties of Yb:CALGO have been discussed in this chapter.

In Chapter 2, the intracavity loss estimation in our continuous-wave (CW) laser has been discussed. Intracavity loss estimation is important as it has an impact on lasing efficiency and in an extreme case it might cease lasing as well. The loss measurement was based on the spectroscopic gain analysis and the results were compared with the traditional loss estimation methods (Findlay-Clay and numerical methods). Based on this work, the following paper has been published:

1. Md. A.R. Reza, P. Loiko, and A. Major, "Intracavity loss measurement in a diode-pumped Yb:CALGO laser", Proc. of SPIE, vol. 10896 (2019).

[The results from this experiment have been drafted for submission to the Laser Physics journal.]

In chapter 3, the dual-wavelength operation and its wavelength tuning based on a birefringent filter (BRF) have been discussed. An off-surface axis BRF was used instead of a traditional one as it allows to change the dual-wavelength separation without the need to use BRF with different thicknesses. The designing process of the off-surface axis BRF has been discussed and then results have been discussed based on a 12 mm and 24 mm off-surface axis BRFs. This chapter is based on the following publications:

1. Md. A.R. Reza, C. Dyck, S. Manjooran, P. Loiko, and A. Major, "Optimized birefringent filter design for mutli-wavelength operation of Yb-ion lasers", Proc. of SPIE, vol. 10513 (2018).

2. Md. A.R. Reza, R. Akbari and A. Major, “Dual-wavelength Yb:CALGO laser with wavelength spacing tunability”, Proc. of SPIE, vol. 11259 (2020).

[The results from this experiment have been drafted for submission to the Optics Letters journal.]

In chapter 4, the conical refraction output based on the Yb:CALGO laser has been discussed. In the laser setup, the gain medium was separated from the CRE which allowed it to generate an exceptional quality beam with high output power. In addition to that, the tuning and dual-wavelength operations were performed as well using the birefringent filters. This chapter is based on the following publication:

1. Md. A.R. Reza, R. Akbari, K.A. Fedorova, G.S. Soklovskii, E.U. Rafailov, and A. Major, “Diode-pumped Yb:CALGO laser with conical refraction output”, Proc. of SPIE, vol. 11259 (2020).

[The results from this experiment have been drafted for submission to the Applied Physics B journal.]

In chapter 5, the results of the mode-locked Yb:CALGO laser with high peak power have been presented. To get the high peak power, the laser cavity was extended by using a 1:1 imaging telescope. Pulses as short as 81 fs were obtained from this experiment. This chapter is based on the following publication:

1. Md. A.R. Reza and A. Major, “Ultrafast laser sources for nonlinear imaging and spectroscopy with high energy in sub-100 fs pulses”. Proc. of SPIE, vol. 11825 (2021).

[The results from this experiment have been drafted for submission to the Laser Physics Letters journal.]

In chapter 6, the results for the mode-locked laser have been presented where the laser cavity was extended by a White cell configuration. By using simple optics, mode locking at 13.85 MHz, 10.15 MHz and 8.2 MHz repetition rates were observed. From this experiment 68 fs pulses were obtained. This chapter is based on the following publication:

1. Md. A.R. Reza and A. Major, “Low repetition rate Yb:CALGO laser extended with a White cell configuration”. Proc. of SPIE, vol. 11980 (2022).
2. Md. A.R. Reza and A. Major, “Femstosecond extended-cavity Yb:CALGO laser operating at sub-10 MHz repetition rate”. Proc. of SPIE (2023).

[The results from this experiment have been drafted for submission to the Optics Letters journal.]

In chapter 7, the summary of the experiments has been presented, as well as some possible works that might be done with the Yb:CALGO laser have been discussed.

REFERENCES

[1.1] https://en.wikipedia.org/wiki/Laser.

[1.2] R. J. Keyes and T. M. Quist, “Injection Luminescent Pumping of CaF_2:U^{3+} with GaAs Diode Lasers,” Appl. Phys. Lett. 4(3), 50 (1964).

[1.3] F. Druon, F. Balembois, P. Georges, “New laser crystals for the generation of ultrashort pulses” Académie des sciences. Published by Elsevier Masson SAS (2006).

[1.4] A. M. Weiner, “Ultrafast Optics”, published by John Wiley & sons, 2009.

[1.5] W. R. Zipfel, R. M. Williams, and W. W. Webb, "Nonlinear magic: multiphoton microscopy in the biosciences," Nat. Biotechnol. 21, 1369–1377 (2003).

[1.6] D. Kobat, M. E. Durst, N. Nishimura, A. W. Wong, C. B. Schaffer, and C. Xu, "Deep tissue multiphoton microscopy using longer wavelength excitation," Opt. Express 17, 13354 (2009).

[1.7] E. A De Souza, M. C. Nuss, W. H. Knox, and D. A. B. Miller, "Wavelength-division multiplexing with femtosecond pulses," Opt. Lett. 20, 1166 (1995).

[1.8] A. M. Larson, “Multiphoton microscopy,” Nat. Photonics 5, (2011), doi:10.1038/nphoton.an.2010.2.

[1.9] S. Nolte, C. Momma, H. Jacobs, A. Tünnermann, B. N. Chichkov, B. Wellegehausen, and H. Welling, "Ablation of metals by ultrashort laser pulses," J. Opt. Soc. Am. B 14, 2716 (1997).

[1.10] R. a Farrer, M. J. R. Previte, C. E. Olson, L. A. Peyser, J. T. Fourkas, and P. T. C. So, "Single molecule detection with a two-photon fluorescence microscope with fast-scanning capabilities and polarization sensitivity," Opt. Lett. 24, 1832 (1999).

[1.11] R. E, U. Morgner, F. X. Kärtner, J. G. Fujimoto, E. P. Ippen, V. Scheuer, G. Angelow, T. Tschudi, M. J. Lederer, A. Boiko, and B. Luther-Davies, "Generation of 5-fs pulses and octave-spanning spectra directly from a Ti:sapphire laser," Opt. Lett. 26, 373 (2001).

[1.12] P. G. Antal and R. Szipőcs, "Tunable, low-repetition-rate, cost-efficient femtosecond

a. Ti:sapphire laser for nonlinear microscopy," Appl. Phys. B 107, 17–22 (2012).

[1.13] M. T. Asaki, C.-P. Huang, D. Garvey, J. Zhou, H. C. Kapteyn, and M. M. Murnane, "Generation of 11-fs pulses from a self-mode-locked Ti:sapphire laser," Opt. Lett. 18, 977 (1993).

[1.14] A. M. Kowalevicz, Jr., a T. Zare, F. X. Kärtner, J. G. Fujimoto, S. Dewald, U. Morgner, V. Scheuer, and G. Angelow, "Generation of 150-nJ pulses from a multiple-pass cavity Kerrlens mode-locked Ti:Al_2O_3 oscillator," Opt. Lett. 28, 1597 (2003).

[1.15] C. G. Durfee, T. Storz, J. Garlick, S. Hill, J. a Squier, M. Kirchner, G. Taft, K. Shea, H. Kapteyn, M. Murnane, and S. Backus, "Direct diode-pumped Kerr-lens mode-locked Ti:sapphire laser," Opt. Express 20, 13677 (2012).

[1.16] S. Sawai, A. Hosaka, H. Kawauchi, K. Hirosawa, and F. Kannari, "Demonstration of a Ti:sapphire mode-locked laser pumped directly with a green diode laser," Appl. Phys. Express 7, 22702 (2014).

[1.17] P. W. Roth, A. J. Maclean, D. Burns, and A. J. Kemp, "Direct diode-laser pumping of a mode locked Ti:sapphire laser," Opt. Lett. 36, 304 (2011).

[1.18] K. Kuetemeyer, G. Kensah, M. Heidrich, H. Meyer, U. Martin, I. Gruh, and A. Heisterkamp, "Two-photon induced collagen cross-linking in bioartificial cardiac tissue," Opt. Express 19, 15996 (2011).

[1.19] L. DeLoach, S. Payne, L. Chase, L. Smith, W. Kway, W. Krupke, “Evaluation of absorption and emission properties of Yb3+-doped crystals for laser applications,” IEEE J. Quant. Electron. 29, 1179–1191(1984).

[1.20] W. Krupke, “Ytterbium solid-state lasers - the first decade”, IEEE J. Sel. Top. Quantum Electron. 6(6), 1287–1296 (2000).

[1.21] C. Honninger, G. Zhang, and U. Keller, “Femtosecond Yb:YAG laser using semiconductor saturable absorbers”, Opt. Lett. 20 (23), 2402- 2404 (1995).

[1.22] R. Akbari, H. Zhao, K.A. Fedorova, E.U. Rafailov and A. Major, “Quantom-dot saturable absorber and Kerr-lens mode-locked Yb:KGW laser with >450 kW of peak power, Opt. Lett. 41 (16), 3771- 3774 (2016).

[1.23] H. Liu, J. Nees, and G. Mourou, “Diode-pumped Kerr-lens mode-locked Yb:$KY(WO_4)_2$ laser”, Opt. Lett. 26 (21), 1723- 1725 (2001).

[1.24] F. Hoos, S. Pricking, and H. Giessen, “Compact portable 20 MHz solid-state femtosecond whitelight-laser,” Opt. Express 14(22), 10913–10920 (2006).

[1.25] P. Sevillano, G. Machinet, R. Dubrasquet, P.Camy, J._L. Doualan, R. Moncorge, P. Georges, F. Druon, D. Descamps, and E. Cormier, “Sub-50 fs, Kerr-lens mode-locked

$Yb:CaF_2$ laser oscillator delivering up to 2.7 W", Advanced solid-state laser congress technical digest (2013).

[1.26] A. Greborio, A. Guandalini, and J. A. D. Au, "Sub-100fs pulses with 12.5 W from Yb: CALGO based oscillators", Proc. of SPIE Vol. 8235 823511-1 (2012).

[1.27] J. Petit, P.Goldner, and B. Viana, " Laser emission with low quantum defect in $Yb:CaGdAlO_4$", Opt. letters, 30(11), 1345- 1347 (2005).

[1.28] Di, J.Q.; Xu, X.D.; Xia, C.T.; Zheng, L.H.; Aka, G.; Yu, H.H.; Sai, Q.L.; Guo, X.Y.; Zhu, L. "Crystal growth, polarized spectra, and laser performance of Yb:CaGdAlO4crystal." Laser Phys. 2016, 26, 045803.

[1.29] Boudeile, J.; Druon, F.; Hanna, M.; Georges, P.; Zaouter, Y.; Cormier, E.; Petit, J.; Goldner, P.; Viana, B. "Continuous-wave and femtosecond laser operation of $Yb:CaGdAlO_4$ under high-power diode pumping."Opt. Lett. 2007, 32, 1962–1964.

[1.30] H.Wang, J. Pan, Y. Meng, Q. Liu and Y. Shen, "Advances of Yb:CALGO laser crystals" Crystals, 11 (9), 1131 (2021).

[1.31] F. Auzel, "On the maximum splitting of the ($^2F_{7/2}$) ground state in Yb^{3+}-doped solid state laser materials," J. Lumin. 93, 129-135 (2001).

[1.32] T. Y. Fan, "Optimizing the Efficiency and Stored Energy in Quasi-Three-Level Lasers," IEEE J. Quantum Electron. 28, 2692-2697 (1992).

[1.33] T. Taira, W. M. Tulloch, and R.L. Byer, "Modelling of quasi-three-level lasers and operation of cw Yb:YAG laser", App. Opt., 36(90), 1867-1874 (1997)

[1.34] P. Loiko, F. Druon, P. Georges, B. Viana and K. Yumashev, "Thermo-optic characterization of $Yb:CaGdAlO_4$ laser crystal", Optical material express, Vol.4 No. 11, 2241-2249(2014).

[1.35] R. Gaume, B. Viana, D. Vivien, J. P. Roger, D. Fournier, J. P. Souron, G. Wallez, S. Chenais, F. Balembois, and P. Georges, "Mechanical, thermal and laser properties of $Yb:(Sr_{1-x} Ca_x)_3Y(BO_3)_3$ (Yb:CaBOYS) for 1 μm laser applications," Optical Materials 24, 385-392 (2003)

[1.36] Y. Zaouter, J. Didierjean, F. Balembois, G.L. Leclin, F. Druon, and P. Georges, "47-fs diode- pumped Yb^{3+}: $CaGdAlO_4$ laser, Optics Letter, vol.31 no.1, 119-121 (2006).

[1.37] www.eksmaoptics.com

Chapter 2
Estimation of the intracavity losses in a continuous-wave Yb:CALGO laser

The knowledge of the intracavity losses arising from various laser components is crucial for efficient laser operation. Traditional loss estimation method such as Findlay-Clay analysis or the numerical modeling method is good for a four-level laser system, however, for quasi-three-level laser system the spectroscopic gain analysis is a more reliable and simple technique. In this chapter, the result of the losses based on the spectroscopic gain analysis method has been discussed. A comparison with the traditional gain analysis methods has been presented as well.

2.1 Introduction

One of the most important factors to ensure the efficient operation of the laser sources is to keep the intracavity losses as low as possible. Besides reducing the lasing efficiency, intracavity losses can cease the lasing in the worst-case scenario. Although the intracavity losses are unavoidable as the sources are from the laser cavity mirrors, laser crystals, reabsorption loss in quasi-three-level laser, non-saturable losses in semiconductor saturable absorber mirrors (SESAM) etc., a careful laser operation with minimum intracavity losses can minimize their impact [2.1]. There are different techniques that can be used for intracavity loss estimation in lasers. Traditionally loss estimation was done by using Findlay-Clay analysis [2.2] and numerical methods which are good to measure losses at laser threshold in four-level laser systems [2.3-2.7]. Zhao et al. showed that these methods can be erroneous for quasi-three-level laser systems [2.1]. Also, the measurement might add some error above the laser threshold. It was also shown that, estimating the intracavity losses based on spectroscopic gain could be simple, dynamic and gives accurate measurements above the laser threshold and it can be applicable for quasi-three level lasers [2.1]. In this work, the loss estimation for a continuous-wave Yb:CALGO laser by spectroscopic gain method, Findlay-Clay analysis and numerical method has been demonstrated with a detailed discussion of the methods in the next sections. By using the spectroscopic gain analysis method, the loss was between 2.3%-3.3%. Based on the Finlay-Clay analysis method, the estimated loss was about 3.5%. From the numerical calculation, the estimated the loss was between 3%-3.7% for different output couplers.

2.2 Sources of intracavity losses

Intracavity losses are unavoidable parasitic losses that have a bad impact on the output power. Especially for a lower output coupler, the output power is very sensitive to intracavity losses. In case of significant intracavity losses, the output may be ceased. Below are some sources of intracavity losses:

(i) Cavity mirrors

The cavity mirrors are supposed to be highly reflective at lasing wavelengths. However, an imperfection in the coating of the cavity mirrors leads to leakage of the intracavity power which ultimately increases the losses. For example, the imperfection in the dichroic mirror causes to emit the intracavity power which will reduce the efficiency of the laser. Also, the cavity mirrors should be neat and clean. If it has dust particles on it, it will cause scattering losses.

(ii) Reabsorption losses

The reabsorption losses are a very common phenomenon in a quasi-three-level laser. The reason is that because of the small Stark splitting of the ground level, a small number of electrons are thermally excited to E_1 level which causes the reabsorption of lasing photons as shown in figure 2.1(a). In the case of a four-level laser system, due to the large energy difference between E_0 and E_1, reabsorption losses are not possible which is shown in figure 2.1(b). For an end-pumped laser, the reabsorption losses play a very important role in determining the efficiency. For highly efficient laser operation, the overlap between the pump beam and laser beam in the gain medium is very important. We can minimize the intracavity losses with good overlap. However, due to the thermal lensing effect, sometimes the laser beam becomes larger than the pump beam which causes reabsorption losses.

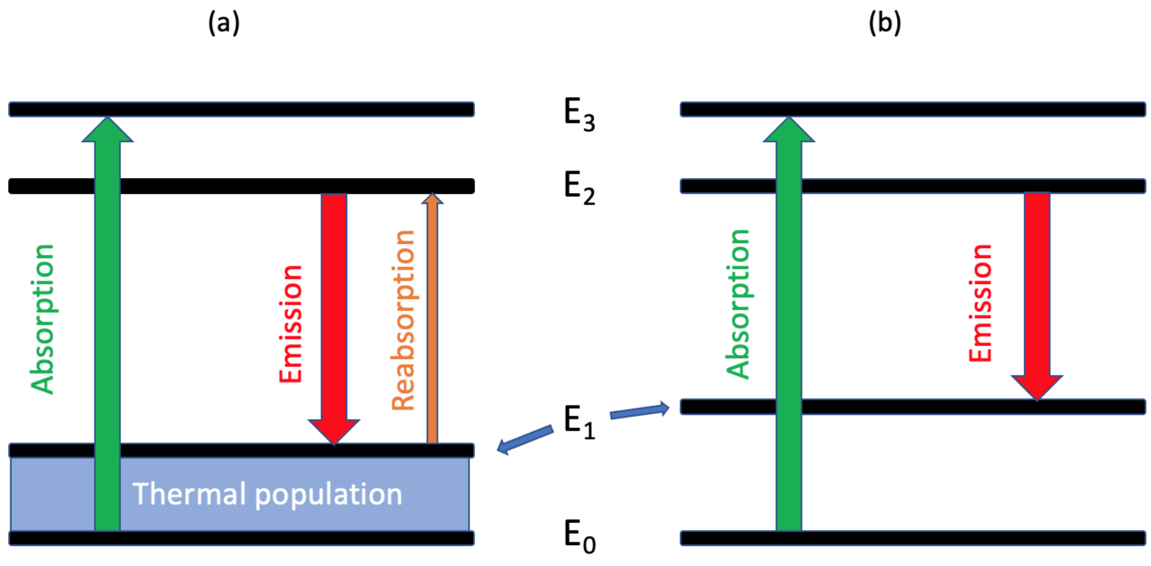

Figure 2.1: Energy level diagram and main transitions for (a) quasi-three-level and (b) four-level lasers.

(iii) Losses from SESAM

Semiconductor saturable absorber mirror (SESAM) is used in a laser cavity to lock all the longitudinal modes in phase to generate ultrashort pulses. Light with low intensity will be absorbed while very high-intensity pulses will be reflected. If the coating on the SESAM has leakage, then the reflection is not 100%. This loss contributes to the intracavity loss.

(iv) Losses from a laser crystal

The trivalent rare-earth ions doped crystals are used as a gain medium for the solid-state laser. The crystal should be transparent i.e., with low absorption and low scattering at the laser wavelengths. The impurities and defects in the laser crystal can enhance absorption and scattering losses. The surfaces through which laser beam passes should be at Brewster's angle or antireflection coated. Imperfect coatings can increase the losses.

2.3 Experimental setup

In the intracavity loss estimation experiment, a 5 mm long *a*-cut 2 at. % doped Yb: CALGO (Castech) crystal was pumped by a fiber-coupled laser diode at 979 nm. The fiber core diameter was 105 µm and the numerical aperture was 0.22. Both ends of the crystal were antireflection coated to minimize the intracavity losses and it was also wrapped with indium foil to improve heat removal. Unpolarized light from the laser diode was imaged into the Yb:CALGO crystal by using two lenses of 50 mm and 150 mm focal length. The resultant spot size was 315 µm in diameter. To ensure that the cavity mode stays inside the pumping zone and the laser beam spot size was 280 µm in diameter which was estimated based on ABCD matrix analysis. The cavity design was done by considering the thermal lensing issues and the crystal was water-cooled to maintain the temperature around 18 °C. About 56% of the pump power was absorbed in the laser crystal without any lasing in the cavity. The laser cavity is shown in figure 2.2. The output power was monitored by a power meter. A spectrometer (Anritsu MS2687B) with fine resolution (0.1 nm) was used to record the laser spectrum.

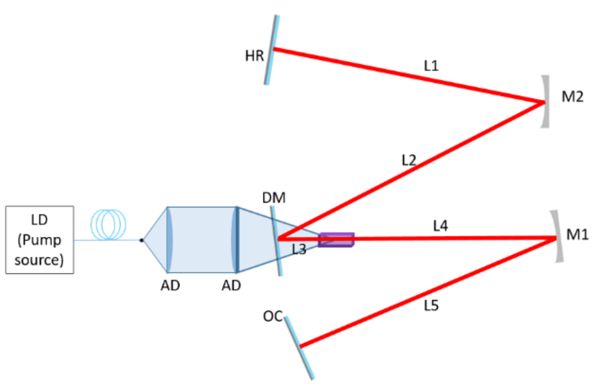

Figure 2.2: Schematic of the continuous-wave Yb:CALGO laser cavity used for intracavity loss. AD: achromatic doublet, DM: dichroic mirror, Radii of curvature of the curved mirrors: M1 = -600 mm, M2 = -600 mm, DM = Dichroic mirror, OC = output coupler, L1 = L5 = 700 mm, (L2+ L3) = L4 = 324 mm.

The actual photo of the experimental setup is shown in figure 2.3 with different components used in the laser cavity as described above in figure 2.2.

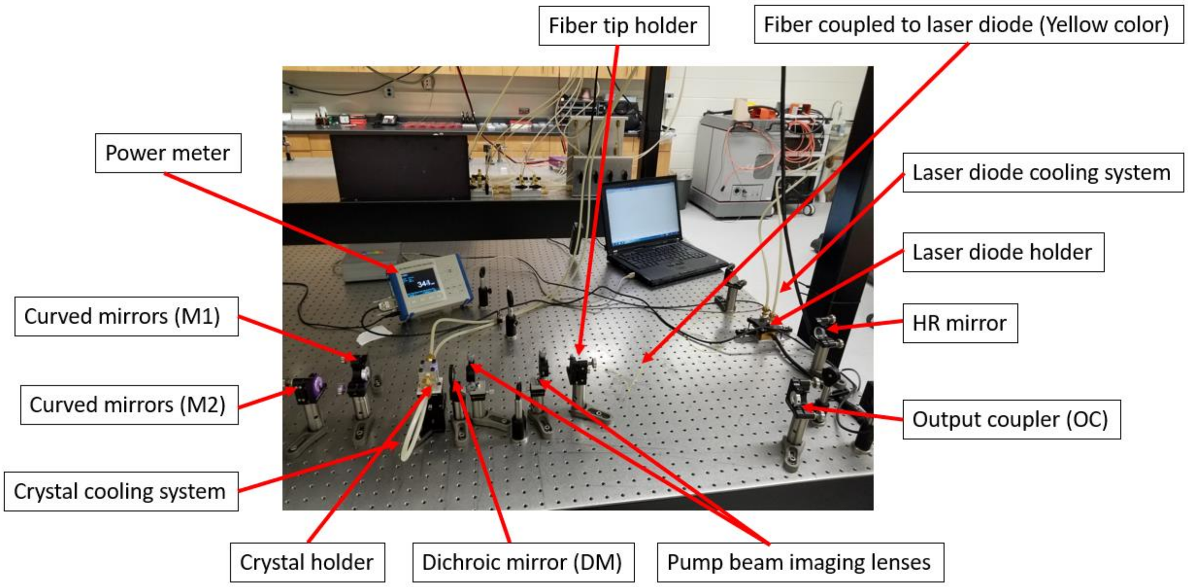

Figure 2.3: Photo of the experimental setup.

2.4 Results and discussion

The laser performance was initially evaluated with different output couplers with transmissivity from 0.8% to 10%. As stated in Ref. 1 that the loss estimation based on the spectroscopic gain analysis method could introduce unreliable loss estimation for too large or too small losses, so the experiment was continued for the above-mentioned output couplers. The highest output power (5.95 W) was obtained with a 10% output coupler at 25 W of incident pump power. The output power for different output couplers at different incident pump power is shown in figure 2.4(a). The beam quality factor was also measured, and it was close to 1 which is shown in figure 2.4(b).

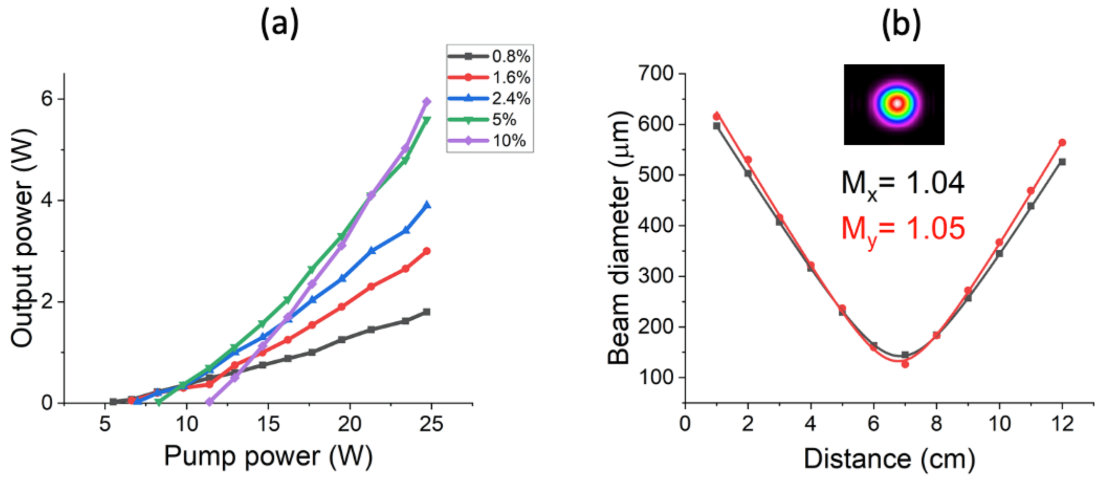

Figure 2.4: (a) The recorded output power for different output couplers with the change in the incident pump power, (b) beam quality factor with transverse beam intensity profile.

The impact of intracavity losses on the laser efficiency is profound so it is very important to estimate the intracavity losses in the laser cavity. Findlay and Clay proposed a model to estimate the losses in a four-level laser system [2.2]. The model was based on the fact that the peak gain of a laser system is spectrally independent of the loss. This makes a linear relationship between the logarithm of the output coupler reflectivity and the threshold pump power. To estimate the intracavity losses based on this Findlay-Clay method, one needs to use several output couplers and determine the threshold pump power for each of these output couplers. Though this model is completely reliable for a 4-level laser system, in quasi-three-level lasers the reabsorption loss plays a vital role which is also wavelength dependent. Because of this wavelength dependency of the gain and loss for quasi-three-level lasers, the linear relationship cannot estimate the losses accurately. Also, it is important to estimate the intracavity losses above the laser threshold to maintain efficient operation which cannot be done using the Findlay-Clay analysis as it can give a measure of losses at laser threshold only. Zhao et al. showed that spectroscopic gain analysis can be a good candidate for dynamic loss estimation in quasi-three-level lasers [2.1]. This model was based on the fact that the peak gain coefficient of the quasi-three-level lasers is dependent on the loss. In steady-state laser operation, the overall losses would be balanced by the gain which can be expressed by:

$$R_{oc}(1-L_{in})\exp[g(\lambda_L)]=1 \quad (2.1)$$

where R_{oc}= reflectivity of the output coupler, L_{in} = roundtrip intracavity loss and $g(\lambda_L)$ = wavelength dependent effective gain coefficient. If one knows the gain-coefficient values, then one can get the corresponding intracavity loss from equation 1. The gain-coefficient determines the output oscillating wavelength, and one can find its value based on the following equation [2.8]:

$$g(\lambda_L) = 2N_0 l_c[\beta(\sigma_{abs}(\lambda_L)+\sigma_{em}(\lambda_L))-\sigma_{abs}(\lambda_L)] \quad (2.2)$$

where N_0 = doping concentration, l_c = length of the crystal, $\sigma_{abs}(\lambda_L)$ & $\sigma_{em}(\lambda_L)$ = absorption and emission cross-sections at lasing wavelength, respectively, β= fractional population inversion. The variation in the peak of the gain-coefficient for a 5 mm long Yb:CALGO laser for different β values is shown in figure 2.5. The graph is based on equation 2.2, where the absorption and emission cross-sections data were provided by P. Loiko [2.9].

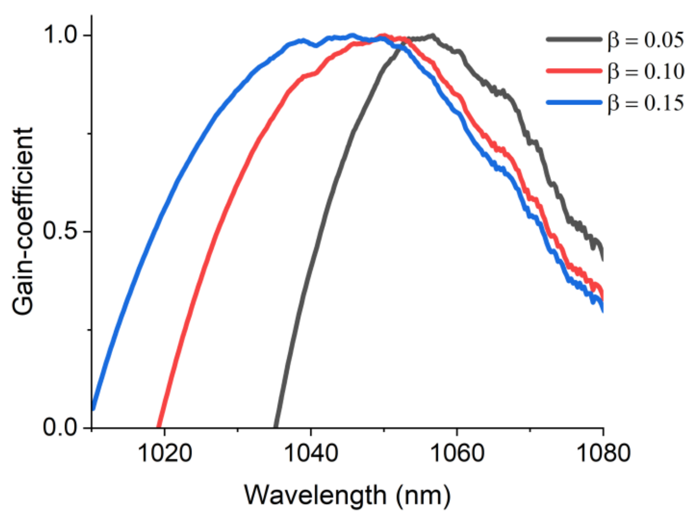

Figure 2.5: Variation in gain co-efficient for different β values.

This spectroscopic gain analysis technique allows measuring the intracavity loss at any power level without the need to use multiple output couplers. Just one output coupler can give the loss estimation based on the above equations. The lasing wavelength λ_L, the fitted fractional population inversion β, the gain coefficient $g(\lambda_L)$ at the lasing wavelength, and the calculated intracavity losses (L_{in}) are listed in Table 1. The lasing spectra and the calculated gain spectrum for different output couplers are shown in figures 2.6(a) - 2.6(e). For all the output couplers the emission spectrum was recorded at 25 W of incident pump power and no shift in wavelength was observed with the variation in pump power. The calculated intracavity loss was ~2.3%-3.3% for different output couplers. The variation in the intracavity losses between the different output couplers might be coming from the residual misalignment after changing them and another source could be the variation in the cavity mirror reflectivity in 1045-1055 nm wavelength range. The resolution of the spectrometer (Anritsu MS2687B) was 0.07 nm and it could limit the accuracy of the measurement as well. The absorption and emission spectra values for this experiment were measured at room temperature [2.9] and these values are dependent on the temperature, therefore it can add some errors in the calculation as well. The laser setup was a tabletop set up and it was operated in a cleanroom environment. As the setup was not covered, therefore the dust particles and related scattering might be a variant as well.

Table 2.1: Intracavity losses for different output couplers based on spectroscopic gain analysis method. Here, T_{oc} = transmission of output coupler, λ_L= lasing wavelength, β = fractional population inversion, $g(\lambda_L)$ = wavelength dependent effective gain coefficient, L_{in} = intracavity losses.

T_{oc}	λ_L (nm)	β	$g(\lambda_L)$	L_{in} (%)
0.8	1054.94	0.047	0.033	2.47
1.6	1053.34	0.051	0.038	2.28
2.4	1052.54	0.063	0.0541	2.94
5	1049.28	0.086	0.0852	3.33
10	1045.84	0.123	0.139	3.30

The losses based on spectroscopic gain analysis could be erroneous when the losses introduced by the output coupler are too high or too low as the gain spectrum could be comparatively flat or the longer wavelengths could cause weak reabsorption losses [2.1]. Therefore, it is important to determine the range of acceptable loss. Based on the equation 1, the total loss i.e. (R_{oc} + L_{in}) vs the calculated lasing wavelength could give an idea about that which is shown in figure 2.6(f). At the lower loss level, the lasing wavelength has a high variation which translates into a broad/multipeak laser spectrum and at the high-level loss the lasing wavelength becomes almost invariable due to the flat gain spectrum, so the range of losses in between these two could give reliable loss estimation. Based on figure 2.6(f), this range is approximately 3%-22% for this experiment.

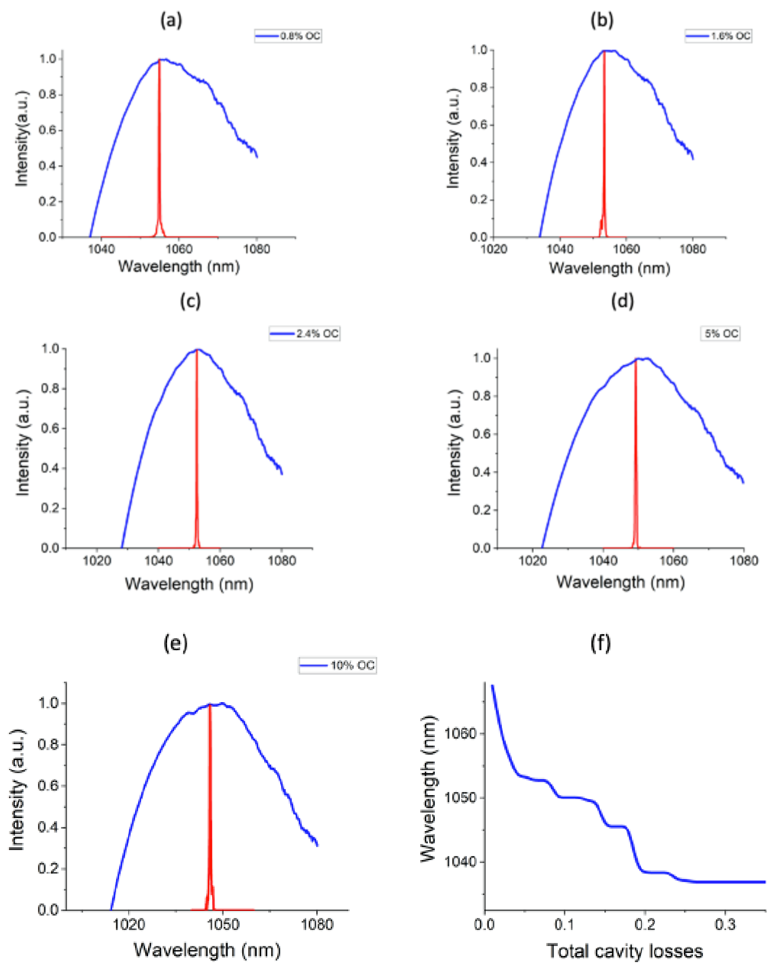

Figure 2.6: (a)-(e) The lasing spectra (red lines) and the calculated gain spectra (blue lines) for different output couplers, (f) the variation in calculated lasing wavelength with the total cavity loss.

The loss was also estimated by using the Findlay-Clay analysis. The main equation of this technique can be re-written by including the reabsorption loss as below [2.2]:

$$P_{th} = K\ (\ L_{in} - ln(R_{oc}) + \ \delta_{reabs}) \tag{2.3}$$

where P_{th} = threshold pump power, R_{oc} = reflectivity of output coupler, L_{in} = roundtrip intracavity loss and K is a constant. The reabsorption loss can be defined as $\delta_{reabs} = 2N_o l_c \sigma_{abs}(\lambda_L)$ [2.1] where N_o is the doping concentration, l_c is the crystal length. For this experiment, the threshold pump power (P_{th}) was determined by using a viewing card to visually find a point when the lasing ceased while reducing the incident pump power. As it can be seen from figure 2.7, the relationship between the threshold pump power and the ln (R_{oc}) is almost linear. The intercept of the linear fit with the x-axis from this graph will yield the overall cavity loss. From figure 2.7, it can be seen that the overall cavity loss (excluding the loss of the output coupler) is 7%, and the average reabsorption loss is about 3.5 % which will give an estimated intracavity loss of 3.5%.

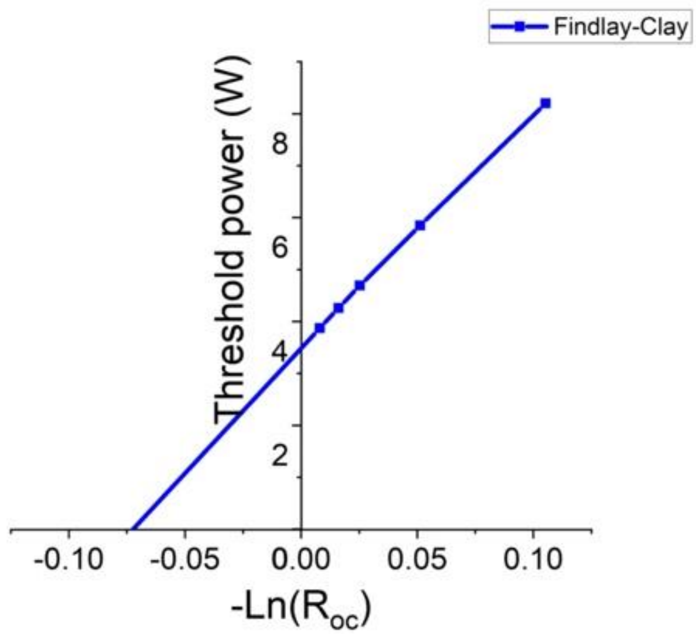

Figure 2.7: Loss estimation by a linear curve fitting based on the Findlay-Clay method.

Taira et al. modelled the laser performance of the end-pumped quasi-three-level oscillator considering the reabsorption losses [2.4]. The threshold pump power (P_{th}) was calculated based on the following equation:

$$P_{th} = \frac{\pi h \upsilon_p \, (W_{ap}^2 + W_l^2)}{4\tau[\, \sigma_{abs}(\lambda_L) + \sigma_{em}(\lambda_L)](f_u + f_l)} \; (T_{oc} + L_{in} + \delta_{reabs}) \qquad (2.4)$$

where $h\upsilon_p$= pump photon energy, the lifetime of the upper laser level for Yb:CALGO is 420 μs. The fractional populations for the upper and lower laser levels were f_u= 0.703, f_l= 0.053, and were calculated based on the energy levels of Yb:CALYO as this should have closer characteristics with Yb:CALGO [2.10]. Considering the pump beam quality factor of the laser diode, the average pump beam spot size was *Wap* = 195 μm [2.11]. Toc is the transmission of the output coupler, and the emission, absorption spectra and reabsorption loss (δ_{reabs}) are wavelength-dependent parameters. As all the parameters of equation 4 is known, we can calculate the intracavity loss from this equation. The calculated intracavity losses for the corresponding output couplers are shown in table 2.2. The numbers could include errors as well. It might come from the finite accuracy of the power meter that was used to measure the power and the uncertainty of the overlap between the pump spot size and laser spot size due to the thermal lensing effect. Also, the laser mode and the pump sizes were not measured.

Table 2.2. Calculated intracavity loss for different output couplers based on equation 4.

T_{oc} (%)	σ_{em} (10^{-25}×m^2)	σ_{abs} (10^{-26}×m^2)	δ_{reabs}	P_{th} (W)	L_{in} (%)
0.8	5.01	1.09	2.72	3.87	3.66
1.6	5.28	1.23	3.07	4.26	3.65
2.4	5.35	1.29	3.22	4.69	3.66
5	5.62	1.56	3.9	5.85	3.26
10	5.87	1.93	4.67	8.2	3.00

2.5 Conclusion

In conclusion, the intracavity loss of a diode-pumped continuous-wave Yb:CALGO laser has been estimated by using the spectroscopic gain analysis method, which is a dynamic and effective method to measure the losses above the laser threshold. For this experiment, the loss was 2.3%-3.3% using the spectroscopic gain analysis method. To compare with the traditional methods, losses were also estimated based on the Findlay-Clay analysis method and a numerical model. The loss using the Findlay-Clay analysis was 3.5 % and 3%- 3.66% for different output couplers based on numerical method. The traditional models can estimate losses only at the laser threshold. However, it is important to know about the losses above the laser threshold to enable an efficient laser operation. The spectroscopic gain analysis method is definitely a good choice to estimate the losses above the threshold. Although the absorption and emission spectra data we used in this experiment were recorded at room temperature, for more accurate measurement temperature-dependent absorption and emission cross-sections should be used. Hopefully, this estimation of the loss will facilitate high-power laser operation both in CW and mode-locked regimes.

REFERENCES

[2.1] H. Zhao and A. Major," Dynamic characterization of intracavity losses in broadband quasi-three-level lasers", Opt. Express 22(22), 26651-26658 (2014).

[2.2] D. Findlay,and R.A. Clay,"The measurement of internal losses in 4-level lasers," Phys. Lett., 20(3), 277–278 (1966).

[2.3] W.P. Risk, "Modeling of longitudinally pumped solid-state lasers exhibiting reabsorption losses", J.Opt.Sc.Am.B, 5(7), 1412-1423(1988).

[2.4] T. Taira, W. M. Tulloch, and R.L. Byer, "Modelling of quasi-three-level lasers and operation of cw Yb:YAG laser", App. Opt., 36(90), 1867-1874 (1997)

[2.5] T.Y.Fan, "Optimising the efficiency and stored energy in quasi-three-level lasers" IEEE J. Quantum Electron. 28(12), 2692-2697 (1992).

[2.6] T.Y. Fan, "Diode-pumped solid-state lasers" Lincoln lab J., 3, 413-425 (1990).

[2.7] P. Lacovara, H.K. Choi, C.A. Wang, R.L, Aggarwal, and T.Y. Fan, "Room temperature diode-pumped Yb:YAG laser", Opt. Lett.,16, 1089-1091(1991).

[2.8] C. Hönninger, R. Paschotta, M. Graf, F. Morier-Genoud, G. Zhang, M. Moser, S. Biswal, J. Nees, A. Braun, G. A. Mourou, I. Johannsen, A. Giesen, W. Seeber, and U. Keller, "Ultrafast ytterbium-doped bulk lasers and laser amplifiers," Appl. Phys. B 69, 3-17 (1999)

[2.9] Loiko, P., Serres, J.M., Mateos, X., Xu, X., Xu, J., Jambunathan, V., Navratil, P., Lucianetti, A., Mocek, T., Zhang, X., Griebner, U., Petrov, V., Aguiló, M., Díaz, F. and Major, A., "Microchip Yb:$CaLnAlO_4$ lasers with up to 91% slope efficiency," Opt. Lett. 42(13), 2431-2434 (2017).

[2.10] J. A. Hutchinson, H. R. Verdun, B. H. T. Chai, B. Zandi and L. D. Merkle, "Spectroscopic evaluation of CaYALO4 doped with trivalent Er, Tm, Yb and Ho for eye safe laser applications", Opt. Mat. 3, 287- 306 (1994).

[2.11] I. D. Lindsay and M. Ebrahimzadeh, "Efficient continuous-wave and Q-switched operation of a 946-nm Nd:YAG laser pumped by an injection-locked broad-area diode laser," Appl. Opt. 37(18), 3961–3970 (1998).

Chapter 3

Dual-wavelength operation of a diode-pumped continuous-wave Yb:CALGO laser based on optimized off-surface axis birefringent filter

In continuous-wave operation, the laser line with the highest gain can reach the lasing threshold and after amplification, a single wavelength emission can be obtained. Other laser lines with comparatively weaker gains die out in the competition. But if an equal gain can be maintained for two different laser lines, then both will oscillate in the cavity and as a result dual-wavelength laser can be created and explored. In this chapter, the discussion will be focused on the dual-wavelength laser output from the continuous-wave Yb:CALGO laser by using an optimized off-surface axis birefringent filter.

3.1 Introduction

Continuous-wave dual-wavelength (DW) lasers with wavelengths separated by a few THz are popular for their applications in imaging and spectroscopy [3.1], THz generation [3.2,3.2], astronomy [3.3], optical coherence tomography [3.4], medical and pharmaceutical applications [3.5,3.6].

Different techniques can be used to equalize the gain of two different spectral lines in a broadband laser emission spectrum which can then generate two wavelengths simultaneously in the laser output. For example, DW laser operation was demonstrated using two etalons [3.7]. Another interesting work on DW lasers was done by using two chirped volume Bragg gratings [3.8]. Apart from these techniques, some other techniques such as moving mirror techniques [3.9], two adjacent pump spots in a crystal [3.10], polarization-dependent thermal lensing and reabsorption loss [3.11,3.12] were used to generate DW output. Recently, DW radiation was generated in a much simpler configuration only by inserting a birefringent filter (BRF) in the laser cavity [3.13-3.15].

BRF introduces a periodic loss in the cavity and the free spectral range (the wavelength separation between the generated wavelengths, FSR) depends on the thickness of the birefringent plate [3.16]. The on-surface axis BRF is also called the traditional BRF because the optic axis is located on its surface. With a traditional BRF, the wavelength separation between the generated wavelengths is fixed, i.e. if one wants to change the wavelength separation at the laser output, then one need to use a BRF with a different thickness. On the other hand, it was shown previously that when the optical axis is positioned at an angle to the filter surface, the filtering characteristics are considerably altered. Those BRFs are known as off-surface axis BRFs or diving axis BRFs [3.16-3.21].

For DW operation, rare-earth-doped materials (Yb^{3+}, Nd^{3+}) are popular because of their large emission cross-section, the low thermal effect and the ability to produce higher output power for diode pumping operation. Although Nd-ion doped materials were previously used for multi-color operation, their limited gain-bandwidth [3.22] restricts multi-color operation only to discrete wavelength pairs [3.23]. On the other hand, Yb-ion laser crystals are suitable candidates for multi-color operation because of their broader gain-bandwidths what was presented in chapter 1, and it was also shown that compared to other Yb-ion lasers, Yb:CALGO has approximately 50 nm emission bandwidth which is better compared to other Yb-ion lasers and suitable for this dual-wavelength tuning experiment as well.

In this work, the first goal was to determine an optimum design for an off-surface axis BRF. After choosing the optimized BRF, the second goal was to minimize wavelength separation between the generated laser lines. In Ref. 3.3, it was stated that for some astronomical applications, one needs to have ~1-6 THz sources which corresponds to 4 nm - 22 nm wavelength separation. As the wavelength separation between the two transmission peaks of a dual-wavelength is inversely proportional to the thickness of the BRF plate, therefore the experiment was done by using a 12 mm and 24 mm BRF plate as this will help to get minimum wavelength spacing of around 5 nm. The results of the experiment using the optimized BRFs will be discussed in the results section of this chapter.

3.2 Designing of an off-surface axis BRF

In this part, the simulation results of various filtering properties of a laser resonator that contains a quartz BRF with an optic axis pointing out of its surface will be discussed. A BRF with a properly selected optic axis orientation exhibits a wide variation of the parameter values such as free spectral range, modulation depth and bandwidth [3.17,3.18]. As a consequence, there is no necessity to use several BRFs of different thicknesses to obtain different sets of multicolor wavelength pairs [3.17].

Consider figure 3.1where light is incident obliquely on a BRF plate at an angle of Φ_0 where L is the thickness of the plate, the optic axis lies at an angle of θ with respect to the surface and α is the angle between the optic axis of the BRF plate and the plane of incidence (i.e. the rotation angle) [16].

The loss properties of a BRF vary with wavelength. This is caused by the wavelength-dependent phase retardation owing to the birefringence of the BRF material and can be written as [3.16]:

$$\varphi = sin^2\gamma(\kappa\delta l/\cos\phi) \tag{3.1}$$

$$sin^2\gamma = cos^2\theta\ sin^2\alpha + (cos\phi\ cos\theta\ cos\alpha - sin\phi\sin\theta) \tag{3.2}$$

where φ is the phase retardation because of the birefringence, wavenumber, $\kappa = 2\pi/\lambda$, $\delta = n_e - n_o$ is the difference between the ordinary and extraordinary refractive indices, ϕ is the refraction angle of the ordinary ray which is approximately 33° for a quartz BRF plate inserted at Brewster's angle [3.14, 3.16].

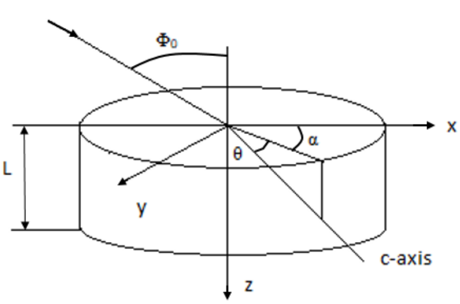

Figure 3.1: Birefringent filter showing notations used in the calculations.

The BRF will create a wavelength-dependent loss because of the change in the polarization of intracavity laser radiation. In addition to that, the thickness of the BRF plate, its rotation angle (α) and the angle between the plate surface and an optical axis play an important role in loss behavior. The theoretical background of transmission characteristics [3.16] has been discussed in detail in the Appendix A. An important property of the BRF is the modulation depth (MD) [3.25]. Modulation depth of the BRF shows the relative loss for the neighbouring wavelengths with respect to the transmission peak. Modulation depth can be calculated based on the following equation:

$$MD = 4\cos^2 m \sin^2 m \tag{3.3}$$

where $cosm = sin\alpha \sin\phi \,/ sin\gamma$. Another important property of the BRF is the free spectral range (FSR) [3.24] which is the wavelength separation between two transmission peaks. The FSR can be determined by the following equation:

$$FSR = \frac{\lambda^2 sin\,\phi}{\delta d sin^2 f} \tag{3.4}$$

where $f = arccos\,(cos\alpha \cos\phi \, cos\theta + sin\phi \, sin\theta)$.

First, the discussion will be focused on the variation of transmission characteristics with the change in the position of the optical axis with respect to the filter surface (θ) as a function of the plate rotation angle (α). A dual-wavelength operation frequency difference of 4.65 THz (16.7 nm wavelength separation) was reported for Yb:KGW with a 6 mm-thick regular BRF [3.14]. In the next section of the thesis, the variation in the transmission properties of the BRF filter for a 6 mm thick BRF will be discussed for for θ=45° and θ= 0° in a similar manner as in Ref. 3.17.

Figure 3.2 shows the transmission characteristics of a laser cavity that has a 6 mm thick BRF, the optical axis of which lies at an angle of 45° with respect to the plate surface, as a function of plate rotation angle from 15° to 115°. Since BRF characteristics for rotation angles from 0° to 180° are the same as from 180° to 360°, therefore the discussion will be focused on rotation angles only from 0° to 180°. From figures 2(a) and 2(b), it can be seen that the filtering properties such as modulation depth, free spectral range and full width at half maximum (FWHM) of transmission peaks change as the filter was rotated.

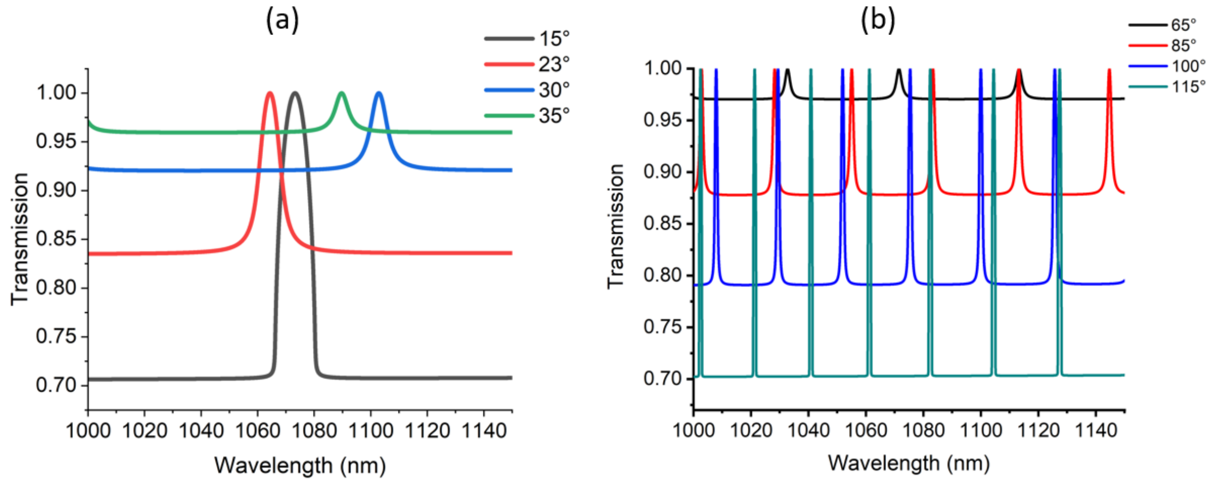

Figure 3.2: Calculated transmission characteristics of a laser cavity with a BRF for its different rotation angles. A 6 mm thick BRF with the optical axis at 45° with respect to its surface was used for calculations. (a) Rotation angles from 15° to 35° and (b) from 65° to 115°.

On the other hand, figure 3.3 shows the transmission characteristics of the laser cavity that has a regular 6 mm thick BRF (i.e. the optical axis lies at an angle of 0° with respect to plate surface) as a function of its rotation angle from 15° to 115°.

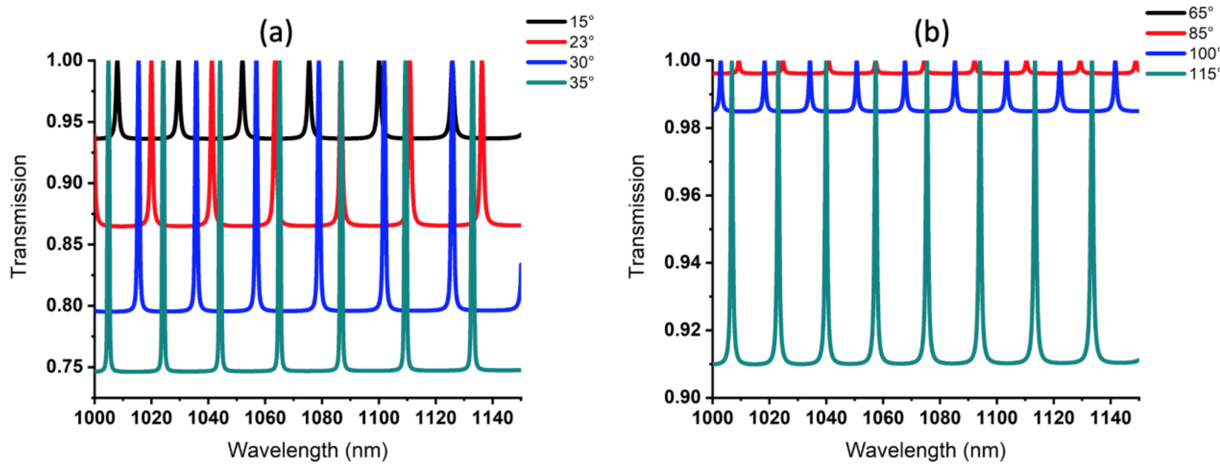

Figure 3.3: Calculated transmission characteristics of a laser cavity with a regular BRF for its different rotation angles. (a) Rotation angles from 15° to 35° and (b) from 65° to 115°.

When compared to figure 3.2, it is clear that the mentioned BRF properties do not change as much with the rotation angle. From this example, one can clearly see that the flexibility in terms of parameters offered by the regular, on-surface optic axis, BRF is quite limited when compared to the BRF which has an optical axis pointing out of the plate surface [3.17].

An alternative way to investigate the transmission characteristics of a BRF is presented in figure 3.4. Figure 3.4(a) shows the transmission characteristics around 1050 nm as a function of BRF rotation angle whose optical axis lies at an angle of 45° with respect to its surface and figure 3.4(b) shows the transmission characteristics for the regular BRF. The selected wavelength of 1050 nm matches the emission of the Yb:CALGO and other Yb-ion doped crystals. Comparing these two graphs from figure 3.4, it can be concluded that the off-surface BRF with θ=45° has different transmission maxima which are not evenly distributed and also have different FWHMs. In contrast, for the conventional BRF, the transmission maxima are evenly spaced and have similar linewidth [3.17].

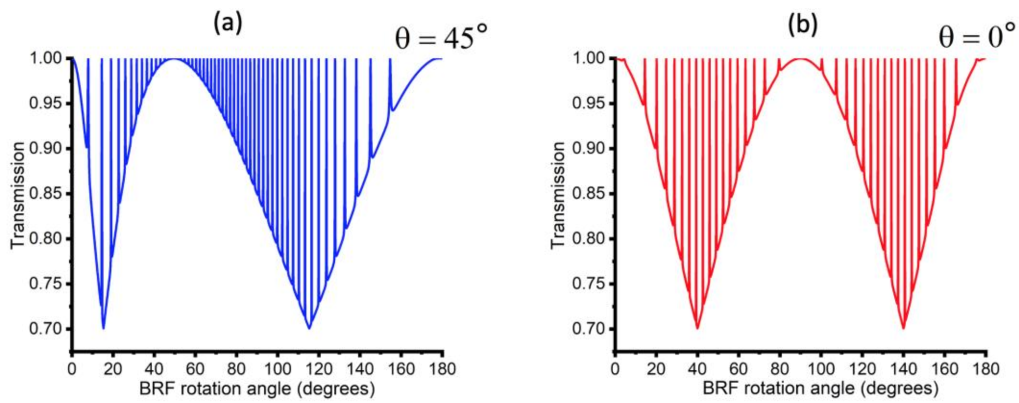

Figure 3.4: Calculated variation of transmission as a function of the BRF plate rotation angle at 1050 nm for a laser cavity with a 6 mm thick BRF. Optical axis of the BRF lies at an angle of 45° (a) and 0° (b) with respect to the filter surface.

Based on the above discussion one can see that the off-surface optical axis BRF has more rich filtering characteristics than the conventional one. Therefore, one needs to find out the position of the optical axis with respect to the filter surface which will yield the best performance. A BRF which can produce variable FSR values and high modulation depth (MD) which remains constant for a large range of rotation angles can be considered as the best one for our purpose. Next, the discussion will be focused on the FSR and modulation depth parameters for various θ values in order to determine which position of the optical axis will yield the best result.

First, the effect of the BRF optical axis orientation on its FSR will be presented. The calculations were performed at 1050 nm for different optical axis positions varying from 0° to 90° for a 6 mm thick BRF plate. As can be seen, when the optical axis lies on the BRF surface, i.e. θ=0°, the FSR values become quite low and fairly constant.

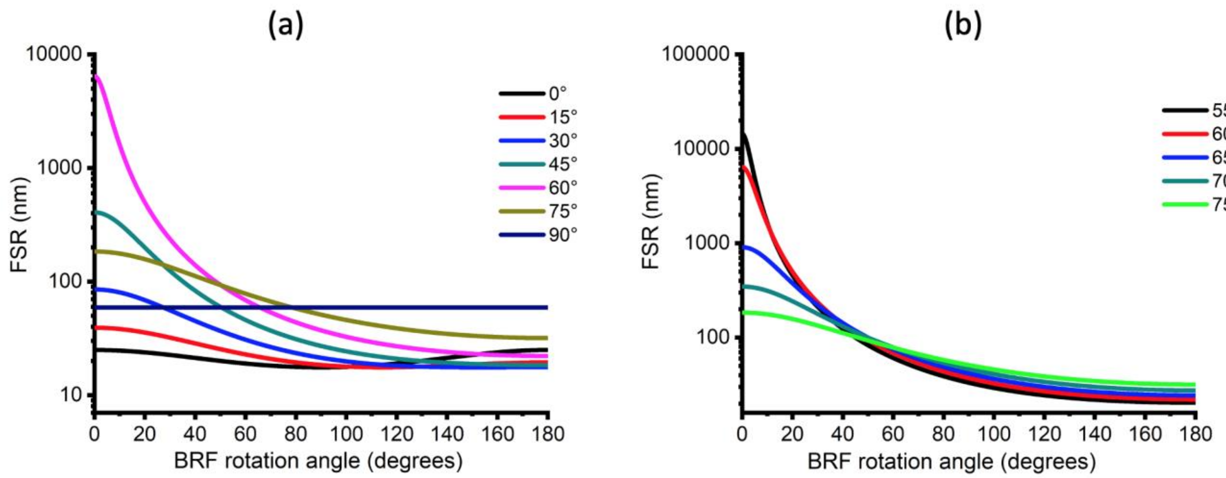

Figure 3.5: Variation of free spectral range with plate rotation angle for a 6 mm-thick BRF plate at 1050 nm with different values of the optical axis off-surface angle values. (a) Off-surface angles θ in the 0° to 90° and (b) in the 55° to 75° ranges.

From figure 3.5(a) it can be seen that the largest FSR variation occurs for θ around 60°. Also, the FSR values in the θ=45° to θ=75° range are comparatively higher than the others. More detailed calculations in this range are shown in figure 3.5(b). The highest value of the FSR could be obtained at θ=55°. Also, the optical axis position with θ=55° helps us to get the lowest FSR (the concluding paragraph of Section 3.1 provided an explanation of why we are seeking the smallest FSR) in the high rotation angle values (>50º). It is also noticeable from figure 3.5(b) that the highest variation in the FSR values occurs when the plate rotation angle (α) values are low. More specifically, when the values of α are lower than 50°, the FSR varies very rapidly with the change in the plate rotation angle values.

Before making the final decision, the impact of the BRF optical axis on the modulation depth (MD) of the BRF also needs to be considered. The calculated results for the MD for various positions of the optical axis are shown in figure 3.6. The modulation depth calculated based on equation 3.3 is a normalized presentation of the MD. MD=1 represents high rejection (nearly 100%) for the adjacent wavelengths of the laser line and MD = 0.1 means 10% rejection. To suppress the adjacent wavelength of the oscillating laser line, we want to have high modulation depth for the BRF.

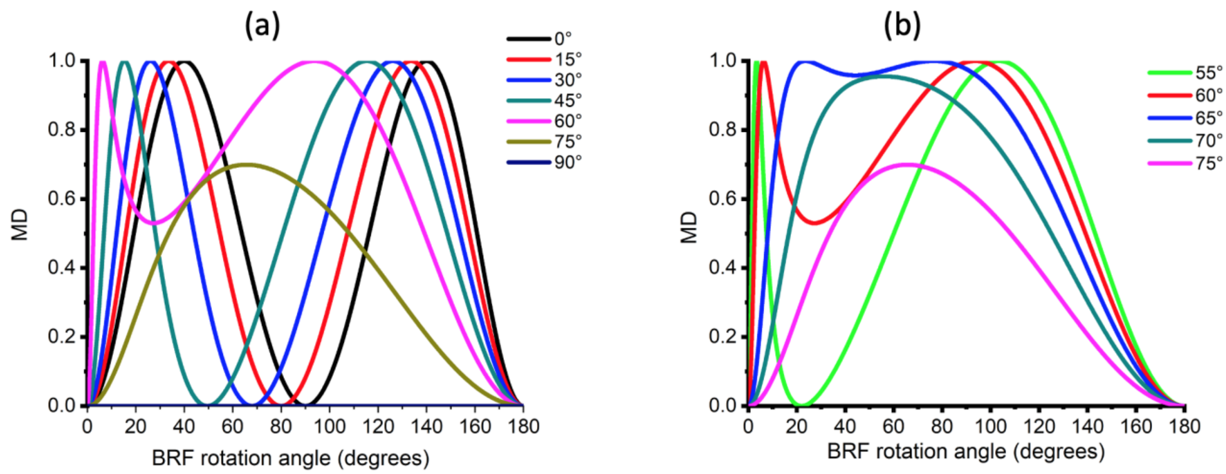

Figure 3.6: Variation of modulation depth with the plate rotation angle with different values of the optical axis off-surface angle values. (a) Off-surface angles θ in the 0° to 90° and (b) in the 55° to 75° ranges.

From figure 3.6(a) it is clear that the modulation depth has the highest values over a large range of rotation angles at the off-surface angle of about θ=60°. The change in the MD values is fairly smooth for this off-surface angle. The variation of MD for other θ values, however, is quite rapid. Since in the previous paragraph the discussion was focused on the θ=55° to 75° range for broadband operation, therefore the variation in the modulation depth values within this range which are presented in figure 3.6(b). When considering the modulation depth perspective to choose the optical axis diving angle, one needs to keep in mind that most of our operation will be at higher rotation angle values as the obtainable FSR is limited by the bandwidth of the laser crystal. For Yb:CALGO this bandwidth is 50 nm which corresponds to angles higher than 80° (Fig 3.5(b)).

Considering the same rotation angle range for modulation depth, it can be seen that the θ=55° covers it with higher MD. Moreover, this higher rotation angle regime gives our targeted wavelength separation (~5nm) as discussed in the FSR section. Considering these facts (i.e. obtaining the narrowest wavelength separation with the highest modulation depth), the optical axis position with θ=55° with respect to filter surface is undoubtedly the best choice. This value of the off-surface optic axis angle will be used in our further analysis.

3.3 Results and discussion for 12 mm off-surface axis BRF

The off-surface axis BRF gives variation in FSR and modulation depth bandwidth when compared to the conventional one. This eliminates the necessity of using several BRFs with different thicknesses to get different wavelength separations [3.17,3.18]. Manjooran et al. [3.13] reported the minimum wavelength separation of 16.7 nm with 6 mm thick conventional BRF. Since the FSR is inversely proportional to the filter thickness [3.24], to obtain an even lower wavelength separation than this, a 12 mm thick BRF was used in this part of the experiment. At an angle of 55° with respect to the filter surface it is possible to obtain fairly low FSR with high modulation depth at the same time. This scenario is presented in figure 3.7. The emission bandwidth of Yb:CALGO crystal is approximately 50 nm, that is, our operation will be mainly in the area of higher BRF rotation angle where modulation depth is strong enough to suppress lasing for the intended lasing line's neighbouring wavelength and a low FSR can be obtained. Therefore, in our experiment, a 12 mm thick BRF with an optical axis lying at 55º with respect to the filter surface was chosen initially.

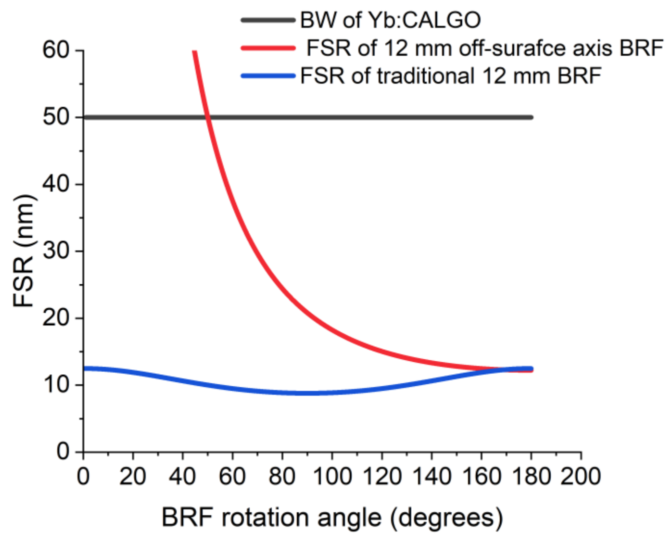

Figure 3.7: Comparison of the traditional BRF and our selected off-surface axis BRF with 12 mm thickness. BW - Bandwidth.

The laser crystal and the pump characteristics were the same as in Chapter 2. The pump beam was imaged into the laser crystal by using two lenses having focal lengths of 50 mm and 75 mm. The resultant pump spot diameter inside the crystal was approximately 157 µm. For DW operation, the off-surface axis BRF was placed close to the HR mirror at Brewster's angle as shown in figure 3.8(a). The spectrum was recorded using a spectrometer (Anritsu MS2687B) with 0.07 nm resolution.

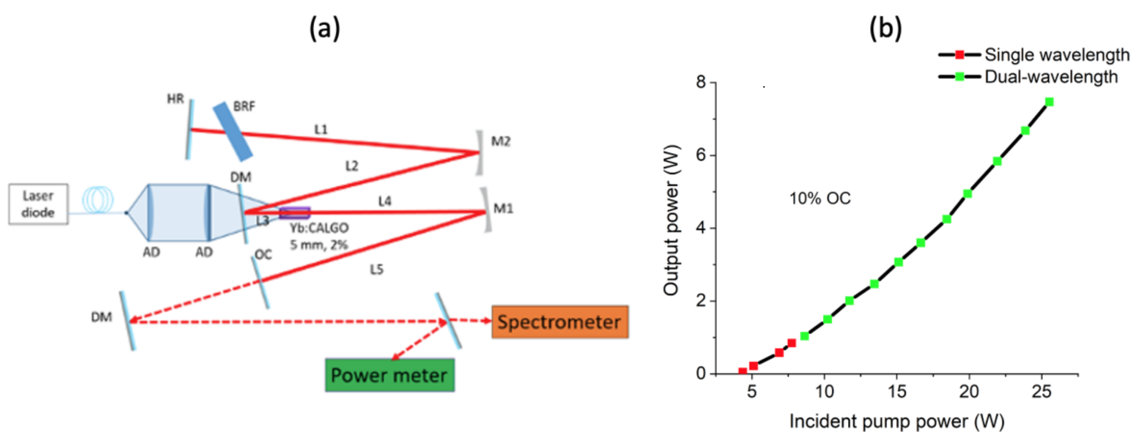

Figure 3.8: (a) Schematic of the laser cavity, (b) output power vs incident pump power for 10% output coupler.

Different output couplers were used but a 10% output coupler gave the best performance in terms of output power. The highest output power was 7.47 W for 25 W of incident power. Initially, the laser was operating in a single wavelength regime. Up to about 8 W of incident pump power, it produced single wavelength radiation. When the incident power was increased above 8 W, the laser switched from a single wavelength regime to a DW regime. Power measurement in the DW regime (figure 3.8 (b)) was done for a DW pair with approximately 10 nm of spacing.

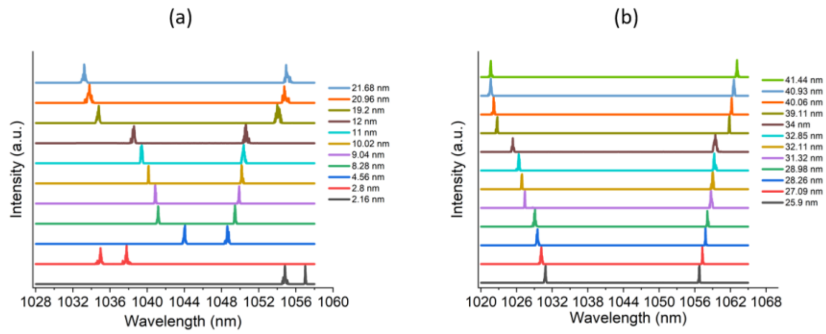

Figure 3.9: DW output with ~1 nm wavelength spacing increment for the (a) 2 - 21.68 nm and (b) 25.9 - 41.44 nm ranges.

As the BRF was rotated, the wavelength spacing between the generated DW pairs was also changed. The observed wavelength spacing from 2.16 nm to 41.44 nm with almost 1 nm increment as shown in figure 3.9. The tuning was so smooth in some wavelength regions that it was possible to tune the wavelength spacing with 0.1 nm increment as shown in figure 3.10. The linewidths of the individual oscillating wavelengths were also varying from 0.1 nm to 0.16 nm as the wavelength spacing ($\Delta\lambda$) varied from 8 nm to 41.44 nm. The spectral power ratio of the two generated wavelengths was not fixed. It was found that the spectral power ratio was changed from 33% to 45% as the wavelength spacing varied from 8 nm to 41.44 nm.

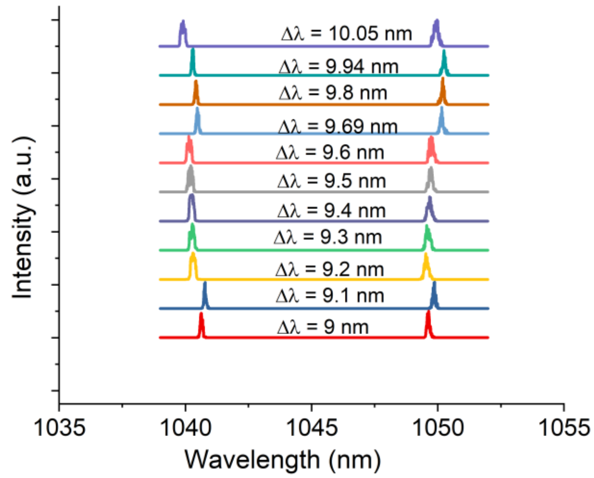

Figure 3.10: DW output with ~0.1 nm wavelength spacing increment.

For a 10% output coupler, a decrease in output power was noticed as the spacing between the generated wavelengths was increased (see figure 3.11(a)). The explanation for this power change is that for shorter wavelength separation the oscillating wavelengths are located close to the maximum of the gain curve. As the wavelength separation increases, the wavelengths shift towards the edges of the gain curve where the gain is lower. As a result, a decrease in output power is observed. Also, from figure 3.11(b), it can be seen that the wavelength spacing change is quasi-continuous. There are some ranges where there were no DW pairs, for example, with wavelength spacing from 35 to 38 nm. These missing pairs, however, can be found by using a different output coupler (e.g. 5%) as the gain spectrum shape changes with different output couplers as shown in figure 2.4.

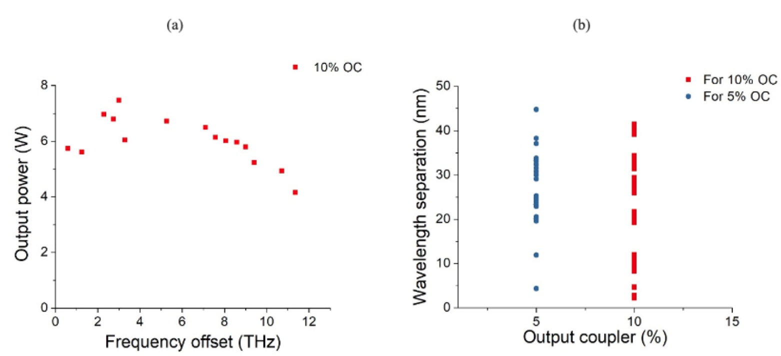

Figure 3.11: (a) Variation in output power for different wavelength spacing and (b) obtained wavelength spacing for 5% and 10% output couplers.

The output beam quality was excellent and is shown in figure 3.12. The measured the beam quality factors as M_x= 1.04 and M_y= 1.03.

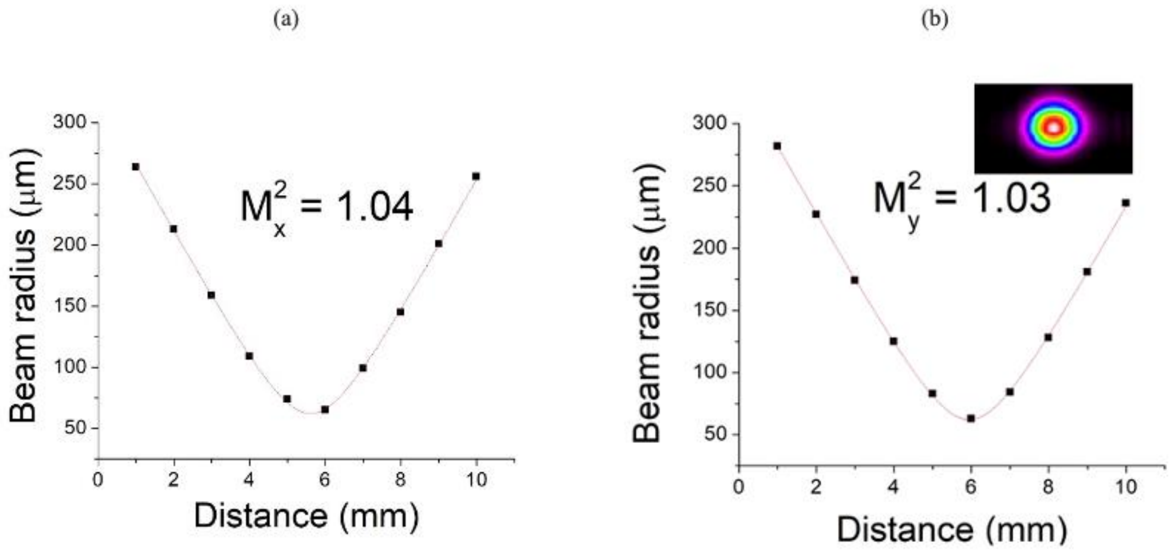

Figure 3.12: Output beam quality factor for 10% output coupler. Inset: transverse beam intensity profile.

From figure 3.7, it can be seen that the maximum possible FSR was limited to ~50 nm by the gain bandwidth and the minimum possible value was around 10 nm (limited by the BRF thickness). In addition to that, the possible FWHM values of the transmission peaks for this 12 mm-thick off-surface axis BRF were in the 0.6-2.5 nm range. At the same time, few DW pairs with wavelength separation smaller than the minimum FSR values, for example 2.16 nm, 2.28 nm, 2.8 nm, 4.74, etc. (see figure 3.13) were recorded. It can be seen that, these smaller values DW pairs were between the DW pairs with larger wavelength separation. For example, a 2.8 nm DW pair was obtained while switching between 41.23 nm and 41.44 nm DW pairs. Wavelength separation smaller than the FSR was also observed in some previous experiments [3.13, 3.26-3.27]. The generation of such a small wavelength spacing that is comparable to the FWHM value of the transmission peak was supported by another loss mechanism of the BRF named as differential loss [3.27]. In these cases, the oscillation of the lower gain wavelength (1044 nm) was supported by the high transmission window of the filter and the oscillation of the 1048.74 nm wavelength was supported by the high gain of the laser although it is in the high loss window of the filter. Such a case is presented in figure 3.13 where the spectrum of the obtained DW radiation is plotted together with the transmission peak of the filter and the gain spectrum of the Yb:CALGO crystal.

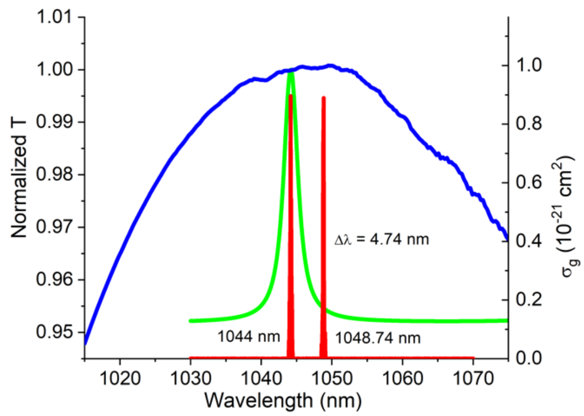

Figure 3.13: DW pair (with 4.74 nm separation) generated by a differential BRF loss mechanism.

In this section, the wavelength spacing tunability of a DW Yb:CALGO laser by using a single optimized off-surface axis birefringent filter has been demonstrated. The results are very encouraging. It was possible to tune the wavelength spacing from 2.16 nm to 41.44 nm with a 1 nm spacing increment offset. In some ranges, the wavelength spacing could be tuned with 0.1 nm increment. The maximum output power was 7.47 W for 25 W of incident power. The beam quality factor of the laser was close to 1. DW pairs with wavelength separation smaller than the FSR of our 12 mm-thick off-surface axis BRF were also observed. This was explained by a new loss mechanism of the BRF. As this part of the experiment went well, in the next part of the experiment, a 24 mm off-surface axis BRF was used. The details of the experiment and results would be discussed in the next section of this chapter.

3.4 Results and discussion for 24 mm off surface axis BRF

The results of the 12 mm thick off-surface BRF plate encouraged us to go for a thicker BRF plate to bring down the wavelength separation even lower than what was obtained. In the second phase of this experiment was done with a 24 mm BRF plate which had similar properties as 12 mm BRF except for the thickness. Since the wavelength separation between the two transmission peaks is inversely proportional to the filter thickness [3.24], by using the 24 mm BRF we can expect to obtain a dual-wavelength output with wavelength separation of around 5 nm which is shown in figure 3.14.

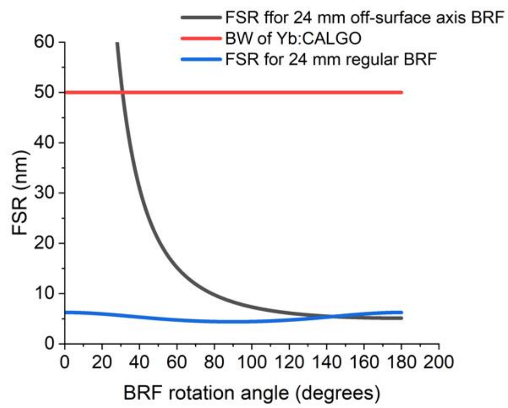

Figure 3.14: Free spectral range of a 24 mm BRF for optical axis is at 55˚ with respect to filter surface (black line), optical axis is on the filter surface (red line), and bandwidth of Yb:CALGO (blue line), BW - Bandwidth.

For this part of the experiment, the experimental setup, laser crystal and pump characteristics were same as for the 12 mm BRF experiment. After optimizing the CW laser, the 24 mm BRF was inserted at Brewster's angle close to the HR mirror as shown in figure 3.8(a). The maximum power from the DW laser was 8.04 W at 25 W incident pump power is shown in figure 3.15. The slight reduction of output power could be due to the very thick BRF which might cause some losses and maybe a slightly off position from the exact Brewster's angle position. Initially, the laser was working in the single wavelength regime. By increasing the incident pump power, it switched to a DW regime which is similar to what was reported in Ref. 3.13. The output beam was recorded using a beam profiler and the beam quality was also measured which was M^2=1.

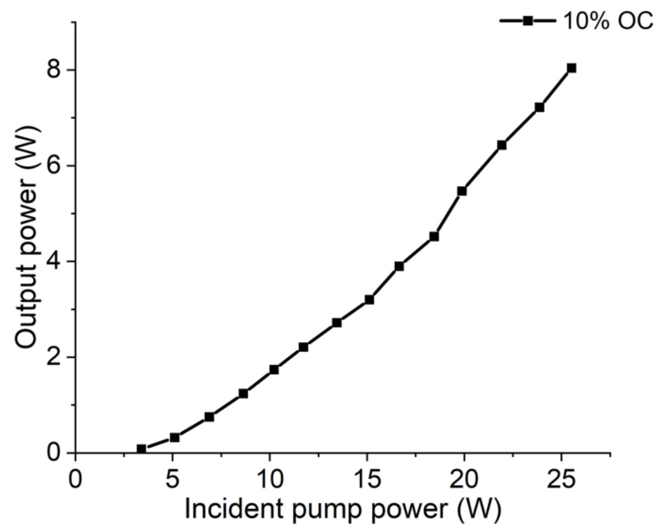

Figure 3.15: Output power for different incident pump power with 10% OC.

To confirm that two wavelengths were simultaneously present in the laser output, a nonlinear crystal BBO was placed at the laser output to generate the second harmonic frequency components and sum-frequency components. The wavelengths at 519.5 nm and 525.19 nm are the second harmonics of 1039 nm and 1050.38 nm (figure 3.16). The sum frequency component at 522.34 nm indicates that two wavelengths were present at the laser output simultaneously [3.28].

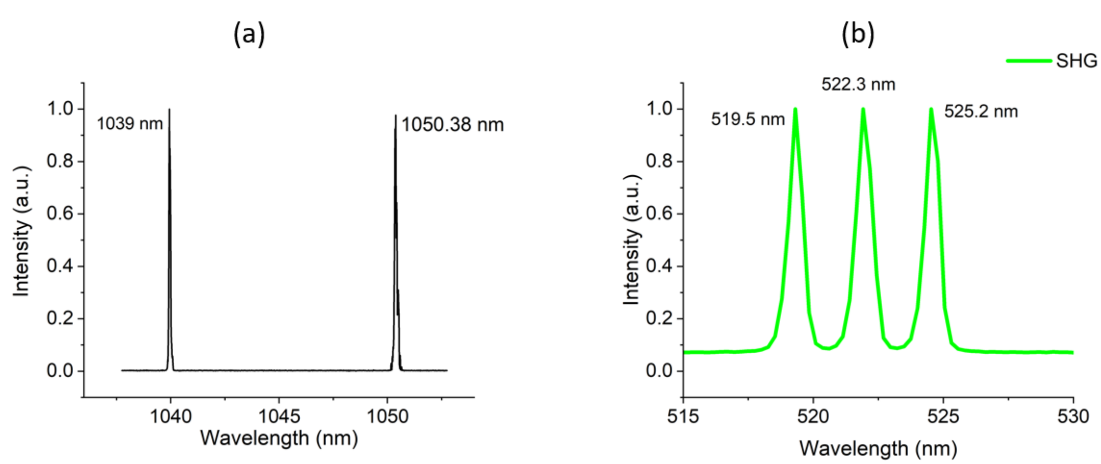

Figure 3.16: (a) Dual-wavelength output from Yb:CALGO laser and (b) second and sum frequency components from the BBO crystal.

To get dual-wavelength with different separation, the BRF plate was rotated, and the dual-wavelength spectrum was recorded using a spectrometer with 0.07 nm resolution. Using the 24 mm off-surface axis BRF, dual-wavelength pairs with separation from 4.11 nm to 24.9 nm were obtained. Although, more than 200 dual-wavelength pairs were observed for 360˚ rotation of the BRF, since the rotation angles from 0˚-180˚ and 181˚- 360˚ range of the filter are identical and the spectrometer resolution is limited to only 0.07 nm, it can be said that there were 98 unique dual-wavelength pairs recorded. The wavelength tuning was smooth and quasi-continuous. The dual-wavelength output can be tuned with 1 nm spacing almost in the whole range as shown in figure 3.17(a). In some cases, it was possible to tune the wavelength separation with 0.1 nm spacing in a small wavelength range (5-6 nm) which is shown in fig. 3.17(b).

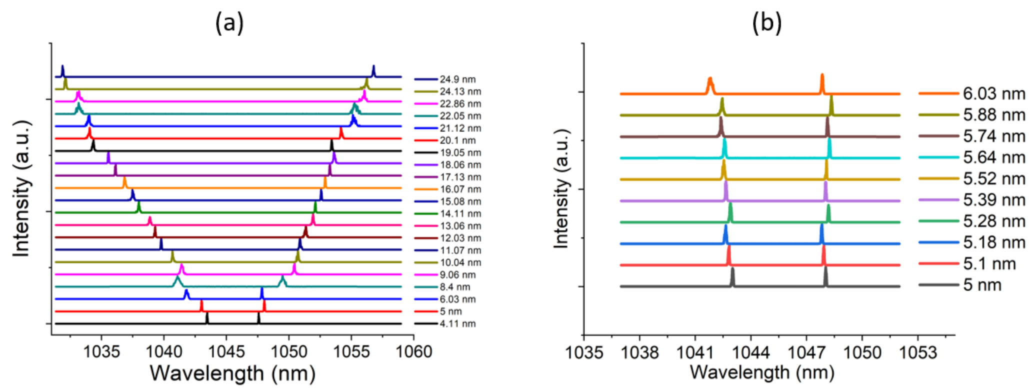

Figure 3.17: (a) DW output with 1 nm spacing and (b) DW output with 0.1 nm spacing increments.

The spectral intensity of the output wavelength was adjusted to a 1:1 ratio by slightly adjusting the BRF plate. The amplitude of the spectral intensity was also sensitive to the pump power. A change in the pump power may change the 1:1 ratio. However, a 1:1 ratio can be brought back by a little adjustment of the BRF plate. The fluctuations in the spectral intensity vary with the wavelength separation of the generated wavelengths. A variation of 42%-50% was found in the spectral intensity while the wavelength separation changed from 4.11 nm to 24. 9 nm. The linewidth of the oscillating wavelengths was found to vary from 0.08 nm to 0.13 nm.

The maximum output power was 8.04 W at 25 W incident pump power for a 10% output coupler. The optical-to-optical efficiency was 32.16% for the maximum incident pump power (41.85% optical-to-optical efficiency for absorbed pump power under non-lasing condition) and the slope efficiency with respect to the incident pump power was 36.65% (49.37% slope efficiency with respect to the absorbed pump power under non-lasing condition). This scenario is shown in figure 3.18(a). Also, in figure 3.18(b), all the wavelength separations that were plotted were obtained by using a 10% output coupler. From the graph, it can be seen that the wavelength separation tuning is almost continuous from 4.11 nm to 24.9 nm except for a little range (6.6 nm-8.4 nm). The reason for this small gap could be explained in terms of the gain-bandwidth curve of the gain medium under which equal gain for two different laser modes was not obtained. As discussed in the result section 3.3 for the experiment with 12 mm BRF, the missing pairs can be found by using different output couplers.

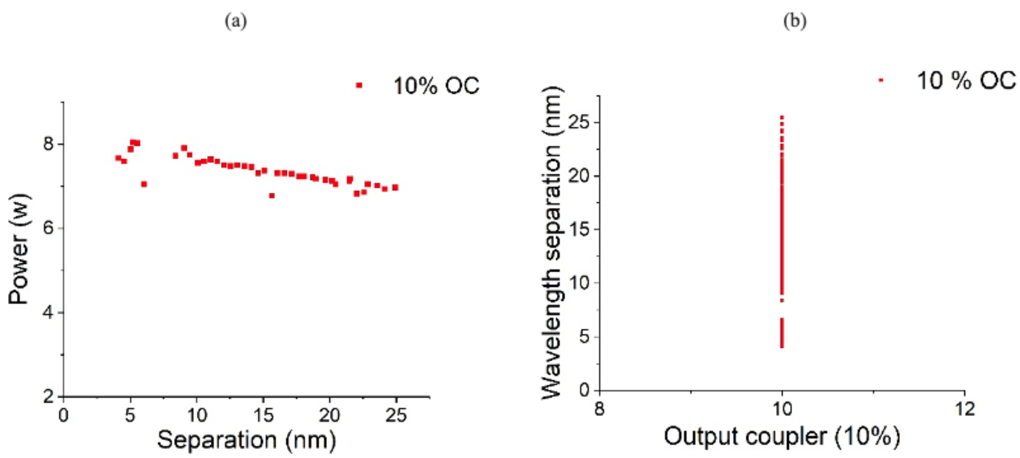

Figure 3.18: (a) Variation in output power with wavelength separation. (b) Obtained wavelength spacings for 10% output coupler.

In this section, the tunability of a Yb:CALGO laser with a 24 mm optimized off-surface axis birefringent filter has been demonstrated. It was shown that the dual-wavelength output can be tuned from 4.11 nm to 24.9 nm almost quasi-continuously with 1 nm spacing for almost the entire range. In small ranges, it could be tuned with 0.1 nm spacing or even smaller. The step size was limited by the resolution of our spectrometer which was 0.07 nm in this case. To the best of our knowledge, this is the smoothest dual-wavelength tuning for any off-surface axis BRF. The maximum output power was 8.04 W at 25 W incident pump power. Approximately 98 unique DW pairs were observed at the output of the laser which is the highest number of DW pairs from any DW laser equipped with an off-surface axis BRF. The previous reports for off-surface axis BRF stated 10 and 11 DW pairs for Cr:Nd:GSGG and Cr:LiSAF crystals in Ref.3.15 using a 3 mm BRF. In Ref. 3.22, 12 DW pairs were reported for Tm:LuAG laser using an optimized 3 mm BRF which was the highest number of DW pairs coming out from any laser using one BRF with a particular thickness. Observing 98 DW pairs in this experiment is clearly a record number compared to the former experiments. Also, 8.04 W of output power with 41.85% optical-to-optical efficiency (with respect to the absorbed pump power under non-lasing condition) proves that our laser worked efficiently. It can be compared to the previous DW operation of Yb:CALGO laser with 27.52% optical to optical efficiency (with respect to the absorbed pump power under non-lasing condition) with 6 mm thick conventional BRF [3.13]. For off-surface axis experiments, the highest reported output power was 738 mW with 16.2% optical-to-optical efficiency (with respect to the absorbed pump power). Using a thick (24 mm) BRF, it was possible to get dual-wavelength separation of less than 10 nm that can be tuned with 0.5 nm wavelength spacing which could be ideal for specific astronomical applications [3.1, 3.3]. Based on the above results and discussion, it can be concluded that off-surface axis BRF could be a great choice for low-cost, high power tunable dual-wavelength experiments.

3.5 Conclusion

In this chapter, the design procedure of an off-surface axis birefringent filter has been discussed. It was shown that by using this off-surface axis BRF, tune the dual-wavelength output can be tuned without the need to use a BRF with a different thickness which was the case for conventional design. It was also shown that a BRF with optical axis making an angle of 55 degrees with respect to filter surface can yield the best filtering performance. To get the lowest possible wavelength separation, a 12 mm and a 24 mm off-surface axis BRFs were used. With the 12 mm BRF, it was possible to tune the wavelength separation from 2.16 nm to 41.44 nm with approximately 1 nm step size and the highest output power was 7.47 W at 25 W of incident pump power. Although this tuning was not smooth for the whole range, in some smaller ranges it was possible to tune the DW output with a 0.1 nm step size. By using the 24 mm BRF, it was possible to tune the dual-wavelength pair with wavelength separation from 4.11 nm to 24.9 nm with approximately 1 nm step size. The highest obtained output power was 8.04 W at 25 W of incident pump power.

Hopefully, this result will be interesting for some biomedical, communication and astronomical applications [3.1-3.6].

REFERENCES

[3.1] P.H. Siegel, "Terahertz technology," IEEE Trans. Microw. Theory Technol. 50(3), 910–928 (2002).

[3.2] P. Gu, F. Chang, M. Tani, K. Sakai, and C. Pan, "Generation of Coherent cw-Terahertz Radiation Using a Tunable Dual-Wavelength External Cavity Laser Diode," Jpn. J. Appl. Phys. 38, L1246–L1248 (1999).

[3.3] M. Scheller, J. M. Yarborough, J.V. Moloney, M. Fallahi, M. Koch, and S. W. Koch, "Room temperature continuous-wave milliwatt terahertz source," Opt. Express 18(26), 27112-27117 (2010).

[3.4] S. Chang, Y. Mao, C. Flueraru, "Dual-source swept-source optical coherence tomography reconstructed on integrated spectrum," Int. J. Opt. 2012, 565823 (2012).

[3.5] C. Debus, and P. H. Bolivar, "Frequency selective surfaces for high sensitivity terahertz sensing," Appl. Phys. Lett. 91(18), 184102 (2007).

[3.6] T. Yasui, T. Yasuda, K. Sawanaka, and T. Araki, "Terahertz paint meter for noncontact monitoring of thickness and drying progress in paint film," Appl. Opt. 44(32), 6849–6856 (2005).

[3.7] R. Czarny, M. Alouini, C. Larat, M. Krakowski, D. Dolfi, "Continuous-wave THz generation through photomixing using a dual-frequency Yb^{3+}: $KGd(WO_4)_2$ laser," Electron. Lett. 40, 942–943 (2004).

[3.8] A. Brenier, "Tuanble THz frequency difference from a diode-pumped dual-wavelength Yb^{3+}: $KGd(WO_4)_2$ laser with chirped volume Bragg gratings ," Laser Phys. Lett. 8, 520–524 (2011).

[3.9] Y. Ji, J. Cao, J. Xu, Z. You, C. Tu, "2.4 W highly efficient simultaneous dual-wavelength laser operation of monoclinic Yb^{3+}: $Ca_4LaO(BO_3)_3$ crystals," Appl. Opt. 53, 5517–5521 (2014).

[3.10] A. Brenier, "Active Q-switching of the diode-pumped two-frequency Yb^{3+}:$KGd(WO_4)_2$ laser," Quantum Electron. 47, 279–284(2011).

[3.11] H. Zhao, A. Major, "Orthogonally polarized dual-wavelength Yb:KGW laser induced by thermal lensing," Appl. Phy. B 122(6), 163-169 (2016).

[3.12] P. Loiko, S. Manjooran, K. Yumashev, and A. Major, “Polarization anisotropy of thermal lens in Yb:KY$(WO_4)_2$ laser crystal under high-power diode pumping,” Appl. Opt. 56(10), 2937–294 (2017).

[3.13] S. Manjooran, P. Loiko, A. Major, “A discretely tunable dual-wavelength multi-watt Yb:CALGO laser,” Appl. Phys. B 124(1), 13 (2018).

[3.14] R. Akbari, H. Zhao, and A. Major, “High-power continuous-wave dual-wavelength operation of a diode-pumped Yb:KGW laser,” Opt. Lett. 41(7), 1601-1604 (2016).

[3.15] S. Ghanbari and A. Major, "High power continuous-wave dual-wavelength alexandrite laser," Laser Phys. Lett. 14(10), 105001 (2017).

[3.16] K. Naganuma, G., Lenz, and E.P. Ippen, “Variable bandwidth birefringent filter for tunable femtosecond lasers,” IEEE J. Quantum Electron. 28(10), 2142-2150 (1992).

[3.17] U. Demirbas, R. Uecker, J.G. Fujimoto, and A. Leitenstorfer, “Multicolor lasers using birefringent filters: experimental demonstration with Cr:Nd:GSGG and Cr:LiSAF,” Opt. Express 25(3), 2594-2607 (2017).

[3.18] U. Demirbas, “Off-surface optic axis birefringent filters for smooth tuning of broadband lasers,” Appl. Opt. 56(28), 7815-7825 (2017).

[3.19] S. M. Kobtsev and N. A. Sventsitskaya, “Application of birefringent filters in continuous-wave tunable lasers: a review,” Opt. Spectrosc. 73(1), 114-123 (1992)

[3.20] U. Demirbas, J. Wang, G. S. Petrich, S. Nabanja, J.R. Birge, L.A. Kolodziejski, F.X. Kartner, and J.G. Fujimoto, “100-nm tunable femtosecond Cr:LiSAF laser mode locked with a broadband saturable Bragg reflector,” Appl. Opt. 56(13), 3812-3816 (2017)

[3.21] Md. A. R. Reza, C. Dyck, S. Manjooran, P. Loiko, A. Major, “Optimized birefringent filter design for multi-wavelength operation of Yb-ion lasers,” Proc. SPIE 10513, 105131L (2018).

[3.22] T. Waritanant, A. Major, “Thermal lensing in Nd:YVO_4 laser with in-band pumping at 914 nm,” Appl. Phys. B 122(5), 135 (2016).

[3.23] T. Waritanant, A. Major, "Diode-pumped Nd:YVO_4 laser with discrete multi-wavelength tunability and high efficiency," Opt. Lett. 42, 1149-1152 (2017).

[3.24] S. Zhu, “Birefringent filter with tilted optic axis for tuning dye lasers: theory and design,” Appl. Opt. 29(3), 410-415 (1990).

[3.25] S. Lovold, P.F. Moulton, D.K. Killinger, and N., Menyuk, “Frequency Tuning Characteristics of a Q-switched Co:MgF2 laser,” IEEE J. Quantum Electron. 21(3), 202-207 (1985).

[3.26] E. Beyatli and U. Demirbas, “Widely-tunable dual-wavelength operation of Tm:YLF, Tm:LuAG and Tm:YAG lasers using off-surface optic axis birefringent filters,” Appl. Opt. 57, 6679 (2018).

[3.27] R. Akbari, P. Loiko, J. Xu, X. Xu, and A. Major "Dual-wavelength Nd:CALGO laser based on an intracavity birefringent filter", Proc. SPIE 10896, 1089611 (2019).

[3.28] R. Akbari and A. Major, “Dual-wavelength Nd: YVO4 laser with two-crystals geometry”, Proc. SPIE Vol. 11664, 116641B (2021).

Chapter 4

High power conical refraction (CR) output from a continuous-wave Yb:CALGO laser and its dual-wavelength operation

A biaxial crystal cut along its optical axis transforms a Gaussian beam into a pair of bright concentric rings separated by a dark Poggendorff ring and the output beam has an annular intensity distribution. In this chapter, the discussion will be focused on the generation of conical refraction (CR) output from CW Yb:CALGO laser and its wavelength tuning by using a BRF. Finally, the results of dual-wavelength operation of this laser based on a conventional and off-surface axis BRFs will be discussed.

4.1 Introduction

A beam with Gaussian intensity distribution travelling along the one of the optical axes of a biaxial crystal refracts conically and transforms into a bright pair of concentric rings. The bright rings are separated by a dark Poggendorff ring (figure 1(a)). There is a plane called the Llyod image plane where the brightest conical refraction (CR) beam with the Poggendorff dark ring can be observed clearly. Moving away from this plane along the beam propagation direction, one can observe that the bright CR rings become thicker (figure 1(b)). As one moves further away from the image plane, the CR rings become a dot which is known as the Raman spot (figure 1(c)). Another signature characteristic of the CR beam is that the polarization of the two diametrically opposite points is orthogonal to each other [4.1-4.5]. This polarization property is useful for polarization multiplexing in optical communication to send and receive information. It can be also used in polarization metrology where the polarization detection of a light beam is extremely important to determine various properties such as absorption coefficient, index of refraction etc. The bright concentric light rings of the CR beam can be used in super-resolution microscopy to confine fluorescence emission to a small area of the sample under study [4.2].

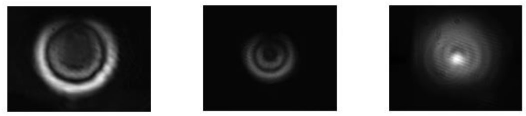

Figure 4.1: Schematic of (a) CR beam with two bright concentric rings separated by dark Poggendorff ring, (a) to (c) is representing the transformation of a CR beam into a Raman spot.

The theoretical knowledge of the CR laser beam formation and its characteristics have been explained in some previous works and traditionally the laser gain medium was also employed as the CR laser medium [4.6-4.16]. Using the laser gain medium as the CR element makes it difficult to understand some phenomena such as the beam transformation from the Gaussian intensity profile to the CR beam inside the cavity, the transformation of the double ring CR beam into a "Raman spot" at far-field after the cavity. Recently, a new model has been proposed and showed some prominent results by keeping the CR element (CRE) separated from the laser gain medium. Keeping the CRE separate from a laser gain medium makes it easier to use a laser crystal of our choice as the properties are now not limited by the CRE element which makes the power scaling incredibly easy. Also, adjustment of the laser crystal and CRE becomes easier as they are separated. Another main advantage is that the CR properties are not dependent on laser properties. In Ref. 4.17, the available pump power was 500 mW and it was possible to produce high quality CR beams with 220 mW of output power. However, due to the lack of the high pump power source for that experiment, it was not clear what would happen under high pump power. That is the reason to investigate CR laser operation in the high-power regime. In this chapter, a laser with a CR output beam will be called as a "CR laser".

In this experiment, the generation of multi-watt power scalable CR laser based on Yb:CALGO with a separate intracavity CRE with very good quality of CR beams has been demonstrated. The output power was 6.25 W at 25 W of incident pump power. In addition, the beam evolution after the output coupler was also investigated. By using a 1 mm-thick traditional birefringent filter, the tuning operation of the CR laser was observed. After successful tuning operation, the dual-wavelength output from this laser by using a 6 mm-thick conventional BRF will be presented.

Then the dual-wavelength tuning operation of this laser by using a 24 mm-thick optimized birefringent filter will be discussed.

4.2 Experimental setup

Light from the laser diode was imaged into the crystal by using two lenses of 50 mm and 75 mm focal length. The resulted pump beam radius inside the crystal was about 79 µm whereas the laser mode radius was about 75 µm. The schematic of the laser cavity is shown in figure 4.2. The cavity design was done by considering the thermal lensing effect and for better mode matching the cavity mode was kept very close to the pump mode. The maximum pump power absorbed under non-lasing conditions was 13.22 W at an incident pump power of 25 W. The output power from the laser was measured by a power meter and the spectrum was monitored by a spectrum analyzer having a resolution of 0.07 nm (Anritsu MS2687B). The mirror M3 provided a suitable focusing of the laser mode into the CR element (CRE). A 18 mm long biaxial KGW ($KGd(WO_4)_2$) crystal cut along its optical axis was used as an intracavity CRE. The KGW crystal is a typical choice as a CRE because of its anisotropic optical and physical parameters. It is also a good host for rare-earth ion based-lasers [4.12-4.16].

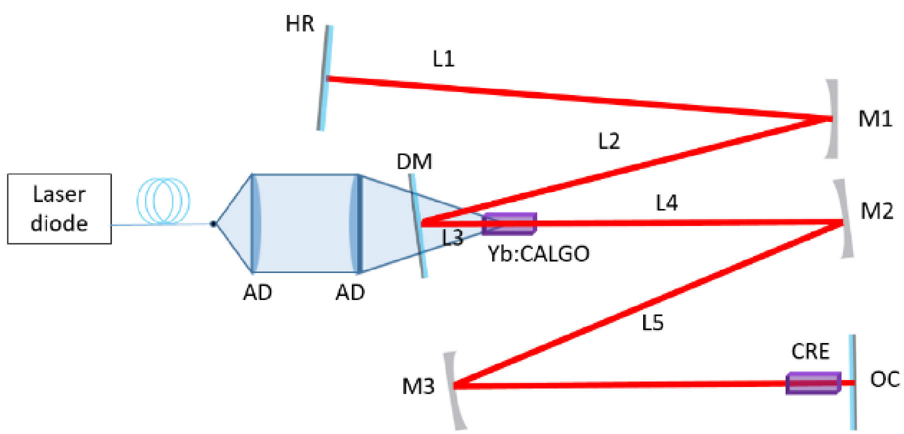

Figure 4.2: Schematic of the laser cavity. M1 = -300 mm, M2 = −250 mm, M3 = −150 mm. OC: output coupler, HR: highly reflective mirror. CRE: conerefringent element.

4.3 Results and discussion

Initially, the performance of the laser was optimized in the CW regime. With a 10% output coupler (OC), 7.5 W of output power was achieved at 25 W of incident pump power. The next step was to observe high power CR laser operation. The CRE was put very close to the output coupler (a few mm away from the surface of the OC). The optical axis of the CRE and the laser mode axis alignment were crucial for good quality CR beam generation. For a large misalignment between these axes, the observed output power was very low. After the alignment, an increase in output power was observed. At that point, a double refraction pattern was also observed at the output of the laser. Further attempts to align the laser mode axis and the optical axis of the CRE resulted in high output power with a nice quality CR beam. Two bright concentric rings which were separated by a dark band known as "Poggendorff dark ring" was observed. The CR laser beam was recorded using a digital camera and for imaging a 60 mm lens was used. This can be seen in figure 4.1(a) for clarity.

In most of the previous experiments, the parameter ρ_0 (the ratio of the radius of the CR beam to the radius of the input beam, detailed description is presented in Appendix B) was highlighted as an important one to obtain a clear CR beam. The suggested value for this ratio is $\rho_0 >> 1$ [4.2, 4.10, 4.17]. In this experiment, ρ_0 was approximately 4 which yielded a nice CR beam which is shown in figure 4.3. To get higher ρ_0, tight focusing of the laser beam into the CRE is helpful. Considering this fact, for tight focusing, a curved mirror with M3 = -150 mm radius of curvature was used. In some of the previous experiments [4.12, 4.15], crescent-shaped CR beam was observed. It was shown that this crescent-shaped CR beam could have happened because of the larger laser mode size in the CRE and thus lower ρ_0 value [4.17].

The maximum output power from the CR laser was 6.25 W at 25 W of incident pump power using a 10% output coupler. In addition to that, some signature characteristics of the CR laser output was explored as well. The Lloyd image plane was 1-3 mm away from the output coupler in this experiment where two bright concentric rings separated by a Poggendorff dark ring was clearly visible as shown in figure 4.3(a). As moved from the image plane, the fine CR rings separated by the Poggendorff dark rings became thicker. Moving further away from the image plane, the beam transformed into a spot-like shape known as Raman spot (figure 4.3(g)). Another very interesting property is the polarization pattern of the CR beam. The polarization state distribution along the

CR beam was determined by using a polarizing beam splitter. The polarization of the diametrically opposite points on the beam is orthogonal to each other. The orthogonal polarization pattern of the diametrically opposite points on the beam is shown in figure 4.3(h).

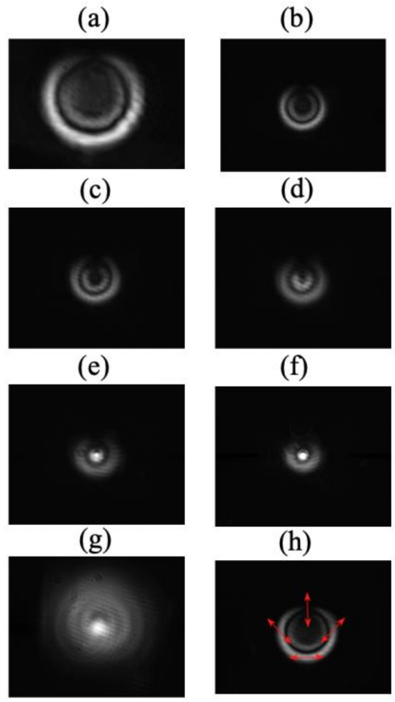

Figure 4.3: The CR laser beam at the Lloyd image plane and its free-space evolution along the beam propagation axis for the horizontal orientation of the N_m-axis of the CRE. Here, z is the measured distance of the corresponding beam position from the front surface of the OC (a) z = 6.7 mm (b) z = 17 mm (c) z = 26.4 mm (d) z = 41.7 mm (e) z = 58 mm (f) z = 73.64 mm((g) is z = 300 mm away from OC which is the far-field view of the beam (h) orthogonal polarization states of the diametrically opposite points on the beam determined by a polarizer.

To compare the performance of the CR laser against an equivalent non-CR laser, the CRE was replaced by a 20 mm-long AR-coated N_g-cut (non-CR) KGW crystal in the cavity. With 10% output coupler, the maximum output power obtained with the non-CR KGW crystal was 7.21 W at 25 W of incident pump power while for CR laser the maximum output power was 6.25 W. The comparison of the performance evaluation is shown in figure 4.4.

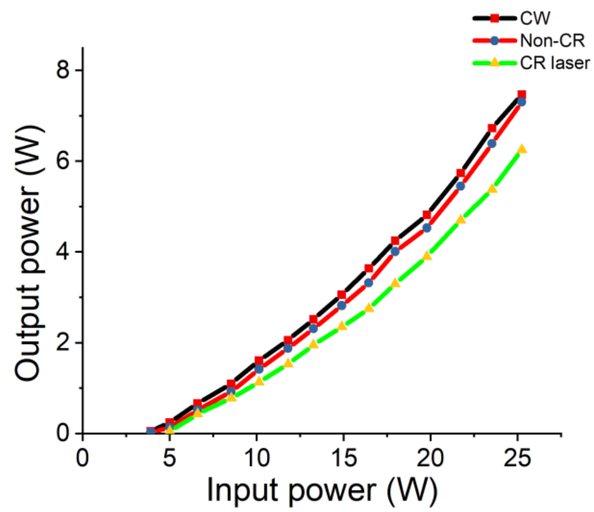

Figure 4.4: The output powers vs. the incident pump power for the CW laser (with and without non-CR crystal) and CR laser.

The wavelength tuning performance of the CR laser of the laser was also explored. For tuning operation, a 1 mm-thick regular birefringent filter was put at Brewster angle close to the HR mirror in figure 4.2. The alignment with the BRF was very critical as the output power and the wavelength were very sensitive to the rotation of the BRF. The CR laser showed the tunability from 1018.95 nm to 1054.80 nm. The tuning operation of the CR laser is shown in figure 4.5.

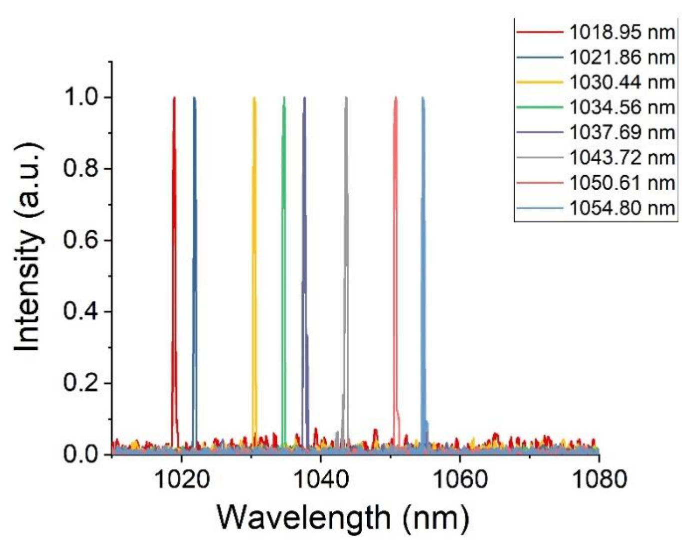

Figure 4.5: Wavelength tuning of the CR laser using 1 mm thick regular BRF.

The CR beam evolution inside the cavity was also explored. With an infrared light detector card, two output beams were observed after the M3 mirror. The recorded beam intensity profiles are shown in the figure 4.6. In this case beam 1 was approaching the CR crystal after a double pass-through the laser crystal while beam 2 was propagating towards the laser crystal after a double pass through the CR crystal. The beam profile after the HR mirror was also recorded.

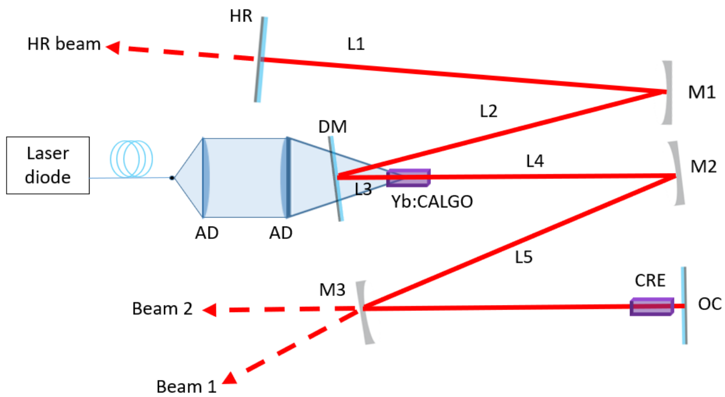

Figure 4.6: Observation points of the evolution of the CR laser modes inside the cavity.

Beam 1(figure 4.7(a)) has Gaussian like intensity distribution while beam 2 (figure 4.7(b)) shows more prominent intensity distribution. On the other hand, figures 4.7(c) and 4.7(d) compare the intensity distribution after the HR mirror with the CR crystal and without the CR crystal in the cavity and it can be clearly seen that the background for the intensity distribution with the CR crystal has some complex pattern compared to the one without the CR crystal.

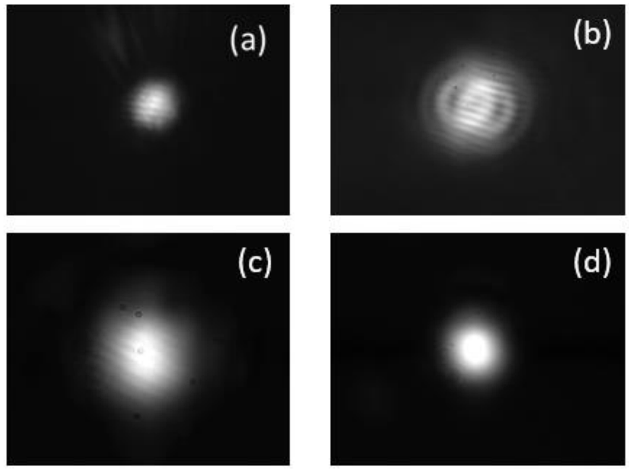

Figure 4.7: (a) Intensity distribution of the laser mode travelling towards CRE after a double-pass through the laser crystal and (b) Intensity distribution of the laser mode going towards the laser crystal after a double-pass through the CRE. (c) Intensity distribution after the HR mirror with the CR crystal in the cavity and (d) Intensity distribution after the HR mirror without the CR crystal in the cavity.

With the observation of the of the change in the intensity profile of the beam as discussed above, the CW part of the experiments was concluded. In conclusion, a high-power conical refraction (CR) laser was demonstrated based on the Yb:CALGO crystal as a laser gain medium and the KGW crystal as a separate intracavity CR element . The recorded output power was 6.25 W at 25 W of incident pump power. Keeping the CRE separated from the laser gain medium not only enabled to get a power scalable system with high output power but also helped to get a high-quality CR beam with clearly visible Poggendorff dark ring which separates the two bright concentric rings. The wavelength tuning capability of the CR laser with a 1 mm conventional BRF was observed and found that it is possible to discreetly tune the CR beam over approximately 40 nm tuning range. The polarization properties of the CR beam were also analyzed and like in the previous experiments it was found that the polarization is orthogonal for diametrically opposite points of the CR beam. This is the first ever demonstration of such a high-quality beam with high output power. As the gain medium was kept separate from the CRE, this reduces the complexity of the set up and enables further power scalability. Observation of the performance of the CR laser in the high-power regime and the success of its wavelength tuning encouraged to explore the dual-wavelength performance of such a laser which is presented in the next section of this chapter.

4.4 Dual-wavelength (DW) output from the CR laser and its tuning operation by using a birefringent filter (BRF)

In chapter 3, it has been discussed that by inserting a birefringent filter, one can equalize the gain for two different laser lines which will produce dual-wavelength output from the laser. As shown in figure 4.4, the CR laser showed successful wavelength tuning operation by using a 1 mm thick BRF. The next goal was to investigate the dual-wavelength output by using a 6 mm-thick regular BRF and then to explore the dual-wavelength tuning operation of the laser by using a 24 mm-thick off-surface axis BRF which was designed and discussed in section 3.2. In previous chapter, it has been discussed that with a regular BRF, the free spectral range (FSR), which is the wavelength separation between the two transmission peaks, is almost constant for a given thickness of the BRF, while with an off-surface axis BRF one can get a wide variation in the FSR [4.18-4.24]. The expected calculated FSR for a conventional 6 mm-thick BRF is 17-25 nm and for the 24 mm-thick off-surface axis BRF it is 5-50 nm. Here the upper range is limited to 50 nm as the bandwidth of CALGO is around 50 nm [4.25]. This scenario is shown in figure 4.8 below:

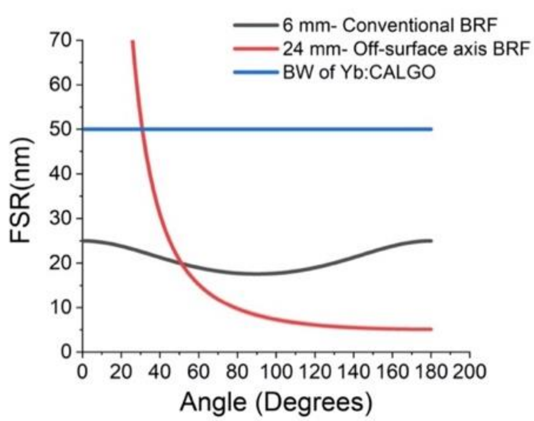

Figure 4.8: The calculated free spectral range for a regular 6 mm BRF and a 24 mm off-surface axis BRF. BW = bandwidth

4.4.1 DW results with 6 mm thick regular BRF

For the dual-wavelength operation, the 6 mm BRF was put at the Brewster angle close to the HR mirror as shown in figure 4.2. The output spectrum was recorded by a spectrometer with 0.07 nm resolution. The remainder of the experiment employed this output coupler since it generated the best results in terms of beam quality and power. With 6 mm BRF the maximum output power was approximately 6 W for 25 W of incident pump power which is shown in figure 8. As the BRF was rotated, a few pairs of DW with wavelength separation between 17-25 nm were observed with excellent beam quality displaying a clear Poggendorff dark ring which is shown as an inset in figure 4.9.

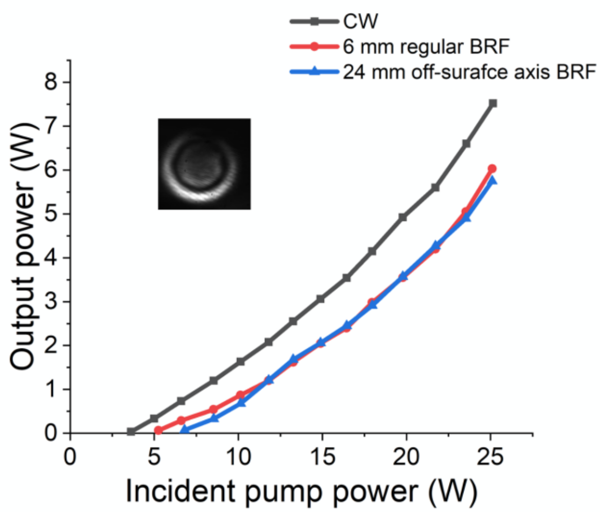

Figure 4.9: Output power comparison of 6 mm and 24 mm BRF cavities with CW regime (without BRF). The inset is the corresponding CR beam profile recorded for 6 mm BRF.

The dual-wavelength pairs obtained by using the 6 mm BRF are shown in figure 4.10(a) below with the corresponding CR beams in figure 4.10(b). In all the cases, the CR beams were clear with distinguishable Poggendorff dark ring which indicates the high beam quality. The CR laser was very sensitive to the BRF rotation. After rotating the BRF, a little adjustment to the CRE was needed to maintain the good beam shape. The BRF was also adjusted slightly to maintain the 1:1 ratios of the spectral intensity. The variation of the spectral intensity was found to be about 40%-

50%. The linewidth of the oscillating wavelengths was found to be in the 0.08 nm - 0.13 nm range which was limited by the resolution (0.07 nm) of the spectrometer.

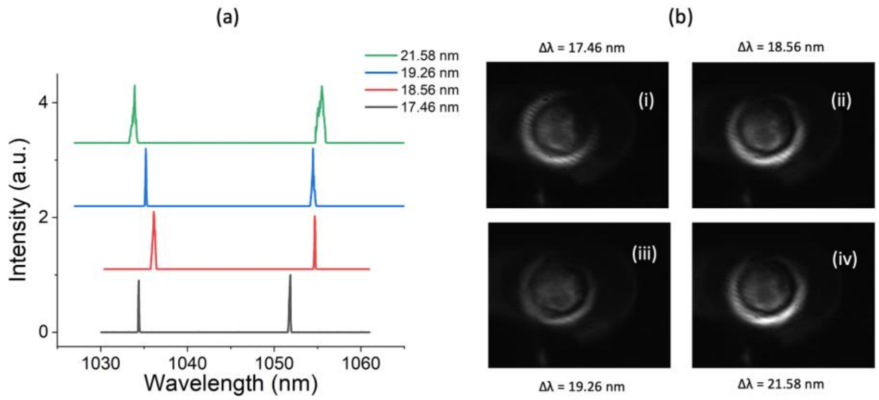

Figure 4.10: (a) Dual-wavelength pairs with a regular 6 mm BRF and (b) the corresponding CR beam photos.

As it can be seen from figure 4.8, the expected wavelength separation is 17-25 nm, but in the experiment, a dual-wavelength pair with 8.82 nm of wavelength separation was observed which is shown in figure 4.11. This figure also displays the transmission peak of the filter and the gain spectrum of the Yb:CALGO crystal. Similar pairs were observed before for the 12 mm BRF DW experiments and explained in section 3.3 via a differential loss mechanism. As the dual-wavelength experiment was successful with conventional 6 mm BRF, the next goal was to tune this dual-wavelength output by using an optimized 24 mm off-surface axis BRF which will be discussed in next section 4.4.2.

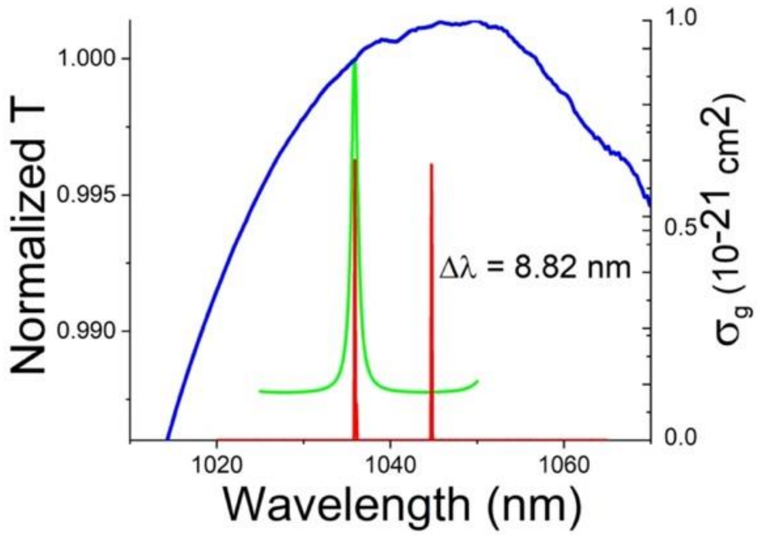

Figure 4.11: Dual-wavelength pair with 8.82 nm generated by the differential loss mechanism.

4.4.2 DW results with 24 mm off-surface axis BRF

The optimized design technique for an off-surface axis BRF was discussed in section 3.3 and the results of the DW output for a CW laser were presented in section 3.4. The expected wavelength separation range for this BRF is 5-50 nm which can be seen in figure 4.7 by replacing the 6 mm BRF in figure 4.2 by the 24 mm BRF. The highest output power was 5.75 W at 25 W of incident pump power with 10% output coupler. The dual-wavelength output with wavelength separation changing from 3.76 nm to 19.76 nm was observed. In figure 4.12(a), dual-wavelength pairs with 1 nm step size from 4.08 nm to 19.76 nm is presented. With the various wavelength separation, the CR beam intensity profile was recorded as well. It can be seen from figure 4.12(b) that beams still maintain good shape. The variation of the spectral intensity of the dual-wavelength output was about 45%-50 % and the linewidth at full width at half maximum (FWHM) was about 0.07 - 0.15 nm.

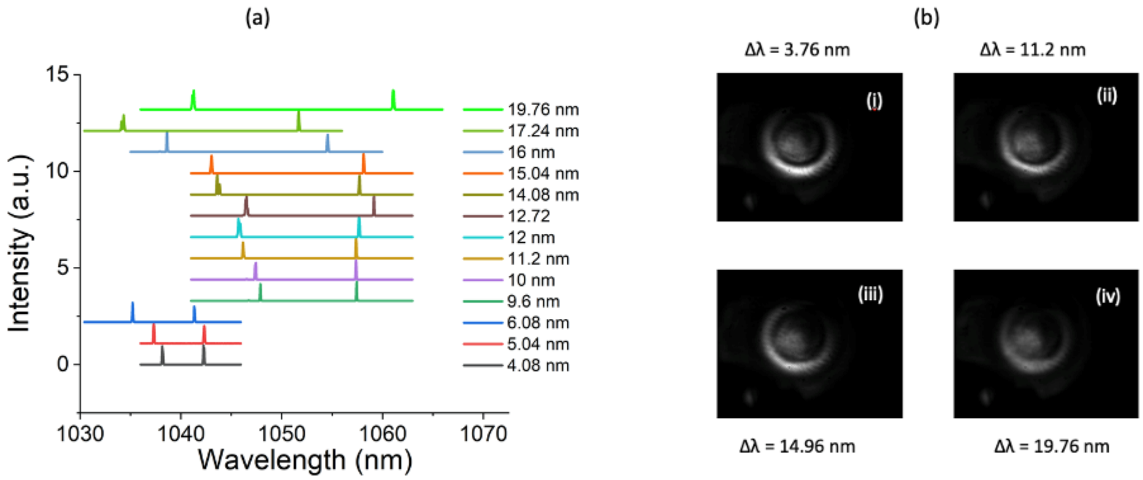

Figure 4.12: (a) Dual-wavelength output pair with 24 mm BRF and (b) examples of the recorded CR beam intensity profiles at different dual-wavelength separation.

The wavelength separation obtained for this 10% output coupler is summarized in figure 4.13 and the corresponding recorded output power is also shown as well. The wavelength separation is not continuous like the results which were presented in sections 3.3 and 3.4. But one can obtain the desired wavelength separation by using a different output coupler which was also explained in section 3.3. Also, similar to the previously described DW experiments, figure 4.13 shows a characteristic decrease in the output power as the separation between the generated wavelengths increased.

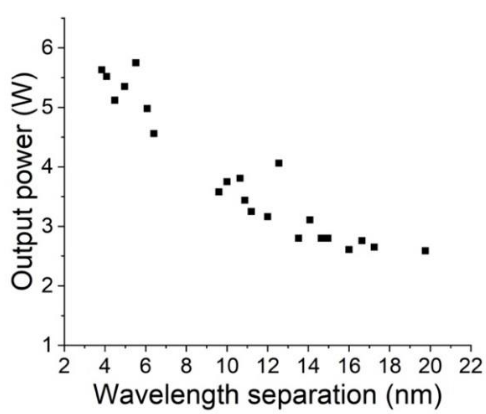

Figure 4.13: The decrease in output power with increase in wavelength separation.

4.5 Conclusion

A high-power CR laser based on Yb:CALGO crystal with KGW crystal as a CRE element has been demonstrated. Keeping the CRE separated from the gain medium, enabled to get the exceptional quality CR beams with 6.25 W of output power at 25 W of incident pump power. The wavelength tuning operation of the CR laser by using a 1 mm BRF was also observed, and it was shown that the output can be tuned over approximately 40 nm range. The outcomes of the tuning experiment provided strong motivation to investigate dual-wavelength functioning. For dual-wavelength operation, a 6 mm regular BRF and a 24 mm off surface axis BRF were used. With the regular BRF, DW output with 17-25 nm wavelength separation was obtained as per the calculated FSR for this BRF. On the other hand, using a 24 mm BRF, the tuning of the DW output with wavelength separation from 3.76 nm to 19.76 nm was recorded. Hopefully, the generation of the CR laser beams with such a high quality and power with tunable dual-wavelength output is a landmark in the CR laser field and will boost the various applications [4.2] of the CR lasers. Up to this point, the laser performance was good, and our next goal was ultrashort pulse operation which will be presented in chapters 5 and 6.

REFERENCES

[4.1] W. R. Hamilton, “Third supplement to an essay on the theory of systems of rays,” Trans. R. Irish Acad. 17, 1(1837).

[4.2] A. Turpin, Y. V. Loiko, T. K. Kalkandjiev, and J. Mompart, "Conical refraction: fundamentals and applications," Laser Photon. Rev. 10, 750–771 (2016).

[4.3] H. Lloyd, “On the phenomena presented by light in its passage along the axes of biaxial crystals,” Philos. Mag. 2, 112 (1833)

[4.4] J. C. Poggendorff, “Ueber die konische refraction,”Ann. Phys. Chem. 124, 461 (1839).

[4.5] W. Voigt, “Theoretisches und Experimentelles zur Aufklarung des optischen verhaltens aktiver Kristalle,”Ann. Phys. Chem. 323, 645 (1905).

[4.6] C. F. Phelan, K. E. Ballantine, P. R. Eastham, J. F. Donegan, and J. G. Lunney, “Conical diffraction of a Gaussian beam with a two-crystal cascade,” Opt. Express 20, 13201 (2012).

[4.7] G. S. Sokolovskii, D. J. Carnegie, T. K. Kalkandjiev, and E. U. Rafailov, “Conical Refraction: New observations and a dual cone model,” Opt. Express 21, 11125 (2013).

[4.8] M. V. Berry, “Conical diffraction asymptotics: fine structure of Poggendorff rings and axial spike,” J. Opt. A 6, 289 (2004).

[4.9] A. M. Belsky and M. A. Stepanov, “Internal conical refraction of coherent light beams,” Opt. Commun. 167, 1 (1999).

[4.10] M. V. Berry, M. R. Jeffrey, and J. G. Lunney, “Conical diffraction: Observations and theory,” Proc. R. Soc. A 462, 1629 (2006).

[4.11] A. Turpin, Y. V. Loiko, T. K. Kalkandjiev, H. Tomizawa, and J. Mompart, “Super-Gaussian conical refraction beam,” Opt. Lett. 39, 4349 (2014).

[4.12] R. Cattoor, I. Manek-Hönninger, D. Rytz, L. Canioni, and M. Eichhorn, “Laser action along and near the optic axis of a holmium-doped $KY(WO_4)_2$ crystal,” Opt. Lett. 39, 6407 (2014).

[4.13] K. G. Wilcox, A. Abdolvand, T. K. Kalkandjiev, and E. U. Rafailov, “Laser with simultaneous Gaussian and conical refraction outputs,” Appl. Phys. B 99, 619 (2010).

[4.14] J. Hellström, H. Henricsson, V. Pasiskevicius, U. Bünting, and D. Haussmann, “Polarization-tunable Yb:KGW laser based on internal conical refraction,” Opt. Lett. 32, 2783 (2007).

[4.15] A. Brenier, "Lasing with conical diffraction feature in the $KGd(WO_4)_2$:Nd biaxial crystal," Appl. Phys. B 122, 237 (2016).

[4.16] A. Abdolvand, K. G. Wilcox, T. K. Kalkandjiev, and E. U. Rafailov, "Conical refraction Nd:$KGd(WO_4)_2$ laser," Opt. Express 18, 2753 (2010).

[4.17] R. Akbari, C. Howlader,1 K. A. Fedrova, G. S. Sokolovoskii, E. U. Rafailov and A. Major, "Conical refraction output from a Nd: YVO_4 with an intracavity conerefringent element," Opt. Lett. 44(3), 642 (2019).

[4.18] K. Naganuma, G., Lenz, and E.P. Ippen, "Variable bandwidth birefringent filter for tunable femtosecond lasers," IEEE J. Quantum Electron. 28(10), 2142-2150 (1992).

[4.19] U. Demirbas, R. Uecker, J.G. Fujimoto, and A. Leitenstorfer, "Multicolor lasers using birefringent filters: experimental demonstration with Cr:Nd:GSGG and Cr:LiSAF," Opt. Express 25(3), 2594-2607 (2017).

[4.20] U. Demirbas, "Off-surface optic axis birefringent filters for smooth tuning of broadband lasers," Appl. Opt. 56(28), 7815-7825 (2017).

[4.21] S. M. Kobtsev and N. A. Sventsitskaya, "Application of birefringent filters in continuous-wave tunable lasers: a review," Opt. Spectrosc. 73(1), 114-123 (1992)

[4.22] U. Demirbas, J. Wang, G. S. Petrich, S. Nabanja, J.R. Birge, L.A. Kolodziejski, F.X. Kartner, and J.G. Fujimoto, "100-nm tunable femtosecond Cr:LiSAF laser mode locked with a broadband saturable Bragg reflector," Appl. Opt. 56(13), 3812-3816 (2017)

[4.23] Md. A. R. Reza, C. Dyck, S. Manjooran, P. Loiko, A. Major, "Optimized birefringent filter design for multi-wavelength operation of Yb-ion lasers," Proc. SPIE 10513, 105131L (2018).

[4.24] S. Zhu, "Birefringent filter with tilted optic axis for tuning dye lasers: theory and design," Appl. Opt. 29(3), 410-415 (1990).

[4.25] S. Manjooran, P. Loiko, and A. Major, "A discretely tunable dual-wavelength multi-watt Yb:CALGO laser," Appl. Phys. B 124(1), 13 (2018).

Chapter 5

Mode-locked Yb:CALGO laser with high peak power and sub-100 fs pulses at 27 MHz repetition rate

In this chapter, the mode locking operation of a diode-pumped Yb:CALGO laser will be presented. Typically, the repetition rate of the mode-locked lasers is around 80 MHz. However, an application like fluorescence imaging requires oscillators with low repetition rate to avoid signal aliasing issues. The goal was to develop a low repetition rate mode-locked Yb:CALGO laser by extending the laser cavity. To extend the laser cavity in this experiment, a 1:1 imaging telescope was used. Before jumping into the experimental setup and results, the concept of mode locking and some relevant topics will be discussed in the following sections.

5.1 Introduction to mode locking

Mode locking technique is popular to obtain ultrashort pulses in the picosecond or femtosecond regime. In a free running laser, the oscillating longitudinal modes have neither fixed mode to mode amplitude nor phase relationship. The output is a statistical average of all the longitudinal modes [5.1]. In a Fabry-Perot resonator with two mirrors separated by a distance L, multiple longitudinal (frequency) modes can exist with frequency separation of $\Delta\upsilon = \frac{c}{2L}$, where c is the speed of light as shown in figure 5.1(a) [5.2]. In the mode locking regime, all the longitudinal modes are locked in phase so that a constructive superposition occurs among them which results in the generation of a very intense ultrashort pulse inside the cavity. In a mode-locked laser, the duration of the pulse is inversely proportional to the number of existing longitudinal modes in the cavity i.e. the spectral bandwidth of the laser radiation. The time-bandwidth product of a bandwidth-limited pulse indicates how close a pulse duration is to the value set by its spectral bandwidth. For a Gaussian-shaped pulse, the product of temporal duration Δt (FWHM) and spectral width $\Delta\upsilon$ (FWHM) is $\Delta t\Delta\upsilon = 0.44$ and for a $sech^2$ shaped pulse, this value is $\Delta t\Delta\upsilon = 0.315$.

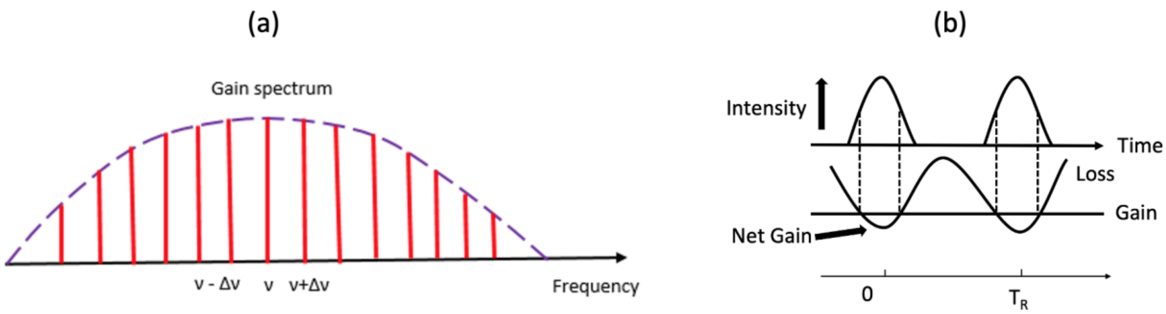

Figure 5.1: Mode locking process in (a) frequency domain and (b) time domain [5.2].

Mode locking can be done by the introduction of a loss mechanism synchronous with pulse round trip time in the cavity. This can be done by the external signal applied to the intracavity loss modulator (active mode locking) or by using a saturable absorber (passive mode locking). Active mode locking can be achieved by means of an electro-optic modulator or acousto-optic modulator which is driven by the external signal to modulate the phase or amplitude of intracavity radiation. In the frequency domain, a mode with frequency ν generates two new sideband modes with frequencies ν+Δν and ν-Δν after modulation. Thus, the energy from the corresponding central mode distributes among the generated sideband modes. More generated sidebands with frequencies ν+nΔν and ν-nΔν are created with each cavity roundtrip of the radiation which falls within the bandwidth of the gain medium. The coupling of these sidebands with their neighboring modes will lock all the modes in phase which causes constructive interference among those modes. As a result, ultrashort pulse in the picosecond or femtosecond regime is produced. In time-domain operation, the modulation produces a time-dependent loss as shown in figure 5.1(b). To produce pulses, there should be a synchronization between loss dips below the gain level and the pulse round trip time. The energy within this window will be amplified while at other times it will be suppressed.

One can obtain much shorter pulses with passive mode locking because of fast loss modulation [5.2-5.4]. Semiconductor saturable absorber mirror (SESAM) and Kerr-lens mode locking (KLM) have become popular for passive mode locking. These procedures will be discussed individually in the following sections and also the combination of these two which is known as KLAS (Kerr-lens and saturable absorber) mode locking will be discussed as well.

The mode locking operation can be divided into 3 categories, continuous-wave mode locking (CW-ML), Q-switched mode locking (QS-ML) and multi-pulsing. The QS-ML and multi-pulsing ML are undesirable and known as mode locking instabilities and the recovery dynamics of SESAM plays a role behind these mechanisms. The criterion to avoid QS-ML was derived by Honninger et al. [5.5] which is given below:

$$E_p^2 > E_{sat,\ laser}\, E_{sat,\ SESAM}\, \Delta R \tag{5.1}$$

where E_p is the intracavity pulse energy, $E_{sat,\ laser}$ is the saturation energy of the gain medium, $E_{sat,SESAM}$ is the saturation energy of the SESAM and ΔR is the modulation depth of the SESAM. $E_{sat,laser}$ can be defined as:

$$E_{sat,\ laser} = F_{sat,\ L}\, A_L = (h\nu/m\sigma)\, A_L \tag{5.2}$$

where $F_{sat,L}$ is the fluence on the gain medium, A_L is the beam area on the gain medium, m is the number of passes through the gain medium per round trip and σ is the emission cross-section. Based on equation 5.1 & 5.2, the gain medium with larger stimulated emission cross-section makes it easier to avoid QS-ML as it decreases the gain saturation fluence.

On the other hand, multi-pulsing instabilities can occur due to high fluence on the SESAM when the laser system cannot differentiate between a single pulse and multiple pulses travelling in the cavity if both have the same level of fluence. The multi-pulsing instabilities set the upper limit to the output power of a mode-locked laser system [5.6].

In the next sub-sections, the details mode locking will be discussed including SESAM, KLM and the combination of both methods.

5.1.1 SESAM mode locking

SESAM is a mirror structure with an integrated saturable absorber. It contains a Brag mirror which acts as the reflector with a quantum well absorber layer embedded in it as shown in figure 5.2(a). For incident light with low intensity, excitation of electrons from the valence band to the conduction band causes absorption. On the other hand, high-intensity light saturates (i.e. fills) the conduction band and as a result, no absorption occurs. Therefore, when a pulse is incident on a SESAM, the low-intensity portions of the pulse (wings) are absorbed thus saturating the absorption of the SESAM for the high intensity central part of the pulse. So, the central part of the pulse is transmitted without loss. In this way, SESAM can shorten a pulse. It is easier and more convenient to implement mode locking using SESAM because the design of the cavity is simpler and mode locking initiation is usually self-starting. Figure 5.2 is a schematic of a typical SESAM structure.

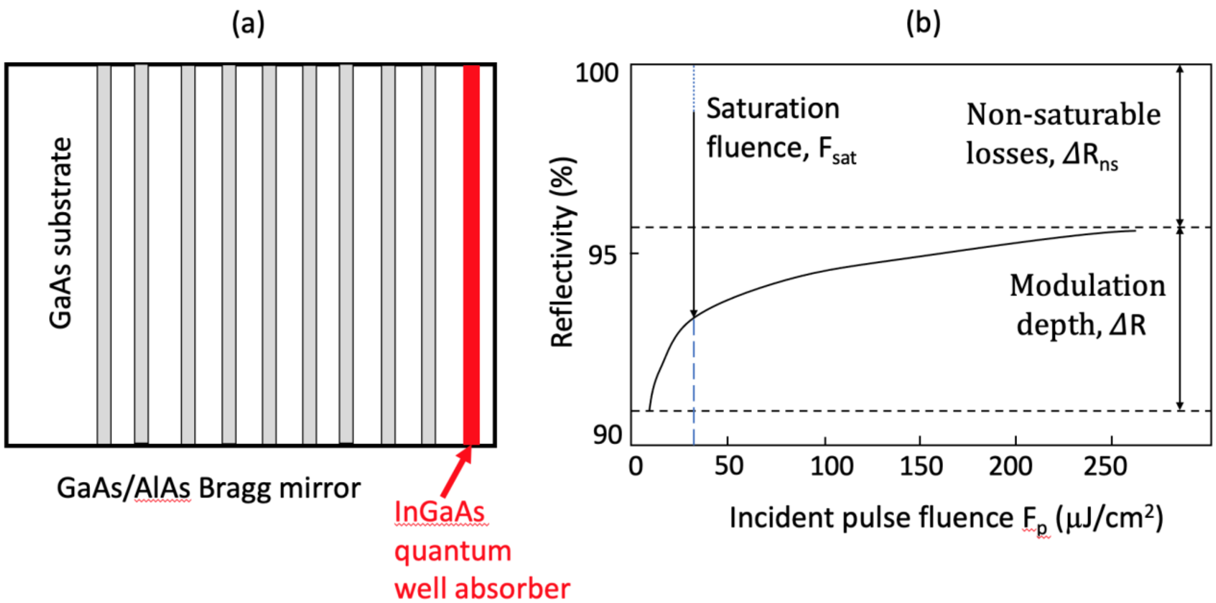

Figure 5.2: (a) Structure of a SESAM [5.5] and (b) its important properties [5.3].

The most important parameters of SESAM are the wavelength range, modulation depth, dynamic response, non-saturable losses and saturation fluence which are shown in 5.2(b). Modulation depth (max introduced loss) can be defined as the maximum nonlinear change in reflectivity. On the other hand, saturation fluence is defined as the level of incident fluence which causes saturation in absorption, i.e. it reduces the absorption of the SESAM by 1/e (37%) of its initial value. The non-saturable loss should be low as it does not contribute to the pulse shaping, but it increases the device heating effect and the threshold of the laser. For high-power laser operation, the modulation depth should be strong enough in order to shape the pulse properly. The incident laser beam spot should be wide as it distributes the generated heat over the large area [5.3, 5.5, 5.7]. Large modulation depth and fast recovery time are the reasons behind the increase in non-saturable losses [5.7].

5.1.2 Kerr-lens mode locking (KLM)

Kerr-lens mode locking can be observed due to the third-order non-linearity effect in a Kerr medium. A Gaussian pulse with high intensity can modulate the refractive index of the medium through the Kerr effect as shown in the equation below:

$$n(I) = n_0 + n_2 . \mathrm{I}\ (\mathrm{r.t}) \tag{5.3}$$

where n_o is the original refractive index of the medium and n_2 is the nonlinear refractive index due to the passing of highly intense beam. The modulated refractive index usually behaves as a positive lens where the central part of the pulse experiences a strong focusing effect compared to the other parts of the pulse (i.e. wings).

The initiation of loss modulation can be done by introducing an aperture behind the gain medium as shown in Figure 5.3. This aperture allows only the central part of the light pulse to be transmitted and subsequently amplified while the leading and trailing portions of the pulse will be blocked by the aperture. The aperture could be a real one which is known as a hard aperture Kerr-lens mode locking. On the other hand, implementation of the artificial aperture can be done by tightly focusing the pump beam on the small region of the laser crystal to create a small gain volume. Only the central part of the lasing pulse gets focused & amplified which helps to get an ultrashort pulse.

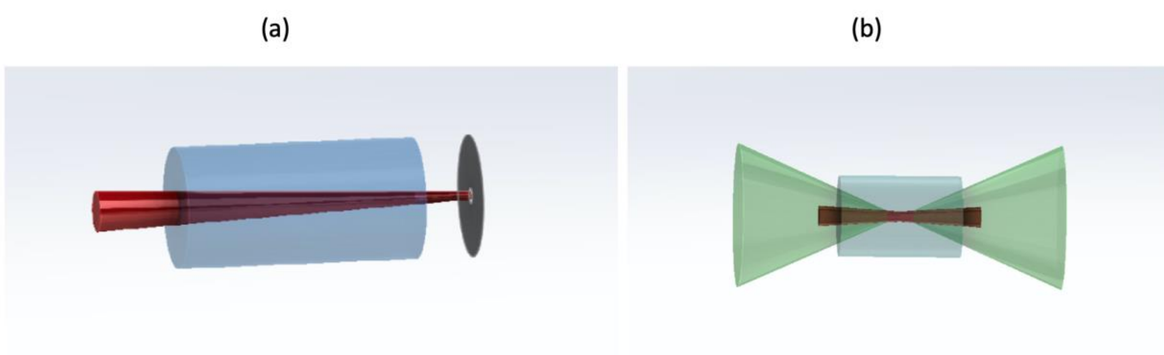

Figure 5.3: Kerr lens mode locking: (a) hard aperture and (b) soft aperture [5.8].

Due to the modulation by the highly intense pulse, the pulse spectrum becomes broader due to self-phase modulation (SPM), which is crucial for obtaining ultrashort pulses (this also happens for SESAM). The initiation of Kerr-lens mode locking is tough because high beam intensity is needed to induce the Kerr effect. Usually, the manually created mechanical vibration on one of the end cavity mirrors will start the process [5.3, 5.8, 5.9].

In general, Kerr-lens mode locking can generate shorter pulses compared to SESAM mode locking because of its very fast saturable absorption like property. The design procedure for Kerr-lens mode locking requires that the resonator operation should be conducted near the cavity stability limit. The starting of the Kerr lens mode locking requires mechanical perturbation as mentioned above, but the SESAM mode locking process is self-starting. On the other hand, SESAM has drawbacks such as the probability of being damaged by a highly intense laser beam with a small beam size [5.3]. It is also costly.

5.1.3 KLAS mode locking

A method which is known as KLAS mode locking is the combination of Kerr-lens mode locking and SESAM mode locking. It uses the advantages of both methods such as the stable and self-starting mode locking offered by SESAM, and KLM which suppresses the Q-switched mode locking effect and multi-pulsing instabilities at high pump power. In addition to that, both SESAM and KLM also help by spectral broadening through additional SPM effect which will lower the pulse duration. Because of this dual action, KLAS is an ideal candidate for sub-100 fs mode locking operation [5.10].

5.2 Dispersion compensation

In mode locking operation, when a pulse travels through the gain medium and other intracavity elements, it gets temporarily stretched due to velocity variation for the different spectral components which is known as group velocity dispersion (GVD). An appropriate amount of negative dispersion should be introduced into the cavity to overcome this positive dispersion effect. A pair of prisms cut at Brewster’s angle can be added as an additional cavity element [5.11].

Another way to introduce the negative dispersion in the cavity is by using a Gires-Tournois interferometer (GTI) mirror. It is similar to a Fabry-Perot resonator and consists of a front partial reflective mirror and a highly reflective back mirror (figure 5.4). The spectral components of the incident pulse will be changed in phase which will yield negative dispersion. The insertion loss is low for GTI mirrors, and it is less sensitive to the cavity alignment [5.12].

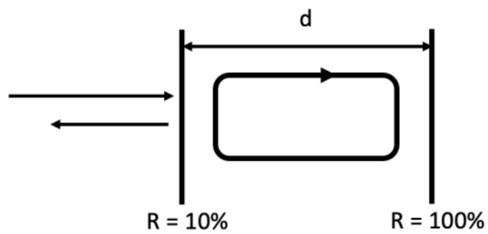

Figure 5.4: Schematic of a GTI mirror.

5.3 Extended cavity oscillators

The peak power of the oscillating pulse in a mode locked oscillator can be defined as:

$$P_{peak} = \frac{E}{\tau} = \frac{P_{avg}}{\tau f} \tag{5.4}$$

where E is the pulse energy, τ is the pulse duration, P_{avg} is the average output power and f is the repetition rate. To increase the peak power, one should increase the average output power or decrease the pulse duration and the repetition rate. Although Ti:sapphire laser has provided megawatt peak power with sub-10 fs pulses [5.13], this is difficult for the Yb-ion lasers because of their comparatively narrow emission bandwidth. Also the broadband gain medium such as Yb:Glass has a low thermal conductivity which limits the average output power. Fortunately the situation has been changed with the development of Yb:CALGO laser crystal with broadband emission bandwidth and high thermal conductivity. Another method to increase pulse energy is by reducing the pulse repetition rate. The repetition rate is inversely proportional to the cavity length as shown in equation 5.5. So, by increasing the cavity length, one can easily reduce the repetition rate.

$$f = \frac{c}{2L} \tag{5.5}$$

where in equation 5.5, f is the repetition rate, c is the speed of light and L is the length of the cavity. It is clear from equations 5.4 and 5.5 that extending the laser cavity will increase the peak power. A convenient way to extend the laser cavity is to use a reflective 1:1 imaging telescope.

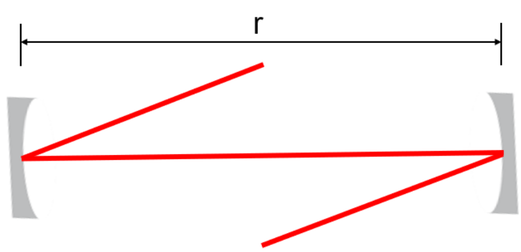

Figure 5.5: 1:1 imaging telescope to extend the laser cavity without changing the q-parameter.

A 1:1 imaging telescope (figure 5.5) can be inserted at any point of the cavity without changing the cavity q-parameter (Appendix C) which contains the information of a Gaussian beam radius and radius of curvature of wavefront. Usually, it consists of two concave mirrors of the same radius of curvature r. These two mirrors are placed at a distance of r from each other, and it will add a 4r to the total cavity length in a single round-trip.

5.4 Motivation behind this experiment

Femtosecond laser system has become an essential tool for applications in the field of nonlinear microscopy and spectroscopy [5.14-5.17], optical coherence tomography [5.18, 5.19], optical communication [5.20], surgical applications [5.21] etc. Because of these useful applications, researchers have put a lot of effort into developing oscillators in sub-100 fs regime with megawatt peak power. Application such as fluorescence imaging would need this type of source to avoid the signal aliasing problem. The popular traditional way to get the high peak power sub-100 fs pulses by using a 1:1 imaging telescope configuration which was already discussed in section 5.3. The implementation of this method was successful for Yb:CALGO [5.22-5.24] Yb:KGW [5.29-5.30], Yb:Glass [5.31], Yb:KYW [5.32, 5.33], Yb:YAG [5.34] in previous experiments. The detailed results would be discussed in section 5.7. Getting sub-100 fs pulses with high peak power is difficult in the low repetition rate regime (<40 MHz) because it needs excellent mode locking performance of the laser and a careful choice of the appropriate laser crystal. It was discussed in chapter 1 that Yb:CALGO is a good choice for high power ultrashort pulse experiments because of its high emission bandwidth and thermal conductivity[5.22-5.28]. So, the next step was to get a stable mode locking performance from the laser in the extended cavity operation with a 1:1 imaging telescope. The sub-100 fs pulses with lower repetition rate and high peak power would be a good choice for the above-mentioned applications.

5.5 Experimental setup

The laser oscillator used the same laser crystal that was mentioned in the previous chapters and the pump source was also same. The unpolarized pump beam was focused into the laser crystal by using two lenses of 50 mm and 75 mm focal length and the resultant spot size was 157.5 μm. The laser crystal was positioned between two folding mirrors M1 and M2 with a radius of curvature of -250 mm. The laser mode inside the crystal was approximately 142 μm in diameter which was estimated by using ABCD matrix analysis. Approximately 56% of the pump power was absorbed in the laser crystal under non-lasing condition. The laser cavity was extended by using a 1:1 imaging telescope which was formed by using two concave mirrors of -2000 mm radius of curvature (figure 5.6). The resultant cavity length was 5573 mm which corresponded to a 26.9 MHz repetition rate. The laser introduces positive dispersion from the laser crystal (95 fs^2/mm) [5.35] and the intracavity optical components. Also, the self-phase modulation introduces pulse chirping. To compensate for the positive dispersion effects, two Gires-Tournois interferometer (GTI) mirrors were used, and the total round-trip dispersion was -3200 fs^2 per round trip by using two bounces on a -250 fs^2 and -550 fs^2 GTI mirrors (Layertech GmbH). The rest of the cavity mirrors were chosen to have the lowest possible (closer to zero at 1040 nm) group delay dispersion (GDD) in the cavity (Laseroptik GmbH). As a mode locking element, a semiconductor saturable absorber mirror (SESAM) designed for 1040 nm and with 1.2 % of modulation depth was used as an end mirror of the cavity. To avoid damage of the SESAM, the beam spot size on the SESAM was kept at 379 μm in radius. 5%, 10%, 15% and 20% output couplers were used in this experiment.

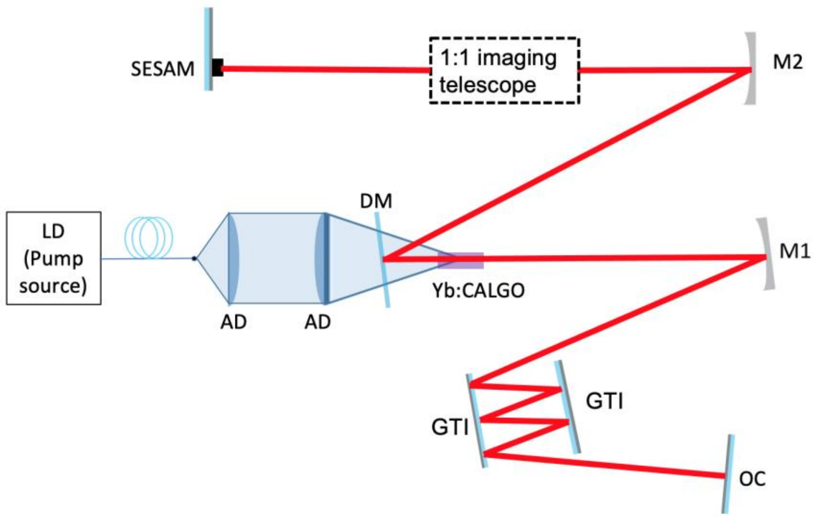

Figure 5.6: The schematic of the mode-locked Yb:CALGO laser. AD: achromatic doublet, DM: dichroic mirror, GTI: Gires-Tournois interferometer mirror, M1, M2: concave mirrors, OC: output coupler.

5.6 Results and discussion

Initially, the laser performance was monitored in the continuous-wave (CW) regime using a 10% output coupler (OC). A highly reflecting mirror (HR) was used instead of the SESAM as an end mirror. With the 10% output coupler, approximately 7.5 W of average output power was obtained at 25 W of incident pump power. The corresponding absorbed pump power was approximately 14 W. After optimizing the laser in the CW regime, we introduced the SESAM in the cavity by replacing the HR mirror. Although with SESAM, it was expected that mode locking would be self-starting, in our case to start the mode locking we needed to apply a mechanical perturbation to the curved mirror M1 or the output coupler which were put on the translation stages. After mechanical perturbation as mentioned above, it was noticed that the spectrum became wider while the output power was reduced.

The ultrashort pulses were measured by using an intensity autocorrelator (Femtochrome FR-103 XL) with resolution <5 fs. To detect multi-pulsing and make sure the laser is operating in the single pulse regime, the autocorrelator was scanned over the range of 200 ps. The pulses that could be separated by more than 200 ps were monitored by using a combination of an oscilloscope and fast photodiode. The spectra were recorded by Anritsu spectrometer (MS9710B) with 0.07 nm resolution.

With 10% output coupler, the shortest pulses obtained pulses were 90 fs long with 350 mW of output power at approximately 8 W of incident pump power and the recorded spectrum bandwidth (FWHM) was 12.7 nm. This was obtained for -3200 fs^2 round trip dispersion which was achieved by using two GTI mirrors of -250 fs^2 and -550 fs^2 each and having two bounces on each GTI mirrors. The calculated time-bandwidth product was 0.32 i.e. the pulses were transform limited. The corresponding pulse energy and peak power were 13 nJ and 145 kW. To investigate the best possible results from the laser, 5%, 15% and 20% OCs were used. The highest average output power was 1.3 W which was obtained with a 20% output coupler at 17 W of incident pump power and the corresponding pulse duration was 81 fs (figure 5.7(a)) while the round-trip dispersion was -3200 fs^2.The spectrum was centered at 1038 nm and had an FWHM bandwidth of 14.14 nm (figure 5.7(b)). The calculated time-bandwidth product was 0.32 which indicated that the obtained pulses were transform-limited. The pulse energy and the peak power were 48 nJ and 596 kW, respectively. The shortest pulse duration obtained for 5% and 15% output couplers were 85 fs and 91 fs at the total round-trip dispersion of -3200 fs^2. The corresponding spectrum bandwidths at FWHM were 13.32 nm and 12.5 nm respectively.

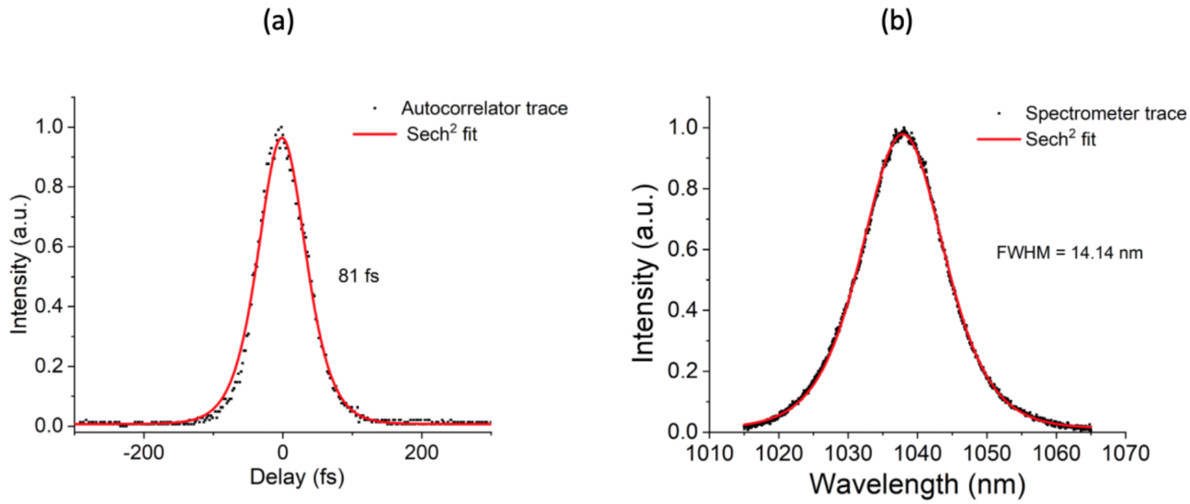

Figure 5.7: (a) Intensity autocorrelation of the 81 fs pulses and (b) the corresponding spectrum with 14.14 nm bandwidth at FWHM.

The radio frequency spectrum of the pulse train was also recorded and a high signal-to-noise ratio in figure 5.8(a) indicates that we had a clean mode locking without any Q-switching instabilities. The output beam quality factor M^2 was approximately 1 which is shown in figure 5.8(b).

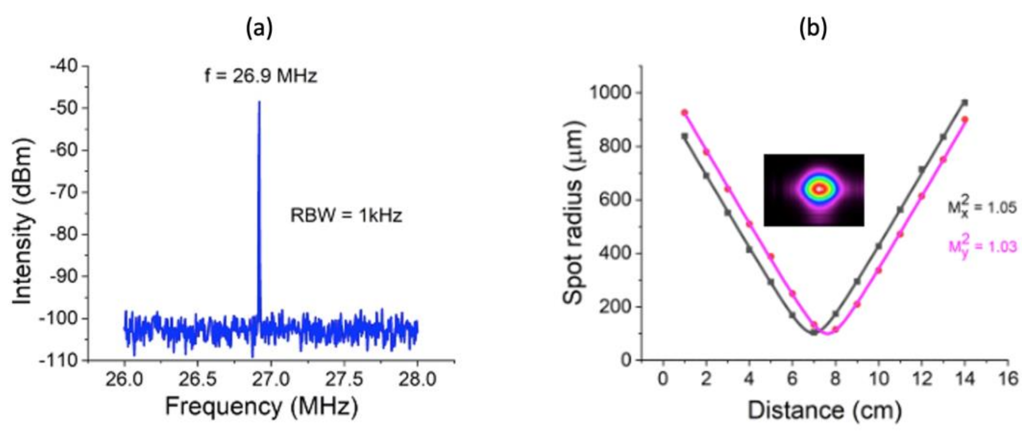

Figure 5.8. RF spectrum of the 81 fs pulse train recorded with a 1 kHz resolution bandwidth and the beam quality measurement.

Getting a stable mode locking with high average output power was difficult for us due to the multi-pulsing effect (discussed in section 5.1). To avoid multi-pulsing, maximum 17 W of incident pump power was used. The pulse duration and average output power were recorded at different dispersion levels. In search of the highest output power, two GTI mirrors of dispersion value -550 fs^2 each were used, which gave a total round-trip dispersion of -4400 fs^2. In this case, the output power was 1.55 W at the same incident pump power level at the expense of longer pulse duration (124 fs). The mode locking performance was monitored by using 5%, 10% and 15% output couplers as well. The pulse duration obtained for these output couplers with the total round-trip dispersion of -4400 fs^2 were 115 fs, 118 fs and 119 fs, respectively. The spectrum bandwidths at FWHM were 10 nm, 9.8 nm and 9.75 nm, respectively. The corresponding output powers were 285 mW at 7.6 W of incident pump power, 600 mW at 9.3 W of incident pump power and 1.09 W at 13 W of incident pump power, respectively.

5.7 Comparison with previous results

The summary from the previous extended-cavity Yb-ion lasers is presented in figure 5.9. The repetition rates were usually from 10 MHz to 40 MHz. From figure 5.9(a), it can be seen that there are very few experiments where the laser delivered sub-100 fs pulses.

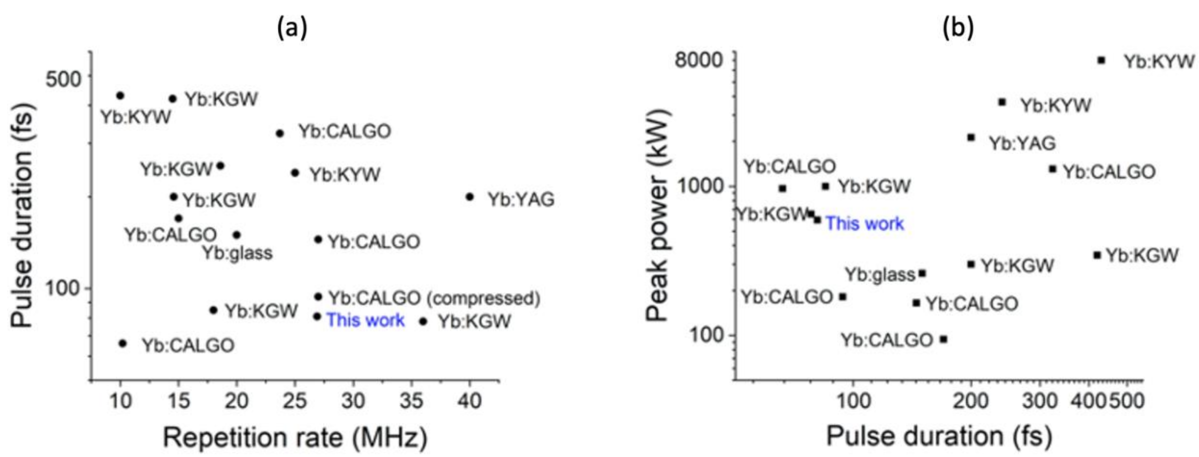

Figure 5.9. Comparison of previous results with this work in terms of the (a) pulse duration and (b) peak power in the 10-40 MHz repetition rate range.

From Yb:CALGO crystal 145 fs pulses were obtained at 27 MHz of repetition rate directly from the laser, while after external compression 93 fs pulses were measured [5.22]. In the same work, 170 fs pulses were generated at 15 MHz repetition rate. In Ref. 5.23, 300 fs pulses were reported at 23 MHz repetition rate with 28 W of average output power from thin-disk Yb:CALGO oscillator. The same authors also reported on 135 fs pulses with 1.3 W of output power at the same repetition rate. In Ref. 5.24, 323 fs pulses were obtained at 23.7 MHz repetition rate. A very impressive result was presented by Manjooran et al. in Ref. 5.25 where 66 fs pulses at 10.2 MHz repetition rate based on KLM were reported. Apart from Yb:CALGO, there were some other experiments for Yb:KGW, Yb:KYW, Yb:Glass, Yb:YAG etc. Zhao et al. in Ref. 5.29 reported 78 fs pulses directly from the Yb:KGW laser output without any external compression at 36 MHz repetition rate and 85 fs pulses at 18 MHz repetition rate. In other experiments, 200 fs pulses were reported for Yb:KGW at 14.6 MHz repetition rate [5.30], 150 fs pulses were reported at 20 MHz repetition rate for Yb:Glass [5.31], 240 fs & 430 fs pulses were reported for Yb:KYW at 25 MHz & 10 MHz repetition rate [5.32, 5.33], and 200 fs pulses were reported at 40 MHz repetition rate for Yb:YAG think-disk oscillator [5.34]. Compared to the above results, 81 fs pulses at a 26.9 MHz repetition rate were recorded directly from the laser without any external compression. It is considered that a dual action of SESAM and KLM was present in the cavity which helped us to get these shorter pulses. No mode locking based on pure KLM was observed. Out of 6 listed results in section 5.6, the best one was with 81 fs pulses in terms of the pulse duration, so this one is compared with the previously published results in figure 5.9.

Another comparison with the previous works can be made with the peak power which is shown in figure 5.9(b). Considering the sub-100 fs regime for Yb:CALGO lasers, approximately 970 kW of peak power was reported in Ref. 5.25 and 165-183 kW in Ref. 5.22. Haitao et al. reported 650 kW of peak power for Yb:KGW at 36 MHz repetition rate while for the 18 MHz cavity, the peak power was as high as 1 MW [5.29]. Compared to these results, 596 kW of peak power at a 26.9 MHz repetition rate was obtained in this experiment which is fairly good.

5.8 Conclusion

In conclusion, the generation of sub-100 fs pulses with high peak power from the extended cavity mode-locked Yb:CALGO oscillator has been demonstrated. 81 fs pulses with 1.3 W of output power at 17 W of incident pump power were recorded. The laser output beam quality was approximately 1 while the high signal-to-noise ratio of the RF spectrum ensured that the mode locking was free from Q-switched mode locking instabilities. The mode locking was obtained based on a semiconductor saturable absorber mirror with 1.2% modulation depth. The initiation of mode locking was not self-starting. One of the end cavity mirrors needed to be tapped. A weak Kerr-lensing effect could be present in the cavity, and it may have assisted in generating these shorter pulses. However, no signs of pure Kerr-lens mode locking were seen by replacing the SESAM with an HR mirror. Overall, the performance was good, and the laser was stable throughout the measurement period.

The next goal was to reduce the repetition rate below 26.9 MHz. To do that, one needs to add another 1:1 imaging telescope or one can do that by incorporating a mirror with a longer radius of curvature. In these cases, the alignment process would be complicated and require more space. In the next chapter, a simple and compact design method to lower the repetition rate by using an intracavity White cell will be discussed.

REFERENCES

[5.1] W. Koechner, Solid-State Laser Engineering, vol. 6. Springer New York, 2007.

[5.2] H. A. Haus, "Mode locking of lasers," IEEE J. Sel. Top. Quantum Electron. 6, 1173–1185 (2000).

[5.3] U. Keller, "Recent developments in compact ultrafast lasers," Nature 424, 831–838 (2003).

[5.4] U. Keller, "Ultrafast solid-state laser oscillators: a success story for the last 20 years with no end in sight," Appl. Phys. B 100, 15–28 (2010).

[5.5] C. Hönninger, R. Paschotta, F. Morier-Genoud, M. Moser, and U. Keller, ―Q-switching stability limits of continuous-wave passive mode locking, J. Opt. Soc. Am. B 16, 46-56 (1999).

[5.6] T. Waritanant, "Highly efficient diode-pumped lasers based on In-band pumping of Nd:YVO4 crystal", Ph.D. thesis dissertstion, University of Manitoba (2017).

[5.7] R. Paschotta, "Encyclopedia of laser physics and technology." [Online]. Available: https://www.rp-photonics.com/semiconductor_saturable_absorber_mirrors.html.

[5.8] Available at: https://en.wikipedia.org/wiki/Kerr-lens_modelocking

[5.9] J. Herrmann, "Theory of Kerr-lens mode locking: role of self-focusing and radially varying gain," J. Opt. Soc. Am. B 11, 498 (1994).

[5.10] S. Manjooran and A. Major, "Generation of Sub-50 fs Pulses With >1.5 MW of Peak Power From a Diode-Pumped Yb:CALGO Laser Oscillator", Conference on Lasers and Electro-Optics(CLEO 2016.

[5.11] R. Paschotta, "Encyclopedia of laser physics and technology." [Online]. Available: https://www.rp-photonics.com/prism_pairs.html

[5.12] R. Paschotta, "Encyclopedia of laser physics and technology." [Online]. Available: https://www.rp-photonics.com/gires_tournois_interferometers.html

[5.13] L. Xu, G. Tempea, A. Poppe, M. Lenzner, Ch. Spielmann, F. Krausz, A. Stingl, K. Ferencz, "Highpower sub-10-fs Ti:sapphire oscillators," Appl. Phys. B 65, 151-159 (1997).

[5.14] W. R. Zipfel, R. M. Williams, and W. W. Webb, "Nonlinear magic: multiphoton microscopy in the biosciences," Nat. Biotechnol. 21, 1369–1377 (2003).

[5.15] D. Kobat, M. E. Durst, N. Nishimura, A. W. Wong, C. B. Schaffer, and C. Xu, "Deep tissue multiphoton microscopy using longer wavelength excitation," Opt. Express 17, 13354 (2009).

[5.16] H. Kano and H. Hamaguchi, "Femtosecond coherent anti-Stokes Raman scattering spectroscopy using supercontinuum generated from a photonic crystal fiber," Appl. Phys. Lett. 85, 4298 (2004).

[5.17] J. Mandon, E. Sorokin, I. T. Sorokina, G. Guelachvili, and N. Picqué, "Supercontinua for high-resolution absorption multiplex infrared spectroscopy," Opt. Lett. 33, 285 (2008).

[5.18] J. G. Fujimoto, A. D. Aguirre, Y. Chen, P. R. Herz, P.-L. Hsiung, T. H. Ko, N. Nishizawa, and F. X. Kärtner, "Ultrahigh-Resolution Optical Coherence Tomography Using Femtosecond Lasers," in Ultrashort Laser Pulses in Biology and Medicine, M. Braun, P. Gilch, and W. Zinth, eds. (Springer Berlin Heidelberg, 2008), pp. 3–27.

[5.19] W. Drexler, U. Morgner, F. X. Kärtner, C. Pitris, S. a Boppart, X. D. Li, E. P. Ippen, and J. G. Fujimoto, "In vivo ultrahigh-resolution optical coherence tomography," Opt. Lett. 24, 1221 (1999).

[5.20] E. A De Souza, M. C. Nuss, W. H. Knox, and D. A. B. Miller, "Wavelength-division multiplexing with femtosecond pulses," Opt. Lett. 20, 1166 (1995).

[5.21] T. Juhasz, F. H. Loesel, R. M. Kurtz, C. Horvath, J. F. Bille, and G. Mourou, "Corneal refractive surgery with femtosecond lasers," IEEE J. Sel. Top. Quantum Electron. 5, 902–910 (1999).

[5.22] D.N. Papadopoulos, D. Druon, J. Boudeile, I. Martial, M. Hanna, P. Georges, P.O. Petit, P. Goldner, and B. Viana, "Low-repetition rate femtosecond operation in extended- cavity mode-loked Yb: CALGO laser", Opt. Lett. 34(2), 196-198 (2009).

[5.23] S. Ricaud, A. Jaffres, K. Wentsch, A. Suganuma, B. Viana, P. Loiseau, B. Weichelt, M. Abdou-Ahmed, A. Voss, T. Graf, D. Rytz, C. Hönninger, E. Mottay, P. Georges, and F. Druon, "Femtosecond Yb:$CaGdAlO_4$ thin-disk oscillator," Opt. Lett. 37(19), 3984–3986 (2012).

[5.24] A. Greborio, A. Guandalini, and J. A. D. Au, "Sub-100fs pulses with 12.5 W from Yb: CALGO based oscillators", Proc. of SPIE Vol. 8235 823511-1 (2012).

[5.25] S. Manjooran and A. Major, "Low repetition rate operation of a femtosecond Yb:CALGO laser", Proc. of SPIE Vol. 10511(2018).

[5.26] Y. Zaouter, J. Didierjean, F. Balembois, G. L. Leclin, F. Druon, and P. Georges, "47 fs diode-pumped Yb^{3+}: $CaGdAlO_4$ laser", Opt. Lett. 31(1), 119-121 (2006).

[5.27] A. Agnesi, A. Greborio, F. Pirzio, G. Reali, J. A. D. Au, and A. Guandalini, “40-fs Yb^{3+}: $CaGdAlO_4$ laser pumped by a single-mode 350-mW laser diode”, *Opt. Express,* vol. 20(9), (2012).

[5.28] A. Klenner, M. Golling, and U. Keller, “High peak power gigahertz Yb: CALGO laser”, *Opt. Express,* vol. 22(9), pp 11884-11891(2014).

[5.29] H. Zhao, and A. Major, “Megawatt peak power level sub-100 fs Yb:KGW oscillators”, Optics express, Vol 22(25), 30425-30431 (2014).

[5.30] A. Major, V. Barzda, P. A. E. Piunno, S. Musikhin, and U. J. Krull, "An extended cavity diode-pumped femtosecond Yb:KGW laser for applications in optical DNA sensor technology based on fluorescence lifetime measurements," *Opt. Express,* vol. 14, pp. 5285-5294, 2006.

[5.31] F. Hoos, S. Pricking, and H. Giessen, “Compact portable 20 MHz solid-state femtosecond whitelight-laser,” Opt. Express 14(22), 10913–10920 (2006).

[5.32] F. Brunner, T. Südmeyer, E. Innerhofer, F. Morier-Genoud, R. Paschotta, V. E. Kisel, V. G. Shcherbitsky, N. V. Kuleshov, J. Gao, K. Contag, A. Giesen, and U. Keller, “240-fs pulses with 22-W average power from a modelocked thin-disk Yb:KY(WO4)2 laser,” Opt. Lett. 27(13), 1162–1164 (2002).

[5.33] E. P. Mottay and C. Hönninger, “MicroJoule level diode-pumped femtosecond oscillator,” Commercial and biomedical applications of ultrafast lasers VII, Proc. SPIE 6460, San Jose, USA, 64600I (2007).

[5.34] O. Pronin, J. Brons, C. Grasse, V. Pervak, G. Boehm, M.-C. Amann, V. L. Kalashnikov, A. Apolonski, and F. Krausz, “High-power 200 fs Kerr-lens mode-locked Yb:YAG thin-disk oscillator,” Opt. Lett. 36(24), 4746–4748 (2011).

[5.35] P.Loiko, P. Becker, L. Bohaty, C. Liebald, M. Peltz, S. Vernay, D. Rytz, J. M. Serres, X. Mateos, Y. Wang, X. Xu, J. Xu, A. Major, A. Baranov, U. Griebner and V. Petrov, “ Sellmier equations, group velocity dispersion, and thermos-optic dispersion formulas for CaLnAlO4 (Ln = Y, Gd) laser host crystals”, Opt. Lett. 42(12), 2275- 2278 (2017).

Chapter 6

Sub-100 fs mode-locked Yb:CALGO laser extended with a White cell configuration

In section 5.3 it has been discussed that the peak power of the oscillating pulse in a mode-locked oscillator can be defined as:

$$P_{peak} = \frac{E}{\tau} = \frac{P_{avg}}{\tau f} \quad (6.1)$$

where E is the pulse energy, τ is the pulse duration, P_{avg} is the average output power and f is the repetition rate. To increase the peak power, one can reduce the pulse repetition rate by extending the laser cavity. In chapter 5, the laser cavity was extended by using a 1:1 imaging telescope to lower the pulse repetition rate to 27 MHz. To reduce it even further one might need to add another 1:1 imaging telescope or one needs to use concave mirrors with a long radius of curvature. Unfortunately, this will make the laser alignment complicated, time-consuming and sensitive. An alternate approach is to use a White cell which will be discussed in this chapter. The White cell consists of 3 concave mirrors, and one can easily control the number of bounces inside the White cell which in turn reduces the repetition rate further. It takes less space and alignment is comparatively simple. In this chapter, the discussion will be focused on extending the laser cavity by using the White cell configuration.

6.1 Introduction

The femtosecond lasers with lower repetition rate (i.e. < 40 MHz) is useful for nonlinear microscopy [6.1, 6.2], optical coherence tomography [6.3-6.5], optical communication [6.6, 6.7] etc. To get laser oscillators with lower repetition rate, one need to increase the cavity length without changing the Gaussian beam q-parameter. There are different techniques to do that such as Herriott type multi-pass cell [6.8], 1:1 imaging telescope [6.9-6.11], or White cell [6.12-6.20]. Considering the design, cost, and easiness of the operation, 1:1 imaging telescope was chosen for the previous experiments in chapter 5 where the repetition rate was 26.9 MHz. However, to lower the repetition rate even further, one need to use more optical components which makes the alignment difficult. An alternative approach is to use a White cell which consists of 3 concave mirrors. It can be inserted at any point in the cavity and the cavity length can be adjusted by simply adjusting the two turning mirrors of the cell. In this section, a White cell configuration was used to extend the laser cavity. The White cell is a simple, compact and cost-effective method to lower the repetition rate of the laser oscillators. Using 3, 5 and 7 bounces on the White cell, the corresponding repetition rate was 13.85 MHz, 10.15 MHz and 8.2 MHz. Pulses as short as 68 fs were recorded. For mode locking, a SESAM was used. There is a possibility that the mode locking was also accompanied by the Kerr-lensing effect which resulted in these shorter pulses. For dispersion compensation, we used chirped mirrors in the cavity. Hopefully, this low repetition rate oscillator with sub-100fs pulses and high peak power will be a great source for applications such as fluorescence imaging and nonlinear microscopy.

6.2 White cell configuration

A 1:1 imaging telescope has been a good candidate for laser cavity extension because of its simple configuration which needs fewer optics and lowers cost. However, to bring the repetition rate down to around 10 MHz, one might need to use two 1:1 imaging telescopes which is quite complicated to implement in the lab because of the complex alignment procedure [6.21].

The multi-pass cell, on the other hand, could be a good solution to this issue. In this experiment, a multi-pass cell, which is also known as a White cell [6.12] was used. The White cell consists of three spherical concave mirrors of the equal radius of curvature as shown in figure 6.1 (a). The left bigger mirror is known as the field mirror and the right two smaller mirrors are known as the turning mirrors. The turning mirrors are placed symmetrically about the central axis of the field mirror and should be put as close as possible to each other to have the highest number of bounces of the optical beam on the field mirror. The photo of the field mirror and the turning mirrors used in this experiment is shown in figure 6.1 (b). The detailed operation of the White cell was explained in earlier work [6.18].

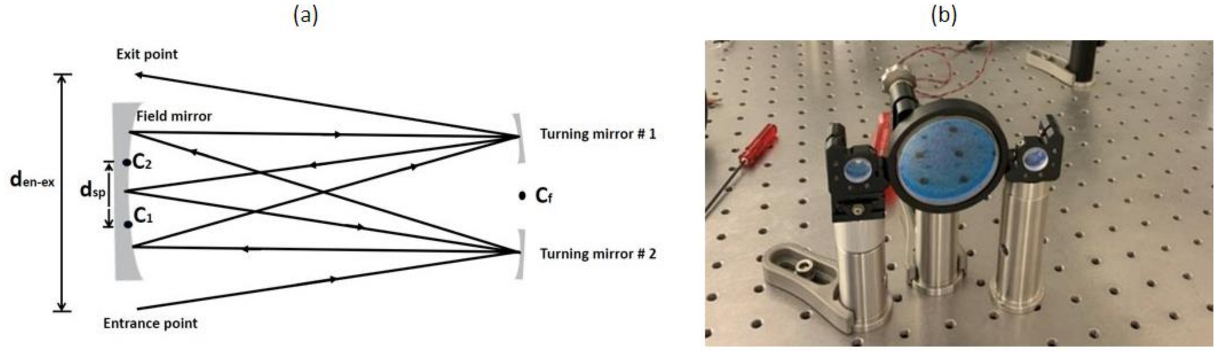

Figure 6.1: (a) The White cell configuration with three concave mirrors with the equal radii of curvature, (b) photo of the field mirror and turning mirrors used in this experiment.

The total number of bounces (N) on the field mirror can be expressed as:

$$N = \frac{d_{en-ex}}{d_{sp}} - 1 \tag{6.2}$$

where d_{en-ex} = spacing between the entrance and exit beams, d_{sp} = distance between C_1 & C_2 which is also equal to the distance between the entrance beam and its nearest spot on the field mirror or the exit beam and its nearest spot on the field mirror, C_f = center of curvature of the field mirror. Since the ratio $\frac{d_{en-ex}}{d_{sp}}$ is constrained to be an integer, simultaneous adjustment of the turning mirrors causes the change of the number of spots on the field mirror as odd integer (1,3,5…….). As the number of bounces on the field mirror increases by two, the optical beam makes 4 extra passes inside the White cell. So, the total optical path length changes as a step of $4R$, where R is the radius of curvature of the mirrors. So, the total optical path L_{wc} in the White cell can be expressed as:

$$L_{wc} = 2NR \tag{6.3}$$

6.3 Experimental setup

The experiment was carried out with a similar laser crystal and same laser diode as the previous experiments. The laser mode radius size inside the crystal was approximately 70 µm which was estimated based on the ABCD analysis. The laser cavity schematic is shown in figure 6.2. By using the White cell configuration, the complex alignment process of multiple telescopes was eliminated. Moreover, it gave the flexibility to vary the repetition rate at 13.85 MHz with 3 bounces on the field mirror (figure 6.3 (a)), 10.15 MHz with 5 bounces on the field mirror (figure 6.3 (b)), and 8.2 MHz with 7 bounces on the field mirror (figure 6.3 (c)) by simply adjusting the turning mirrors. A field mirror (Laseroptik GmbH) with a -1000 mm radius of curvature and 50 mm in diameter was used. The turning mirrors also had -1000 mm radius of curvature. An explanation of the White cell alignment process is provided in Appendix D. Two Gires-Tournois interferometer (GTI) mirrors (Layertec GmbH) with different negative group delay dispersions (GDD) were used to provide a round-trip dispersion of -3200 fs^2. The choice of SESAM is crucial in the low repetition rate and high intracavity energy & peak power. The initial fluctuations of the intracavity power will reach to a stable mode locking if and only if [6.15]:

$$\Delta R > T_r/T_c \tag{6.4}$$

where, T_r is the round-trip time and T_c is the effective correlation time, and ΔR is the modulation depth of the SESAM [6.22], so a SESAM with a large modulation depth (typically 3-6%) is crucial for mode locking in low repetition rate regime where T_r is high. Based on the above discussion, a SESAM with 6% modulation depth (BATOP GmbH) was used in the experiment to initiate the mode locking.

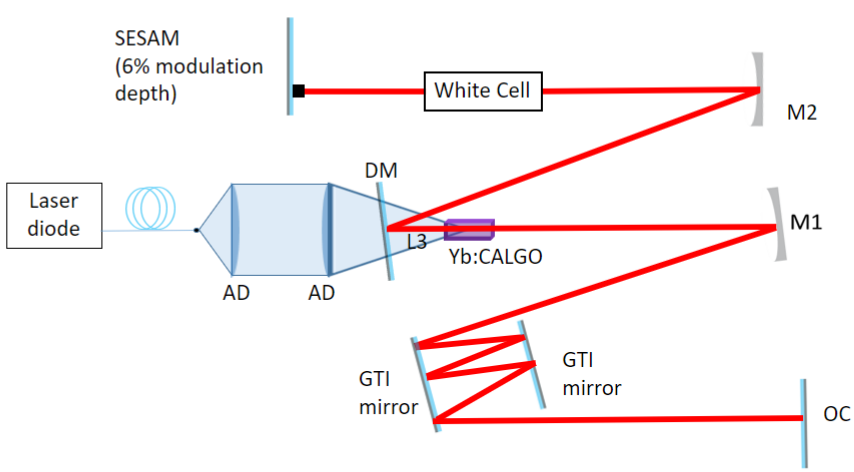

Figure 6.2: Schematic of the low repetition rate cavity with a White cell used for the mode locked operation of Yb:CALGO laser using a SESAM. AD: achromatic doublet, DM: dichroic mirror, GTI: Gires-Tournois interferometer, M1, M2: concave mirrors, OC: output coupler.

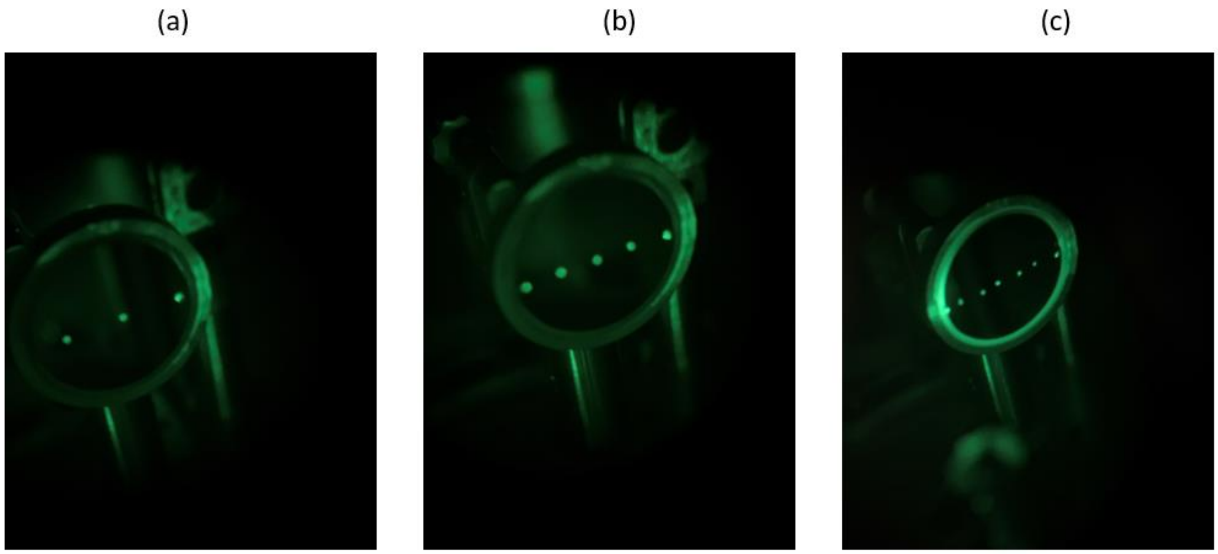

Figure 6.3: Adjusting the turning mirrors changes the number of bounces on the field mirror (a) 3 bounces on the field mirror correspond to 13.85 MHz repetition rate, (b) 5 bounces on the field mirror correspond to 10.15 MHz repetition rate, (a) 7 bounces on the field mirror correspond to 8.2 MHz repetition rate.

6.4 Results and discussion

Initially, the laser performance was monitored in the continuous-wave (CW) regime while a highly reflecting mirror (HR) was used an end mirror. On the other end, different output couplers (OC) were used. By using a 10% output coupler, 7.5 W of output power was recorded at 25 W of incident pump power. The corresponding absorbed pump power was 14 W. After optimizing the laser in the CW regime, the HR mirror was replaced by a SESAM. Although with SESAM, it was expected that mode locking would be self-starting, but in that case, to start the mode locking, a mechanical perturbation was needed on the curved mirror M1 or the output coupler which were put on the translation stages. After mechanical perturbation it was noticed that the spectrum became wider while the output power slightly reduced. For simplicity, initial work was with 3 bounces in the White cell (figure 6.3 (c)). The initial length of the cavity was approximately 1.58 m but with three bounces the total cavity length was increased by 6 m (based on the equation 6.3) which corresponded to 13.85 MHz. In section 6.4.1, the results for 13.85 MHz cavity will be discussed.

6.4.1 13.85 MHz cavity

The mode locking performance of the laser was explored by using 2.5%, 5%, 10%, and 15% output couplers. The GTI mirrors were arranged in such a way that the introduced round-trip dispersion was -2000 fs^2. The pulse train was monitored using a fast photodiode (Thorlabs DET08CFC) and oscilloscope (Tektronix 2465A, 350 MHz) to see if there is any modulation in the pulse train. As it can be seen from the figure 6.4, that the pulse train is free from any distortion which indicates that the mode locking was stable.

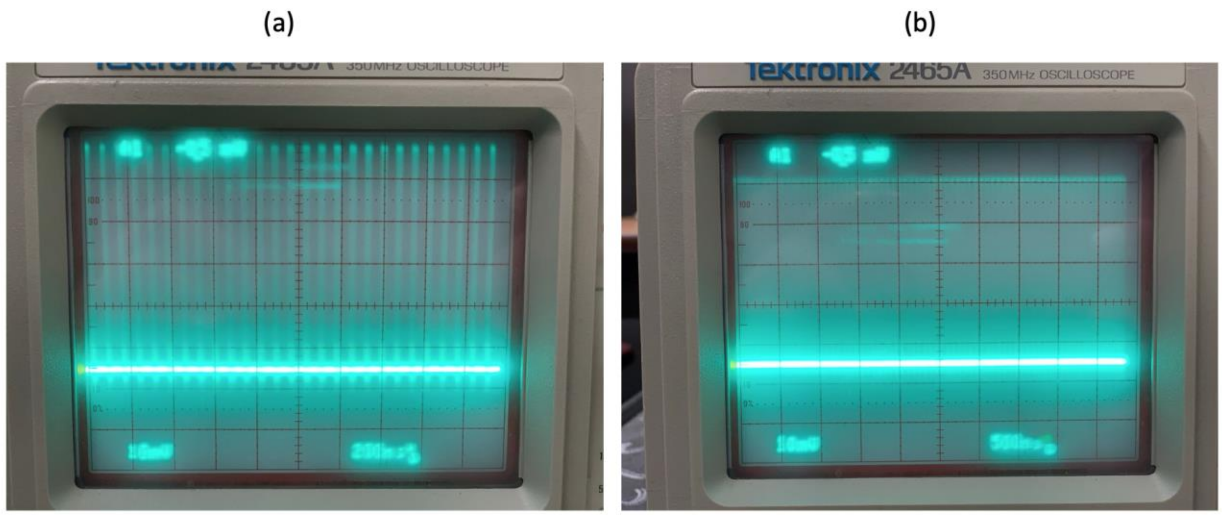

Figure 6.4: Monitoring the mode-locked pulse train with combination of a fast photodiode and oscilloscope at (a) 200 μs/div and (b) 500 μs/div time scales.

Besides monitoring the pulse train, it is also important to see the radio frequency (RF) spectrum of the pulse which was used for the previous experiment (section 5.6). The goal is to compare the signal strength with respect to the noise. It detects if there is any unwanted signal present in the cavity. Basically, the goal to use this spectrum analyzer was to detect if multi-pulsing is present in the cavity. The RF spectrum of the pulse train was also monitored using the DSA 800 spectrum analyzer from Rigol technologies to check on Q-switching or multi-pulsing events. The signal was recorded with a 1 MHz span and a 1 kHz resolution bandwidth. In addition to that, the signal was also monitored up to 100 MHz with 3 kHz resolution bandwidth. This is shown in figure 6.5. The high signal-to-noise ratio indicates that there was no unwanted oscillation present in the cavity.

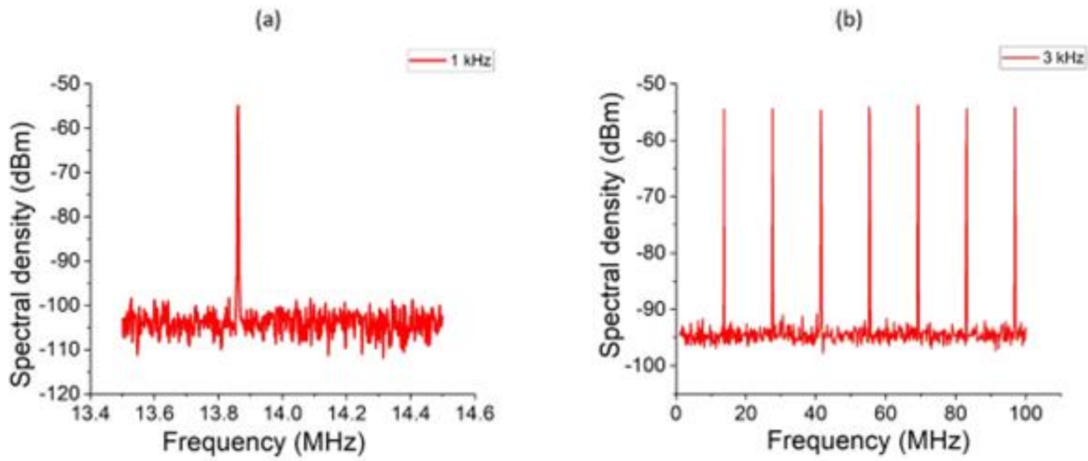

Figure 6.5: Radio frequency spectrum of the pulse train with (a) 1 MHz frequency span and 1 kHz resolution bandwidth (b) 100 MHz frequency span and 3 kHz resolution bandwidth.

A commercial long-range (200 ps) autocorrelator (Femtochrome, FR-103 XL) was used to record the trace of the pulses. To ensure the laser is not working in the multipulse regime, the entire scanning range (200 ps) of the autocorrelator was used. The output spectrum was measured by a high-resolution spectrometer (Anritsu OSA MS9710B) with 0.07 nm resolution. Assuming the $sech^2$ temporal shape, the shortest pulse in this experiment was 68 fs which was obtained with a 2.5 % output coupler. The corresponding spectrum was 19.81 nm wide (FWHM) which indicated a time-bandwidth product of 0.38. The average output power was 110 mW at 15 W of incident pump power. The pulse energy in this case was approximately 7.94 nJ and the peak power was ~116 kW. The measured spectrum and the autocorrelation trace of the pulses are shown below:

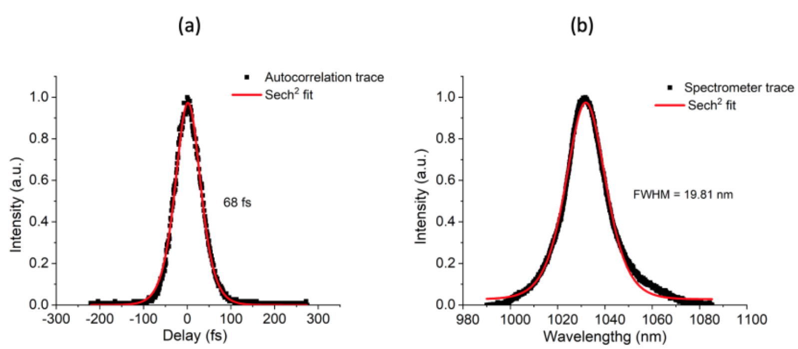

Figure 6.6: (a) The intensity autocorrelation trace of the 68 fs pulses for 2.5% output coupler from 13.85 MHz oscillator and (b) the corresponding optical spectrum.

To get the highest average output power in the sub-100 fs regime, a 15% output coupler was used. With -2000 fs^2 dispersion, we got 73 fs long pulses with 19.57 nm spectrum at FWHM. The corresponding pulse energy was 54.15 nJ and the corresponding peak power was 744 kW. The pulse trace from the autocorrelator and the corresponding spectrum are shown below.

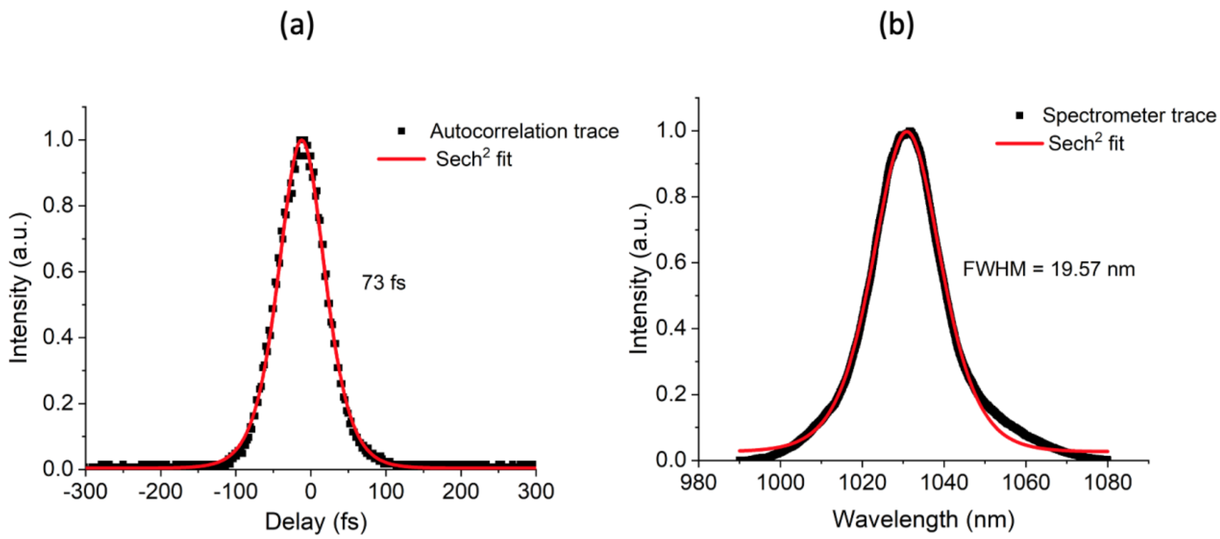

Figure 6.7: The (a) autocorrelation trace of the 73 fs pulses for 15% output coupler from 13.85 MHz oscillator and (b) the corresponding optical spectrum.

During the experiment, it was also noticed that if the dispersion value was changed to -4400 fs^2 it was possible to get a bit higher output power at the expense of the longer pulse duration. However, it is worth mentioning that one can still get pulses in the sub-100 fs regime. The summary of the experiments with -2000 fs^2 and -4400 fs^2 of dispersion for different output couplers is listed in table 6.1. The overall performance of the laser was excellent, and the mode-locked operation was stable. Some KLM effect might present in the cavity, however, by removing the SESAM, no pure KLM was observed. As the initial part of the experiments went well, therefore the next step was to increase the path length to reduce the repetition rate below 13.85 MHz. The details will be discussed in the next sections.

Table 6.1: Summary of 13.85 MHz experiments using the White cell (in the table, P_{inc} = input power, P_{out} = output power, E_p = pulse energy, τ = pulse duration, $\Delta\lambda$ = optical spectrum width at FWHM, TBP = time-bandwidth product)

Rep. rate (MHz)	Dispersion (fs^2)	Output coupler (%)	P_{inc}(W)	P_{out}(W)	E_p (nJ)	P_{peak} (kW)	τ (fs)	$\Delta\lambda$ (nm)	TBP
13.85	-2000	2.5	15	0.110	7.94	116	68	19.81	0.38
		5	16.5	0.29	21	299	70	20.02	0.40
		10	18	0.43	31	423	72	17	0.35
		15	21	0.75	54.15	744	73	19.57	0.40
	-4400	2.5	18	0.2	14.44	147	98	12.5	0.35
		5	18	0.5	36.1	363	100	11.5	0.32
		10	21	1.25	90.25	876	103	11.08	0.32
		15	24	1.45	104.7	1067	98	11.59	0.32

6.4.2 10.15 MHz cavity

As the laser performed efficiently with three bounces (13.85 MHz) in the White cell, the next step was to go for a lower repetition rate operation by increasing the number of bounces on the field mirror. As described earlier, simultaneous adjustment of the two turning mirrors changes the number of bounces on the field mirror by an odd integer, i.e., it increases the path length for the beam. After adjusting the two turning mirrors, five bounces on the field mirror were spotted (figure 6.3 (b)). The total path length of the beam inside the White cell therefore was 10 m. The corresponding repetition rate became 10.15 MHz. To compensate for the positive dispersion, two GTI mirrors each having a GDD of -250 fs^2 and 550 fs^2 per bounce were placed in the cavity which provided a total of -3200 fs^2 of roundtrip GDD. All other cavity optics were selected in such a way that we got the lowest possible dispersion at the lasing wavelength. The shortest pulse observed was 83 fs and it was obtained with a 2.5% output coupler. The pulse intensity autocorrelation and the corresponding spectrum are shown below:

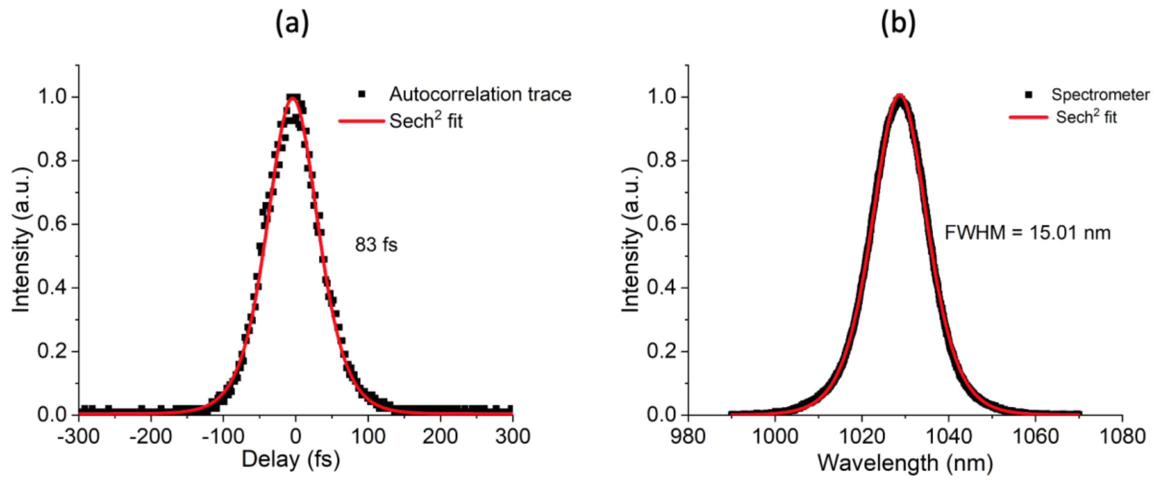

Figure 6.8: (a) The autocorrelator trace of the 83 fs pulses for 2.5% output coupler from 10.15 MHz oscillator (b) the corresponding 15.01 nm optical spectrum.

To determine if there is any modulation present in the mode locking, the pulse train was recorded using the same oscilloscope used with the 13.85 MHz oscillator. From figure 6.9 (a), it can be seen the flat top of the pulse train which shows that the mode locking was free from any modulation. In addition to that, the RF spectrum of the pulse was also recorded with a 1 nm span and 1 kHz resolution bandwidth and the high signal-to-noise ratio indicates that the signal was free from Q-switching (figure 6.9 (b)). The pulses in the autocorrelator were monitored in the 200 ps range to ensure that it was not operating in the multi-pulsing regime. To get high pulse energy, we used a 15% output coupler. Using it with -3200 fs^2 of roundtrip GDD, 94 fs pulses with 13.95 nm wide spectrum were recorded. The corresponding time-bandwidth product was 0.37 which indicates that the pulses were almost transformed limited. The corresponding pulse energy was 69 nJ and the peak power was 734 kW. The pulses were also recorded with -4400 fs^2 roundtrip GDD and pulses were still in the sub-100 fs regime with a bit higher output power. The results are summarized in table 6.2.

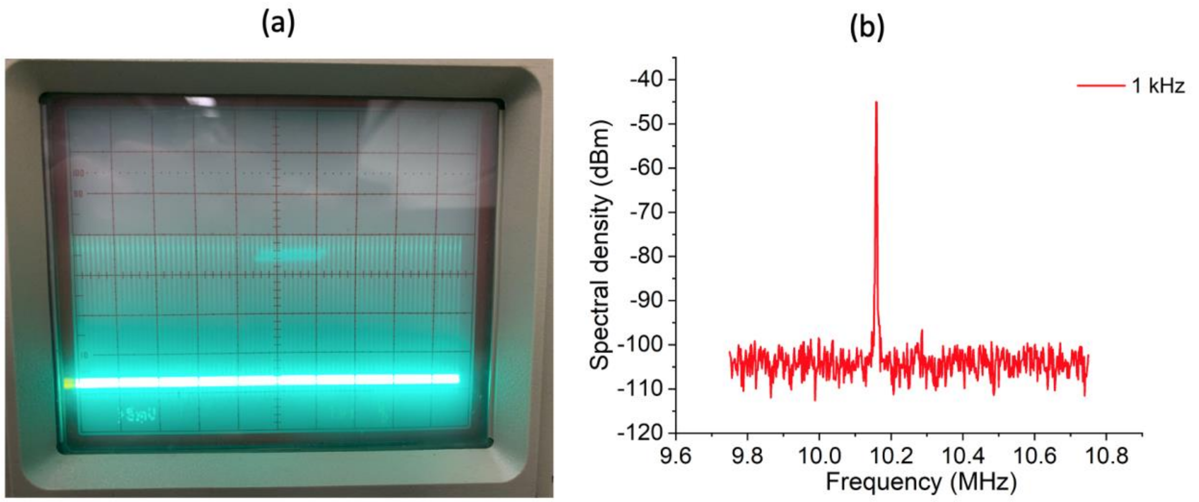

Figure 6.9: (a) The pulse train with a flat top indicates the mode -locking without any modulation, (b) the high signal to noise ratio of the RF spectrum indicates the signal did not have any Q-switched mode locking effect.

Table 6.2: Summary of the 10.15 MHz experiment (in the table, P_{inc} = input power, P_{out}= output power, E_p = pulse energy, τ= pulse duration, $\Delta\lambda$= optical spectrum width at FWHM, TBP = time-bandwidth product)

Rep. rate (MHz)	**Dispersion (fs^2)**	**Output coupler (%)**	**P_{inc}(w)**	**P_{out}(w)**	**E_p (nJ)**	**P_{peak} (KW)**	**τ (fs)**	**$\Delta\lambda$ (nm)**	**TBP**
10.15	-3200	2.5	17.7	0.1	9.85	118.67	83	15.01	0.35
		15	25	0.7	69	734	94	13.95	0.37
	-4400	2.5	22.5	0.1	9.85	101.54	97	12.66	0.35
		15	25	0.95	93.59	936	100	11.73	0.33

6.4.3 8.2 MHz cavity

Further reduction of the cavity repetition rate was done by adjusting the two turning mirrors again to obtain 7 bounces on the field mirror (figure 6.3 (c)). The White cell length was increased by 4 m which resulted in the repetition rate of 8.2 MHz. To the best of our knowledge, this is the lowest repetition rate for any mode-locked Yb:CALGO laser. Initially, the roundtrip intracavity group velocity dispersion of -3200 fs^2 was used. To ensure the mode locking did not contain any modulation and the signal was free from excessive noise, the pulse train of the mode-locked laser and the RF spectrum were recorded in similar ways to what was done before (figure 6.10).

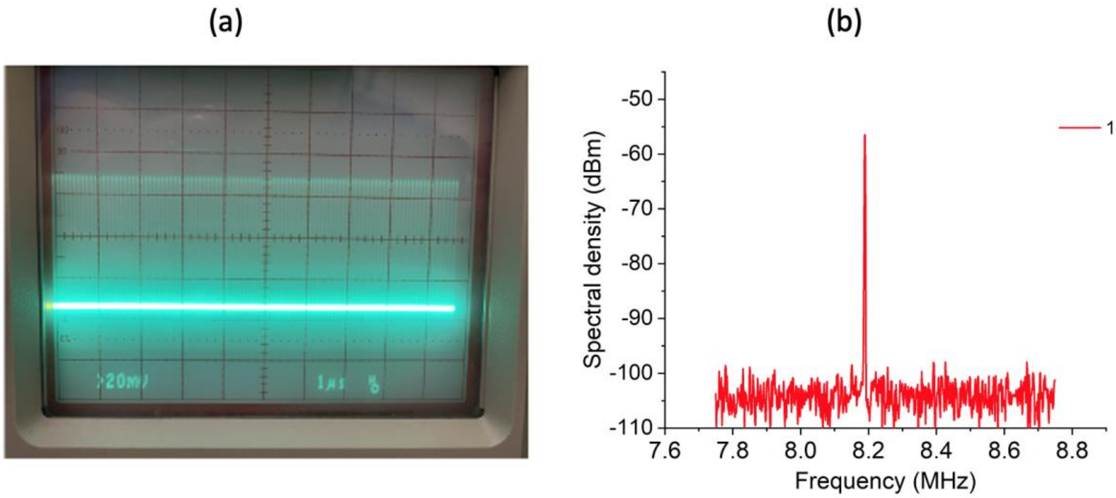

Figure 6.10: (a) The optical pulse train obtained recorded with a fast diode and oscilloscope to determine if it contains any modulation, (b) the RF spectrum of the mode-locked signal.

The shortest pulse that was obtained from this experiment was 114 fs (figure 6.11) with a 2.5% output coupler with 100 mW of output power. The corresponding pulse energy was 12.2 nJ and the peak power was 107 kW. The calculated time-bandwidth product was 0.33 which indicates that we had almost transform-limited pulses. To obtain the highest output power, we used a10% output coupler for the same roundtrip GDD. In this case, 126 fs pulses were obtained with 430 mW of output power. The corresponding pulse energy and peak power were 52.44 nJ and 416 kW.

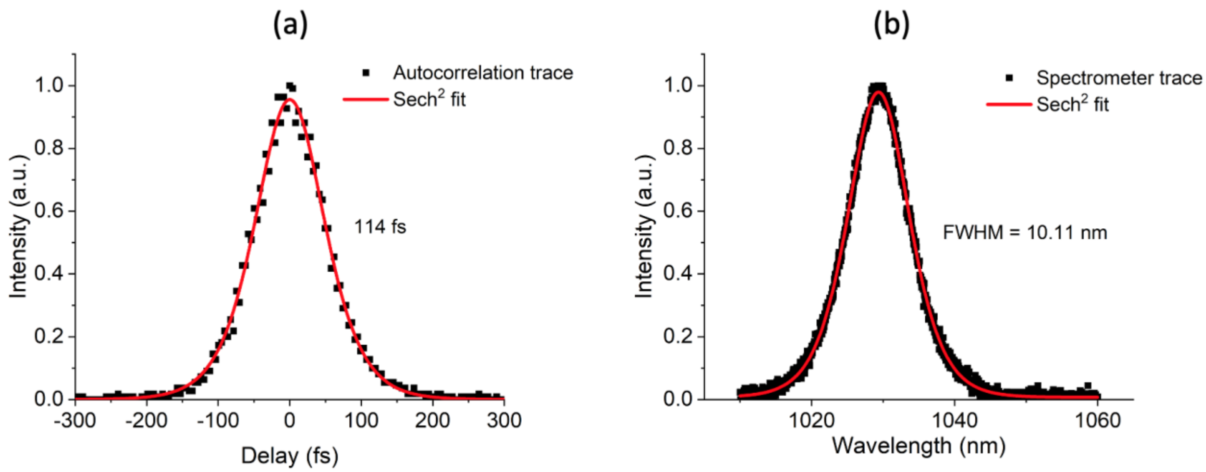

Figure 6.11: (a) Autocorrelator trace for 114 fs pulse at 8.2 MHz repetition rate; (b) corresponding spectrum.

Like in the previous experiments, different GDD values were used to evaluate the performance of our mode-locked laser and the summary is listed in table 3.

Table 6.3: Summary of 8.2 MHz experiment using the White cell (In the table, P_{inc} = input power, P_{out}= output power, E_p = pulse energy, τ= pulse duration, $\Delta\lambda$= optical spectrum (FWHM), TBP = Time-bandwidth product)

Rep. rate (MHz)	**Dispersion (fs^2)**	**Output coupler (%)**	**P_{inc} (W)**	**P_{out} (W)**	**Ep (nJ)**	**P_{peak} (kW)**	**τ (fs)**	**$\Delta\lambda$ (nm)**	**TBP**
8.2	-3200	2.5	16	0.1	12.2	107	114	10.11	0.33
		10	21	0.43	52.44	416.19	126	9.16	0.33
	-4400	2.5	16	0.15	18.29	136.49	134	8.5	0.32
		10	25	0.65	79.26	528.4	150	9.69	0.41

6.5 Conclusion

In conclusion, a sub-100 fs mode locked Yb:CALGO laser was demonstrated by extending the laser cavity with a White cell configuration. To the best of our knowledge, this is the first femtosecond laser that was developed based on the White cell configuration. In this experiment, the repetition rate was changed simply by adjusting the turning mirrors of the White cell. The shortest pulse was 68 fs with 110 mW of output power at 13.85 MHz. The lowest repetition rate was 8.2 MHz. The mode locking was based on SESAM with 6% modulation depth. Although the mode locking was supposed to be self-starting, but one of the end cavity mirrors or the curved mirror M1 needed tapping to initiate it. The use of White cell in the femtosecond laser operation will make it easier to lower the repetition rate.

REFERENCES

[6.1] A. M. Larson, "Multiphoton microscopy," Nat. Photonics 5, (2011), doi:10.1038/nphoton.an.2010.2.

[6.2] A. F. Pegoraro, A. Ridsdale, D. J. Moffatt, Y. Jia, J. P. Pezacki, and A. Stolow, "Optimally chirped multimodal CARS microscopy based on a single Ti:sapphire oscillator," Opt. Express 17, 2984-2996 (2009).

[6.3] J. G. Fujimoto, A. D. Aguirre, Y. Chen, P. R. Herz, P.-L. Hsiung, T. H. Ko, N. Nishizawa, and F. X. Kärtner, "Ultrahigh-Resolution Optical Coherence Tomography Using Femtosecond Lasers," in Ultrashort Laser Pulses in Biology and Medicine, M. Braun, P. Gilch, and W. Zinth, eds. (Springer Berlin Heidelberg, 2008), pp. 3–27.

[6.4] B. E. Bouma, G. J. Tearney, I. P. Bilinsky, B. Golubovic, and J. G. Fujimoto, "Self-phasemodulated Kerr-lens mode-locked Cr:forsterite laser source for optical coherence tomography," Opt. Lett. 21, 1839 (1996).

[6.5] W. Drexler, U. Morgner, F. X. Kärtner, C. Pitris, S. a Boppart, X. D. Li, E. P. Ippen, and J. G. Fujimoto, "In vivo ultrahigh-resolution optical coherence tomography," Opt. Lett. 24, 1221 (1999).

[6.6] Y. J. Chai, C. G. Leburn, A. a. Lagatsky, C. T. a. Brown, R. V. Penty, I. H. White, and W. Sibbett, "1.36-Tb/s spectral slicing source based on a Cr4+-YAG femtosecond laser," J. Light. Technol. 23, 1319–1324 (2005).

[6.7] E. A De Souza, M. C. Nuss, W. H. Knox, and D. A. B. Miller, "Wavelength-division multiplexing with femtosecond pulses," Opt. Lett. 20, 1166 (1995).

[6.8] A. Sennaroglu, and J. G. Fujimoto, "Design criteria for Herriott-type multi-pass cavities for ultrashort pulse lasers," Opt. Express 11, 1106-1113 (2003).

[6.9] A. Major, V. Barzda, P. A. E. Piunno, S. Musikhin, and U. J. Krull, "An extended cavity diode-pumped femtosecond Yb:KGW laser for applications in optical DNA sensor technology based on fluorescence lifetime measurements," *Opt. Exp.*, vol. 14, pp. 5285-5294, 2006.

[6.10] A. Major, R. Cisek, D. Sandkuijl, and V. Barzda, "Femtosecond Yb:KGd(WO4)2 laser with >100 nJ of pulse energy," Laser Phys. Lett. 6, 272–274 (2009).

[6.11] H. Zhao, and A. Major, "Megawatt peak power level sub-100 fs Yb:KGW oscillators", Opt. Express, Vol 22(25), 30425-30431 (2014).

[6.12] J. U. White, “Long optical paths of large aperture”, J.O.S.A., Vol. 32 (1942).

[6.13] A. Sennaroglu and J.G. Fujimoto, “Design criteria for Herriott-type multi-pass cavities for ultrashort pulse laser, *Opt. Express*, vol. 11(9), pp 1106-1113(2003).

[6.14] S. Naumov, A. Fernandez, R. Graf, P. Dombi, F. Krausz and A. Apolonski, “Approaching the microjoule frontier with femtosecond oscillators”, new journal of Phy. 7 (2005).

[6.15] D.N. Papadopoulos, S. Forget, M. Delaigue, D. Druon, F. Balembois and P. Georges, “Passively mode-locked diode-pumped Nd:YVO_4 oscillator operating at ultra-low repetition rate”, Opt. Lett. 28(19), 1838-1840 (2003).

[6.16] N. H. Schiller, X. M. Zhao, X.C. Liang, L.M. Wang, and R.R. Alfano, “Compact picosecond Nd:glass mode-locked laser with variable cavity length from 5 to 21 m”, App. Optics 28(5), 946-948 (1989).

[6.17] J.B. Deaton, Jr. A.D.W. Mckie, J.B. Spicer, and J.W. Wagner, “Generation of narrow-band ultrasound with a long cavity mode-locked Nd:YAG laser”, App. Phys. Lett. 56(24), 2390-2392 (1990).

[6.18] J.B. Deaton, Jr., and James W. Wagner, “Variable-cavity-length mode-locked Nd:YAG laser for noncontact generation and spatial control of narrow-band ultrasound”, App. Optics 33(6), 1051-1058 (1994).

[6.19] J. Chen, R. Knappe, and W. Viol, “Passivley mode-locked Nd:YVO_4 multipass resonator with low repetition rate”, Laser phys. Lett 5(6), 425-428 (2008).

[6.20] G. Cleon, D. Stepowski, and A. Cessou, “Long-cavity Nd:YAG laser used in single-shot spontaneous Raman scattering measurements”, Opt. Lett. 32(22), 3290-3292 (2007).

[6.21] S. Manjooran and A. Major, “Low repetition rate operation of a femtosecond Yb:CALGO laser”, Proc. of SPIE Vol. 10511(2018).

[6.22] F. Krausz, M. E. Fermann, T. Brabec, P. F. Curley, M. Hofer, M. H. Ober, C. Spielmann, E. Winter and A. J. Schmidt, “Femtosecond solid-state lasers”, IEEE J. Quant. Electron. 28, 2097 (1992).

Chapter 7
Conclusion and future work

7.1 Conclusion

The goal of this thesis was to develop a sub-100 fs ultrafast Yb:CALGO laser with high peak power. The condition to operate efficiently in the mode-locked regime is that the laser should work efficiently in the continuous-wave regime as well. This is why before the mode locking operation, some experiments were done in the CW regime. The first one was estimating the intracavity losses of the laser cavity. Intracavity losses reduce the laser efficiency and in an extreme case may cease the lasing. The loss was estimated based on three different techniques. The spectroscopic gain analysis is a dynamic and simple technique. In addition to that, the loss was also estimated based on the Findlay-Clay method and numerical method which are conventional techniques and have some limitations. It was found that the loss was low which is a prerequisite for efficient laser operation. The second one was generating the dual-wavelength output based on optimized birefringent filer (BRF). It has been shown that the regular BRF can generate dual-wavelength output with fixed wavelength separation for a given thickness. In contrast, the optimized BRF can tune the dual-wavelength separation without the need to change the thickness. Based on the proposed design, two BRFs with 12 mm and 24 mm of thickness were used and showed fine-tuning of the dual-wavelength output. The third one was getting conical refraction (CR) output from the CW Yb:CALGO laser. The CR beam from this experiment was of high quality with high output power. In addition to that, the tuning and DW operation of the CR laser were also presented.

As the laser was operating very well in the CW regime, the next goal was to generate ultrashort pulses based on mode locking. As the Yb:CALGO crystal has high emission bandwidth (~50 nm) and high thermal conductivity (6.9 W/m/K), therefore it should be suitable to generate sub-100 fs pulses with high output power. To get the high peak power by boosting the pulse energy, the laser cavity was extended. The first method that we used to extend the cavity was inserting a 1:1 imaging telescope. 81 fs pulses were recorded at a 26.9 MHz repetition rate. The pulse energy and the peak power were 48 nJ and 596 kW, respectively.

However, further extension of the cavity was complicated as it needed insertion of another 1:1 imaging telescope which would make the alignment complicated. To eliminate these issues the use of a White cell configuration was proposed. The White cell consists of three concave mirrors of the same radius of curvature. They allow control of the number of bounces inside the White cell which gave us the flexibility to reduce the repetition rate without the need of multiple additional optical components. Therefore, extending the laser cavity became simple. Based on the number of bounces in the White cell, the laser cavity was operating 13.85 MHz, 10.15 MHz and 8.20 MHz repetition rates. Pulses as short as 68 fs were recorded, and the highest peak power was 744 kW from this experiment. In section 5.6, the results from this experiment were compared with the previous results and showed that using the White cell one can lower the repetition rate in a compact and cost-effective way. Also, there are few experiments which obtained sub-100 fs pulses with such a low repetition rate.

Based on the above discussion, the goal of achieving sub-100 fs pulses with high peak power was successful. Hopefully, these experiments will extend the applications in the areas such as nonlinear microscopy, biomedical imaging, and high-speed optical communications.

7.1 Future work

As an extension of this work, there is plenty of room available. In the experiment, the dual-wavelength output was obtained using the off-surface axis BRF in the CW regime. It would be nice to try the same BRFs in the mode locked operation.

The White cell configuration has a lot of opportunities to work on as this was the first-ever report on the femtosecond mode-locked laser based on it. The field mirror in our White cell was 50 mm in diameter, therefore there is a limit on the maximum number of bounces on it. A field mirror with a bigger diameter such as 150 mm can accommodate more bounces on it, therefore it will enable one to reduce the repetition rate further below than what was obtained in this experiment. In previous experiment, 17 spots were obtained using a 150 mm field mirror. If one uses the similar field mirror, then with 17 spots on the field mirror, it is possible to bring down the repetition rate to around 4 MHz. In applications such as fluorescence lifetime measurement, a low repetition rate (suggested around 1-2 MHz) laser source is useful. In experiments using photon counting detection chain, the high repetition rate causes problem in signal processing devices to record the data.

The mode locking method of our laser was based on the SESAM. It would be interesting if one can extend the laser cavity by using the White cell configuration where the mode locking method is based on the Kerr-lensing effect. It is strongly recommended to use a fiber laser source for pumping as it will give good beam quality which in turn will ensure a good overlap between the pump mode and the laser mode and facilitate KLM operation.

Another interesting work could be the Kerr-lens mode locking of the laser by using an additional intracavity element. The design procedure of the KLM laser cavity is more complex than of SESAM based lasers. The laser operates close to the stability region and tight focusing is required. Also, the laser crystal works as both gain medium and Kerr medium. Such a tight focusing would reduce the efficiency of the laser and it is difficult to achieve where the pump source is a multimode one with a bad beam quality (such as the used laser diode). The addition of another nonlinear medium in the laser cavity eliminates the need to use tight focusing on the gain medium and can increase the Kerr lensing effect in the cavity.

Appendix A: Jones matrix calculation

The propagation of two transverse polarizations of light in a homogenous isotropic medium can be expressed in terms of Jones vectors. The Jones matrices are operator for Jones vector which can be expressed as,

$$\begin{pmatrix} E_{0x}e^{i\phi_x} \\ E_{0y}e^{i\phi_y} \end{pmatrix}$$

Different optical elements or transmission medium has different Jones matrices. In this section, the discussion will be focused Jones matrix (M). The Jones matrix for the BRF discussed in chapter 3 with figure 3.1 can be written as:

$$\mathrm{M} = \begin{pmatrix} 1 & 0 \\ 0 & q \end{pmatrix} \begin{pmatrix} sin\alpha_{eq} & cos\alpha_{eq} \\ -cos\alpha_{eq} & sin\alpha_{eq} \end{pmatrix} \begin{pmatrix} 1 & 0 \\ 0 & e^{i\phi} \end{pmatrix} \begin{pmatrix} sin\alpha_{eq} & -cos\alpha_{eq} \\ cos\alpha_{eq} & sin\alpha_{eq} \end{pmatrix} \begin{pmatrix} 1 & 0 \\ 0 & q \end{pmatrix} \qquad \text{(B1)}$$

where Loss due Fresnel reflection (for s-polarization), $q = \frac{2n}{(n^2+1)}$

$sin\alpha_{eq} = \sqrt{(1 - cos^2\alpha_{eq})}$

$cos\alpha_{eq} = (\cos\phi \cos\theta \cos\alpha - \sin\phi \sin\theta\ )/sin\,\gamma$

Phase difference due to birefringence,

$$\varphi = [(sin^2\ .cos^2) + (cos\alpha . cos\phi(n). cos\theta - sin\theta . \sin\phi(n))^2] \qquad \text{(B2)}$$

The round-trip Jones matrix for the linear laser cavity can be written as:

$$M_{rountrip} = Q'Q'MM \qquad \text{(B3)}$$

Here, Q' is defining the polarization dependent loss inside the laser cavity. As the oscillating wave repeat itself after one round trip, so the eigen value of $M_{rountrip}$ is the electric field amplitude transmission and $|m|^2$is the roundtrip power transmission.

REFERENCES

[A.1] K. Naganuma, G. Lenz, and E. P. Ippen, "Variable bandwidth birefringent filter for stable femtosecond lasers", IEEE J. Quantum Electron. 28(10), 2142-2150 (1992).

[A.2] T. Waritanant, "Highly efficient diode-pumped lasers based on in-band pumping of Nd: YVO_4 crystal", Ph.D. thesis, University of Manitoba, 2017.

Appendix B: ρ_0 calculation

A beam with Gaussian intensity distribution travelling along the one of the optical axes of a biaxial crystal refracts conically and transforms into a bright pair of concentric rings separated by a dark Poggendorff ring. To get a nice CR beam with dark Poggendorff ring the condition is ρ_0>>1, where the parameter ρ_0 is the ratio of the radius of the CR beam to the radius of the input beam.

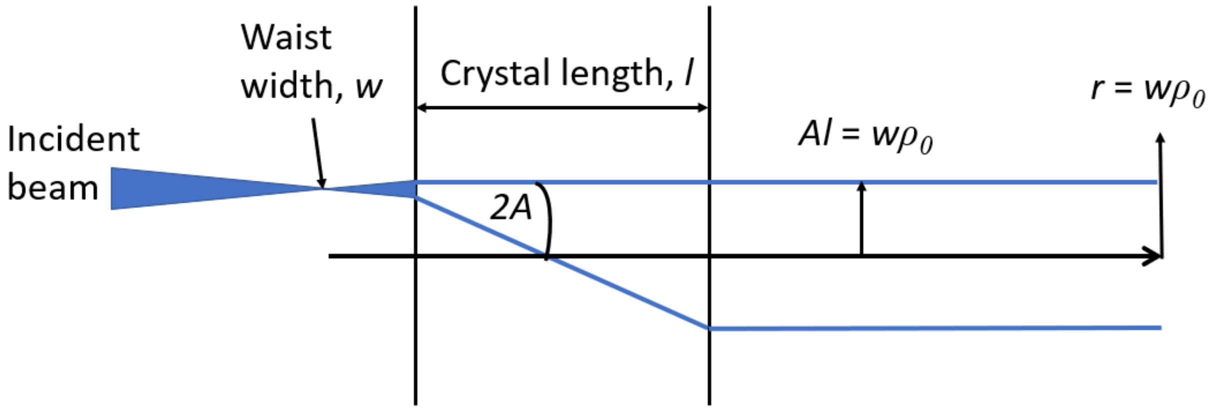

Figure B1: Schematic of the incident beam, forming cone inside the crystal and emerging as a hollow cylinder [B.1].

A collimated beam of light that emerges as a narrow hollow cone within a biaxial crystal with a semiangle as shown in figure C1:

$$A = \frac{1}{n_2}\sqrt{(n_2 - n_1)(n_3 - n_2)} \tag{C1}$$

where, n_1, n_2 and n_3 are the distinct refractive indices of the crystal, and the relation among them is $n_1 < n_2 < n_3$. Also $(n_2 - n_1)$ and $(n_3 - n_2)$ should be small compared to n_2 so that refraction and diffraction effects are paraxial.

The profile of the beam after passing through the crystal with length, l depends on ρ_0 which, can be defined as:

$$\rho 0 = \frac{Al}{w} \tag{C2}$$

$$\rho 0 = \frac{r}{w} \tag{C3}$$

Here, *w* is the beam waist radius and *r* is the ring radius. The refractive indices were calculated based on the Sellmeier's equation as a function of the wavelength which can be written as:

$$n(\lambda)^2 = A + \sum_i \frac{B_i}{\lambda^{2-C_i}} + D_i \lambda^{2i} \tag{C4}$$

where, *A, B, C* and *D* are Sellmeier's coefficients of the medium. The Sellmeier's coefficient for KGW is given below in table 1. In the table *n(λ)* is the value of the refractive index for the corresponding axis.

Table-1: Sellmeier's coefficients and the calculated refracted indices.

		A	B	C/nm	D/nm^2	n (λ)
KGW	n_g	1.3867	0.6573	170.02	0.2913×10^{-9}	2.061
	n_m	1.5437	0.4541	188.91	2.1567×10^{-9}	2.013
	n_p	1.5344	0.4360	186.18	2.0999×10^{-9}	1.984

Based on equation 1, the semiangle was 18 mrad. For an 18 mm long CRE and the pump beam radius of approximately 77µm, the calculated ρ_0 was approximately 4 for our CR experiment.

REFERENCES

[B.1] M. V. Berry, “Conical diffraction asymptotics: fine structure of Poggendorff rings and axial spike,” J. Opt. A 6, 289 (2004).

[B.2] M. C. Pujol, M. Rico, C. Zaldo, R. Solé, V. Nikolov, X. Solans, M. Aguiló, and F. Díaz, "Crystalline structure and optical spectroscopy of Er3+-doped KGd(WO4)2 single crystals," Appl. Phys. B 68, 187–197 (1999).

[B.3] R. Akbari, “High peak power ultra-short pulses diode-pumped Yb:KGW lasers”, Ph.D. thesis, University of Manitoba, 2017.

Appendix C: Gaussian beam and ray tracing

A laser beam propagating in the z-direction can be expressed by a Gaussian function as:

$$E(r,z) = E_0 \frac{w_0}{w(z)} \exp(-\frac{r^2}{w(z)^2}) \exp(-i [kz - \tan^{-1} \frac{Z}{z_R} + \frac{Kr^2}{2\,R\,(z)}] \quad \text{(A1)}$$

Where $|E_0|$ is the peak amplitude, wave number, $k = 2\,\pi/\lambda$, z_R is the Rayleigh length and $R(z)$ is the radius of the curvature of the wavefront. The beam radius at any point along the propagation direction can be calculated as:

$$w(z) = w \sqrt{1 + (\frac{zM^2}{z_R})^2} \quad \text{(A2)}$$

where, M^2 is known as the beam quality factor which measures the spatial quality of a laser beam. For a given wavelength λ, this dimensionless factor can be defined as:

$$M^2 = \theta \frac{\pi w_0}{\lambda} \quad \text{(A3)}$$

where w_o is the beam waist and θ is half-angle beam divergence. An ideal Gaussian beam has M^2= 1.

The Rayleigh range z_R (distance from beam waist to the place where cross-section area is doubled) can be expressed as:

$$z_R = \frac{\pi w_0^2}{\lambda M^2} \quad \text{(A4)}$$

The radius of the curvature of a Gaussian beam can be defined as:

$$R(z) = z\,[1+ (\frac{Z}{z_R})^2] \quad \text{(A5)}$$

The ABCD matrix is a matrix that provides information of an optical element to transform the light information that passes through it. The ABCD matrix can be expressed as:

$$M_{ABCD} = \begin{pmatrix} A & B \\ C & D \end{pmatrix} \quad \text{(A6)}$$

A wavefront and width of a Gaussian beam at any point can be expressed by complex q-parameter as:

$$q = -\,i\,\frac{\lambda}{\pi\, w^2} + \frac{1}{R} \tag{A7}$$

The q-parameter gets modified while propagating in a free space/ optical element and the modified q-parameter can be calculated as follows:

$$q' = \frac{Aq+B}{Cq+D} \tag{A8}$$

The most common ABCD matrices are listed below:

Element	Matrix	
Free space	$\begin{bmatrix} 1 & d \\ 0 & 1 \end{bmatrix}$	d = Propagation distance
Thin lens	$\begin{bmatrix} 1 & 0 \\ -1/f & 1 \end{bmatrix}$	f = Focal length of the lens
Flat mirror	$\begin{bmatrix} 1 & 0 \\ 0 & 1 \end{bmatrix}$	
Crystal	$\begin{bmatrix} 1 & d/n \\ 0 & 1 \end{bmatrix}$	d = Propagation distance n = Refractive index
Curved mirror	$\begin{bmatrix} 1 & 0 \\ -1/2r & 1 \end{bmatrix}$	r = Radius of the curvature of the mirror

REFERENCES

[C.1] B. E. A Saleh, M. C. Teich, “Fundamentals of photonics,” Wiley, 2007.

[C.2] R. Akbari, “High peak power ultra-short pulses diode-pumped Yb:KGW lasers”, Ph.D. thesis, University of Manitoba, 2017.

[C.3] H.Zhao, “Powerful diode-pumped ultrafast solid-state laser oscillators based on bulk Yb:KGd$(WO_4)_2$”, Ph.D. thesis, University of Manitoba, 2015.

[C.4] T. Waritanant, “Highly efficient diode-pumped lasers based on in-band pumping of Nd: YVO_4 crystal”, Ph.D. thesis, University of Manitoba, 2017.

Appendix D: Alignment of the White cell

The White cell is a very useful tool to extend the laser cavity without altering the q-parameter of the laser cavity. The details of operation and working principle can be found in chapter 6 of this thesis. The goal of this section is to explain the White cell alignment procedure.

At the beginning of the process, a stable CW laser oscillation was obtained in a regular length cavity. In this case the regular cavity consists of M1, M2 (concave mirrors), dichroic mirror (DM), output coupler (OC) and a HR mirror. This regular cavity should perform well in terms of the output power and beam quality as well. Then the arrangement was changed for the White cell alignment setup as shown in figure D1. The first step was replacing the HR mirror with a low transmission output coupler (0.4% for this experiment). Using a power meter, it was confirmed that the output power after the 0.4% OC was low. An optical beam blocker (figure D2(a)) was used to control the beam propagation and avoid potential damage. Using an infrared sensor card (figure D2(b)) the beam path was traced and monitored. In figure D1, mirrors M4, M5 and M6 form the While cell. The use of mirrors M3 and M6 is optional but can be useful to make sure that the entering and exiting beams are close to the field mirror [D.1]. The height of the beam after the 0.4% output coupler remained the same and this was checked using an iris diaphragm shown in figure D2(c).

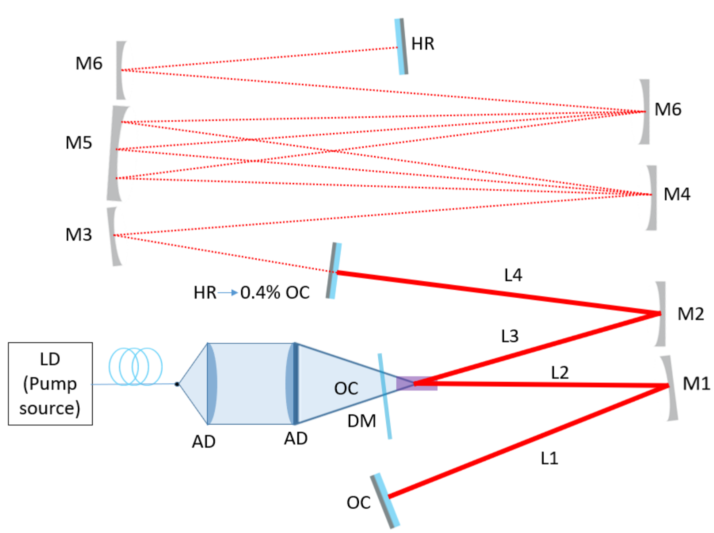

Figure D1: The White cell alignment procedure.

Figure D2: (a) Optical beam blocker, (b) infrared sensor card, and (c) iris diaphragm [D.2].

After that the turning mirrors M4 and M6 were moved simultaneously to obtain the desired number of bounces on the field mirror. An infrared viewer was used to monitor this. In most of the cases, removal of the 0.4% OC after the cell alignment process caused the laser to oscillate with the extended cavity. If not, then gently rocking the HR mirror (or the OC) was helpful to get the laser oscillation.

REFERENCES

[D.1] J.B. Deaton, Jr., and James W. Wagner, “Variable-cavity-length mode-locked Nd:YAG laser for noncontact generation and spatial control of narrow-band ultrasound”, App. Optics 33(6), 1051-1058 (1994).

[D.2] www.newport.com